EXPERIMENTAL AND NUMERICAL ANALYSIS OF SEISMIC WAVES PRODUCED BY WIND FARMS

Dissertation

Zur Erlangung des Doktorgrades

der Naturwissenschaften

vorgelegt beim Fachbereich 11

der Johann Wolfgang Goethe-Universität

in Frankfurt am Main

von

FABIAN LIMBERGER

aus Lahr im Schwarzwald

Frankfurt 2023

(D 30)

Vom Fachbereich Geowissenschaften/Geographie der

Johann Wolfgang Goethe - Universität als Dissertation angenommen.

Dekan:	Prof. Dr. Jürgen Runge
GutachterIn:	Prof. Dr. Georg Rümpker
	Prof. Dr. Christine Thomas

Datum der Disputation:

Content

Abstract

This thesis presents the experimental and numerical analysis of seismic waves that are produced by wind farms. With the aim to develop renewable energies rapidly, the number of wind turbines has been increased in recent years. Ground motions induced by their operation can be observed by seismometers several kilometers away. Hence, the seismic noise level can be significantly increased at the seismic station. Therefore, this study combines long-term experiments and numerical simulations to improve the understanding of the seismic wavefields emitted by complete wind farms and to advance the prediction of signal amplitudes.

Firstly, wind-turbine induced signals that are measured at a small wind farm close to Würzburg (Germany) are correlated with the operational data of the turbines. The frequency-dependent decay of signal amplitudes with distance from the wind farm is modeled using an analytical method including the complex effects of interferences of the wavefields produced by the multiple wind turbines. Specific interference patterns significantly affect the wave propagation and therefore the signal amplitude in the far field of a wind farm. Since measurements inside the wind turbines show that the assumption of in-phase vibrating wind turbines is inappropriate, an approach to calculate representative seismic radiation patterns from multiple wind turbines, which allows the prediction of amplitudes in the far field of a complete wind farm, is proposed.

In a second study, signals with a frequency of 1.15 Hz, produced by the Weilrod wind farm (north of Frankfurt, Germany) are observed at the seismological observatory TNS (Taunus), which is located at a distance of 11 km from the wind farm. The propagation of the wavefield emitted by the wind farm is numerically modeled in 3D, using the spectral element method. It is shown that topographic effects can cause local signal amplitude reductions, but also signal amplification along the travel path of the seismic wave. The comparison of simulations with and without topography reveals that the reduction and amplification are spatially linked to the shape of the topography, which could be an explanation for the relatively high signal amplitude observed at TNS.

Finally, the reduction of the impact of wind turbines on seismic measurements using borehole installations is studied using 2D numerical models. Possible effects of the seismic velocity, attenuation, and layering of the subsurface are demonstrated. Results show that a borehole can be very effective in reducing the observed high-frequency signals emitted by wind turbines. However, a borehole might not be beneficial if signals with frequencies of about 1 Hz (or lower) are of interest, due significant wavelength-dependent effects. The estimations of depth-dependent amplitudes with a layered subsurface are validated with existing data from wind-turbine-induced signals measured at the top and bottom of two boreholes.

The experimental analysis of measurements conducted at wind farms and the advances of modeling such signals improve the understanding of the propagation of wind-farm induced seismic wave fields. Furthermore, the methods developed in this work have a high potential of universal application to the prediction of signal amplitudes at seismometers close to wind farms with arbitrary layout and geographic location.

Zusammenfassung

Das Innere der Erde wird anhand von seismischen Wellen, die den Erdglobus nach einem Erdbeben durchlaufen, erforscht. Seismische Wellen sind elastische Wellen und transportieren Informationen des Untergrunds an die Erdoberfläche und ermöglichen damit Aussagen zum Aufbau, zur Struktur und Beschaffenheit der Erde auf lokaler und globaler Skala. Mit hochempfindlichen Seismometern lassen sich schon sehr kleine Bodenbewegungen und Deformationsprozesse an der Erdoberfläche nachweisen. Neben Erdbeben oder vulkanischen Prozessen werden Seismometer auch zur globalen Überwachung von Nuklearwaffentests oder zur Erfassung lokaler mikroseismischer Ereignisse, beispielsweise bei geothermischen Kraftwerken oder Aktivitäten in Steinbrüchen, eingesetzt.

Aufgrund von wachsenden Bevölkerungszahlen, der Vergrößerung der Städte und der raschen Entwicklung von Verkehrssystemen, Industrie und Technologien zur Energieerzeugung, zeichnen Seismometer nicht nur natürliche Signale, wie z.B. von Erdbeben auf, sondern registrieren auch Schwingungen, die durch die genannten Infrastrukturen verursacht werden - das sogenannte anthropogene seismische Rauschen.

Mit dem Ziel, erneuerbare Energien schnell auszubauen, um unabhängig von fossilen Brennstoffen zu werden, nahm die Anzahl der Windenergieanlagen in den letzten Jahrzehnten drastisch zu und wird in Zukunft noch weiter ansteigen. Diese Anlagen werden häufig in abgelegenen windhöffigen Gebieten errichtet, um die Auswirkungen auf die Umwelt zu minimieren und gleichzeitig die Windenergie optimal zu nutzen. Standorte mit ähnlichen Bedingungen werden auch von den Betreibern seismologischer Stationen bevorzugt, da hier das anthropogene seismische Rauschen vermindert auftritt. Windenergieanlagen werden durch den Wind und die darauffolgende Rotation des Rotors in Vibrationen versetzt, welche über das Fundament der Anlage in das Erdreich eingekoppelt werden. Auf diese Weise entstehen Bodenbewegungen, die sich in Form von seismischen Wellen ausbreiten. Viele Studien belegen bereits, dass der Betrieb von Windenergieanlagen Bodenbewegungen erzeugt, die mit Seismometern in mehreren Kilometern Entfernung gemessen werden können. Dies kann zur Folge haben, dass sich das Rauschniveau an seismischen Stationen erhöht und die Funktionalität und Datenqualität eingeschränkt wird. Betreiber von seismologischen Observatorien und Netzwerken (z.B. Saccorotti at al., 2011; Stammler & Cerana, 2016) belegen einen Anstieg der Rauschamplituden bei bestimmten Frequenzen zwischen 0.5 und 20 Hz, wobei diese Signale dem Betrieb umliegender Windenergieanlagen zuzuordnen sind. Der Amplitudenabfall der von Windenergieanlagen induzierten Signale mit der Entfernung wurde an vielen verschiedenen Standorten messtechnisch erfasst (Westwood & Styles, 2007; Neuffer & Kremers, 2017; Zieger & Ritter, 2018; Limberger et al., 2022; Gaßner et al., 2022), um den Störeinfluss von Windenergieanlagen in Abhängigkeit des Abstandes zu einer seismischen Station genau zu untersuchen. Auf dieser Grundlage wurden Ansätze zur Abschätzung der Amplitude entsprechender Signale im Fernfeld entwickelt, um sogenannte Schutzradien um eine seismische Station besser definieren zu können (z.B. Lerbs et al., 2021). Zur Beschreibung der Amplitudenabnahme mit der Entfernung verwendete Saccorotti et al. (2011) einen analytischen Ansatz unter Berücksichtigung von

Dämpfungsparametern des Untergrundes. Der Effekt von mehreren Windenergieanlagen eines Windparks wurde jedoch nicht genauer betrachtet. Gortsas et al. (2017) und Zieger at al. (2020) modellierten numerisch die Schwingungen einer einzelnen Windenergieanlage, um den Frequenzgehalt der Schwingungen und die Amplituden der entsprechenden Bodenbewegungen in der direkten Umgebung zu spezifizieren. Ihre Arbeit konzentriert sich dabei mitunter auf die Schwingungseigenschaften der Anlage und auf die Kopplung des Fundaments mit dem Erdreich. Darüber hinaus wurden die von einer einzelnen Windenergieanlage erzeugten seismischen Wellen von Abreu et al. (2022) mit numerischen Modellen untersucht. Sie führten Simulationen durch, um eine mögliche Verringerung der Störsignale durch strukturelle Maßnahmen (z. B. gefüllte Hohlräume oder topographische Effekte) nahe einer Windenergieanlage zu untersuchen. Auf der Basis von neuronalen Netzen entwickelte Heuel & Friederich (2022) eine Methode zur Filterung der Störsignale in seismischen Zeitreihen. Es ist allgemein bekannt, dass sich Seismometer in Bohrlöchern im Vergleich zu Stationen an der Oberfläche durch geringere Rauschpegel auszeichnen (Withers et al., 1996; Boese et al., 2015), was die Detektierbarkeit seismischer Ereignisse auch in städtischen Gebieten verbessern kann (Malin et al., 2018). Die positiven Auswirkungen von Bohrlochinstallationen zur Reduzierung der Signale von Windenergieanlagen wurden von Zieger und Ritter (2018) experimentell dargelegt. Sie verglichen in Bohrlöchern gemessene Signale mit entsprechenden Oberflächendaten und zeigen eine signifikante Verringerung der Signalamplituden, welche durch einen nahe gelegenen Windpark erzeugt werden. Neuffer and Kremers (2017) analysierten ebenfalls Daten von Bohrlochstationen, untersuchten aber nicht systematisch die Beziehung zu Oberflächendaten. Dennoch schätzen sie eine Verringerung des Rauschens um eine Größenordnung aufgrund der Bohrlochinstallation. Dies weist darauf hin, dass Bohrlochinstallationen eine wichtige Rolle bei der Verringerung des seismischen Rauschens von Windenergieanlagen an Seismometern spielen können. Ihre Möglichkeiten, Grenzen und die Abschätzung ihrer Wirksamkeit wurden bisher jedoch nicht im Detail untersucht. Obwohl bereits viel Wissen über die charakteristischen Signale, die von Windenergieanlagen ausgehen, vorhanden ist, waren die Ansätze, um diese Signale zu modellieren und vorherzusagen, weitgehend vereinfacht und berücksichtigten lediglich eine einzelne Windenergieanlage als seismische Quelle.

Diese Dissertation beschäftigt sich daher mit der Entwicklung und Anwendung von Methoden, um die komplexe Ausbreitung der Wellen, die von kompletten Windparks ausgehen, zu charakterisieren und zu simulieren. Simulationsergebnisse werden durch Echtdaten validiert, welche an Windenergieanlagen über lange Zeiträume gemessen wurden. Im Folgenden werden die in dieser Thesis beinhalteten drei wissenschaftliche Artikel zusammengefasst und die bedeutendsten Schlussfolgerungen dargestellt.

Im ersten Schritt werden seismische Signale von Langzeitmessungen (ca. 6 Monate), welche entlang eines 4 km langen Profils mit 14 Seismometern in einem kleinen Windpark in Uettingen bei Würzburg selbst gemessen wurden, analysiert. Aus den mit der Rotationsrate der Windenergieanlage korrelierten Leistungsdichtespektren lassen sich sieben diskrete Frequenzspitzen zwischen 1 Hz und 8 Hz eindeutig dem Betrieb der Windenergieanlagen zuordnen. Die zu diesen Frequenzspitzen zugehörigen Amplitudenabnahme sind abhängig von der Entfernung zum Windpark und zeigen einen nahezu perfekten linearen Zusammenhang zwischen der Signaldämpfung und der

Signalfrequenz, wobei die Signale mit hohen Frequenzen deutlich schneller abklingen. Signale mit tiefen Frequenzen (z.B. 1 Hz) lassen sich hingegen entlang des gesamten Profils nachweisen. Zusätzliche Messungen am Fundament der drei Windenergieanlagen zeigen darüber hinaus keine Korrelation zwischen den Schwingungen der einzelnen Windenergieanlagen. Dies bedeutet, dass die drei Anlagen unabhängig voneinander schwingen. Es wird also gezeigt, dass die Interferenz der Wellenfelder, die von mehreren Windenergieanlagen erzeugt werden, zeitlich eher zufällig als systematisch ist, sodass die erzeugten Wellen je nach Ort und Zeit destruktiv und konstruktiv interferieren können. Die Berechnung einer seismischen Abstrahlung eines Windparks unter der Annahme, dass alle Windenergieanalgen in Phase oder einer anderen systematischen Phasenkonstellation schwingen, ist demnach unzureichend. Als Lösung wird in dieser Arbeit eine Methode zur Berechnung einer repräsentativen seismischen Abstrahlung eines Windparks vorgestellt, welche die Amplitude von Oberflächenwellen in einer bestimmten Entfernung zu einem Windpark analytisch berechnet. Des Weiteren schlägt die Methode vor, viele Wellenfelder, die mit zufälligen Signalphasen der Quellen berechnet werden, zu mitteln. Dadurch deckt die resultierende Abstrahlung viele mögliche Konstellationen von interferierenden Wellenfeldern ab und wird nicht von einer bestimmten Interferenz der Wellenfelder dominiert. Unter Einbeziehung von Geschwindigkeits- und Dämpfungsparametern des Untergrunds ermöglicht die Anwendung dieser Methode auf den Windpark in Uettingen eine genaue Simulation der beobachteten frequenzabhängigen Amplitudenabnahme mit der Entfernung zum Windpark. Die durchgeführte Gittersuche nach den besten Modellparametern ergab schließlich, dass ein Zweischichtmodell im Vergleich zu einem homogenen Modell besser geeignet ist, um die Messdaten zu beschreiben. Daraus lässt sich bereits schließen, dass eine Schichtung im Untergrund Einfluss auf das Abklingverhalten der Wellen nehmen kann.

Auf Grundlage der Ergebnisse dieser Studie ist es empfehlenswert, möglichst lange Zeitreihen an einem Windpark aufzuzeichnen, um robuste Signalamplituden und Informationen über die Wellendämpfung ableiten zu können. Darüber hinaus sollte nicht davon ausgegangen werden, dass die Windenergieanlagen eines Windparks in Phase schwingen (z.B. gleichzeitig auf und ab), da eine spezifische Interferenz der Wellen erhebliche Auswirkungen auf die seismische Abstrahlung eines Windparks hat. Die entwickelte Methode ermöglicht zudem eine verallgemeinerte Vorhersage von abgestrahlten Amplituden im Fernfeld eines Windparks, da dessen Geometrie des Windparks variabel verändert werden kann.

Im weiteren Verlauf dieser Thesis wird die entwickelte Methode mit Hilfe fortgeschrittener dreidimensionaler Modelle erweitert, um die Ausbreitung kompletter Wellenfelder von mehreren Windenergieanlagen zu simulieren. Das Ziel ist die Simulation von Signalen, die vom Windpark Weilrod (nördlich von Frankfurt a. M.) erzeugt werden und die am seismologischen Observatorium TNS (Taunus) in 11 km Entfernung nachweisbar sind. TNS zeichnet sich durch ein sehr geringes seismisches Rauschniveau aus, was ein Grund dafür ist, dass eine Verdopplung des Rauschpegels durch den Betrieb des Windparks Weilrod bzgl. Signalen mit 1.15 Hz an TNS messbar ist. Die Taunus Region hat eine ausgeprägte Topographie, die mit Hilfe eines digitalen Höhenmodells in das numerische 3D-Modell einbezogen wird. Neben den bereits beschriebenen signifikanten Effekten

mehrerer Quellen in einem Windpark, verursacht die Topographie Amplitudenreduzierungen, welche durch die Streuung der Wellen zustande kommen. Der Vergleich von Simulationen mit und ohne Topographie zeigt jedoch auch lokale Signalverstärkungen, die insbesondere bei niederfrequenten Signalen auftreten. Diese Abschwächungen und Verstärkungen der Signale korrelieren räumlich mit der topographischen Gegebenheit. So wird die Wellenausbreitung z.B. entlang von Gebirgskämmen begünstigt und Signalverstärkungen sind vorwiegend an den vom Windpark abgewandten Berghängen erhöht. In Täler zeichnen sich eher Amplitudenreduzierungen ab. Diese Beobachtungen könnten daher eine Erklärung für die vom Windpark Weilrod verursachte relativ hohe Signalamplitude am seismologischen Observatorium TNS sein. Unter Berücksichtigung der Wellendämpfung zwischen Windpark und Observatorium werden die Modellierungsergebnisse durch die Messungen an der Station TNS validiert. Die Anwendung der Modellierung auf den Windpark Weilrod zeigt schließlich, dass die Topographie im Modell nicht vernachlässigt werden sollte, insbesondere dann nicht, wenn sie ausgeprägt ist. Täler und Berge können Streuung, aber auch Fokussierungseffekte auf die sich entlang der Oberfläche ausbreitenden Wellen verursachen und Störsignale am zum Windpark entfernten Seismometer begünstigen.

Zum ersten Mal werden die komplizierten Aspekte der Modellierung eines kompletten Windparks als seismische Quelle, die Auswirkungen der lokalen Topographie und die Dämpfung der Signale mit der Entfernung in einem Modell berücksichtigt und erlauben damit eine mögliche Erklärung und Vorhersage der Störamplituden, die am seismologischen Observatorium TNS gemessen werden. Darüber hinaus kann der vorgestellte Modellierungsansatz für die Abschätzung der Störamplituden vor der Errichtung eines neuen Windparks genutzt werden.

Der letzte Teil der Dissertation beschäftigt sich mit der Verringerung des Einflusses von Windenergieanlagen auf seismische Messungen mit Hilfe von Bohrlochinstallationen. Anhand von zweidimensionalen numerischen Modellen werden tiefenabhängige Amplituden von Signalen, die typischerweise von Windenergieanlagen erzeugt werden, bis zu einer Tiefe von 600 m simuliert. Die Auswirkungen der seismischen Geschwindigkeit, der Dämpfungseigenschaften und der Schichtung des Untergrundes werden systematisch analysiert. Die Parameterstudie zeigt, dass die Wirksamkeit von Bohrlöchern in der Nähe von Windenergieanlagen stark von der Länge der ankommenden Wellen abhängt und somit frequenzabhängig ist. Eine Bohrung von 200 m Tiefe kann bzgl. hoch-frequenten Signale (z.B. 10 Hz) sehr effektiv sein, insbesondere in Gebieten mit geringen seismischen Geschwindigkeiten, wie z.B. im Rheingraben. Wenn jedoch Signale mit Frequenzen von etwa 1 Hz (oder geringer) von Interesse sind (z. B. in Bezug auf die Beobachtung von teleseimischen Ereignissen), ist eine Bohrlochinstallation aufgrund der großen Wellenlänge und der damit verbundenen großen Eindringtiefe der Oberflächenwellen, welche vom Windpark ausgehen, weniger von Vorteil. Die Schichtung im Untergrund kann durch Reflexionen an den Schichtgrenzen erhebliche Auswirkungen auf das erzeugte Wellenfeld haben. Die Simulationsergebnisse zeigen, dass eine Deckschicht von 200 m Mächtigkeit die Wellen davon abhält, tiefere Schichten zu erreichen, was die Installation eines Bohrlochseismometers unter der Deckschicht begünstigen kann. Allerdings hängt dieser Effekt von der Mächtigkeit der Deckschicht und der Wellenlänge ab. Die

durchgeführten Abschätzungen der tiefenabhängigen Amplituden bei geschichtetem Untergrund werden schließlich mit Messdaten validiert, die an der Erdoberfläche und in der Tiefe von zwei Bohrlöchern mit 150 m und 305 m Tiefe (Zieger & Ritter, 2018) gemessen wurden. Dies bestätigt eine valide Anwendung der vorgestellten numerischen Abschätzungen, wodurch eine Bewertung der möglichen Rauschminderung durch Bohrlochinstallationen nach oder vor der Errichtung von Windparks in der Nähe einer seismischen Station ermöglicht und vereinfacht wird.

Im Rahmen dieser Arbeit werden experimentell gewonnen Messergebnisse, Verbesserungen der Modellierung und Vorhersage von seismischen Signalen, die von Windparks erzeugt werden, sowie Methoden zur Untersuchung der Auswirkungen von Wellenfeldinterferenzen, Topographie und Signaldämpfung mit der Entfernung und Tiefe vorgestellt. Die entwickelten Ansätze werden mit den Echtdaten validiert und bieten damit eine Antwort auf die Frage nach universellen Methoden, um Wellen von beliebigen Windparks und Untergrundeigenschaften simulieren zu können. Dennoch ist es sinnvoll, möglichen Weiterentwicklungen nachzugehen. Die vorgeschlagenen Methoden könnten durch die Prüfung verschiedener Quellenpolarisationen (z. B. Dipolmechanismen) erweitert werden, um den verschiedenen Bewegungsmustern des Fundaments einer Windenergieanlage Rechnung zu tragen. Dies könnte zu weiteren Effekten bzgl. Interferenzen und der Prognose der Amplitude führen. Darüber hinaus sind die Auswirkungen komplexerer Strukturen im Untergrund wie Störungen oder Grabenstrukturen von Interesse, da sie einen zusätzlichen Einfluss auf die Wellenausbreitung und Signalamplitude im Fernfeld eines Windparks haben könnten. Seismische Wellen können durch große Störungsszonen mit relativ zerklüftetem Gestein im Untergrund zusätzlich gedämpft werden. Solche Zonen zwischen einem Windpark und einem Seismometer könnten von Vorteil sein, um eine hohe Wellendämpfung entlang des Ausbreitungsweges zu erreichen. Im Gegensatz dazu führen Standorteffekte möglicherweise zu lokalen Amplitudenverstärkungen. Die Charakterisierung von Signalen mit einem seismischen Array könnte des Weiteren von großem Nutzen sein, da ein Array eine detailliertere Charakterisierung und Analyse der ankommenden Wellen erlaubt. Bisher wurden die seismischen Wellen mit Hilfe von Einzelstationen oder Profilmessungen analysiert, aber nicht mit speziell angeordneten Arrays im Fernfeld des Windparks. Schließlich würden weitere Validierungen mit umfangreichen Daten von verschiedenen (modernen) Windenergieanlagen, Bohrlöchern mit Seismometern und geografischen Standorten mit unterschiedlichen geologischen Bedingungen dazu beitragen, die vielseitigen Anwendungsmöglichkeiten der in dieser Arbeit entwickelten Methoden und durchführte Analysen weiter auszuarbeiten.

1. Introduction

1.1 Motivation

The earth's interior has been explored for decades, based on the observations made from seismic waves traveling through the globe. Seismic waves transport the geological imprint of the subsurface and thus provide information on the structure and composition of the earth. Highly sensitive seismometers enable the detection of very weak ground motions and deformation processes. Besides earthquakes or volcanic processes, seismometers are widely used to monitor global nuclear bomb tests or local micro seismic events, for example, those that are induced at geothermal power plants or by activities in quarries. With the growing population, the expansion of cities, and the fast development of traffic systems, industry, and technologies for energy production, seismometers also record anthropogenic seismic noise due to the vibrations produced.

Because of the aim to develop renewable energies rapidly, the number of wind turbines has been increased in recent years, and the number will continue to grow in the future. Wind turbines are often installed in remote areas to minimize their effect on the environment and to maximize the exploitation of the wind energy. Often, locations with similar conditions are also preferred by operators of seismic stations, due to the minimization of anthropogenic seismic noise. Many studies have proven that the operation of wind turbines can be measured by seismometers in terms of ground motions that occur several kilometers away from wind turbines. Hence, the seismic noise level can be significantly increased at the seismic station and might limit its functionality and data quality. Operators of seismological observatories and seismic networks (Saccorotti et al., 2011; Stammler & Cerana, 2016) have already observed a clear increase of noise amplitudes at specific frequencies between 0.5 Hz and 20 Hz and have been able to assign these signals to the operation of wind turbines at distances of up to 11 km.

The amplitude decay of wind-turbine-induced signals was measured at many different locations (Westwood & Styles, 2007; Neuffer & Kremers, 2017; Zieger & Ritter, 2018; Limberger et al., 2022; Gaßner et al., 2022) to examine an adequate distance between wind turbines and a seismic station. Based on this, Lerbs et al. (2021) proposed an analytical equation to estimate the amplitude of such signals in the far field with the aim of defining protection radii around a seismic station. Saccorotti et al. (2011) used an analytical approach, including damping parameters of the subsurface, to model the observed amplitude decays of noise amplitudes produced by several wind turbines; however, they did not consider possible effects of multiple wind turbines on the interference of the emitted wavefields. Gortsas et al. (2017) and Zieger et al. (2020) numerically modeled the vibrations of a single wind turbine to specify the wind turbine as a seismic source and the ground motions in the vicinity of a single wind turbine. They studied the interaction of the wind turbine foundation with the surrounding soil. Moreover, the seismic waves produced by a single wind turbine were investigated with numerical models by Abreu et al. (2022). They performed simulations to study a possible reduction of the noise by structural measures (e.g., filled cavities or topography) next to a wind turbine. Heuel and Friederich

(2022) developed a method to de-noise seismic time series from wind-turbine-induced noise, based on neural-network technology. Furthermore, it is commonly known that seismometers in boreholes are characterized by lower noise levels compared to stations at the surface (Withers et al., 1996; Boese et al., 2015), which can improve the detectability of seismic events even in urban areas (Malin et al., 2018). The beneficial effects of borehole installations on signals from wind turbines were shown by Zieger and Ritter (2018). They compared signals measured in boreholes with surface data and showed a significant reduction of the surface wave amplitude induced by a nearby wind farm. Neuffer and Kremers (2017) analyzed data from borehole stations as well but did not systematically study the relation to surface data. Nevertheless, they estimated a noise reduction by an order of magnitude due to the borehole installation. Borehole installations can play a relevant role in reducing the noise of wind turbines at seismometers. However, their capabilities, limitations, and the predictability of their effectivity have not been studied in detail.

Much knowledge is gained about the signals produced by wind turbines due to many experimental studies at wind farms. A few approaches to model and predict these signals are available but concentrate on a single wind turbine. Further development is necessary to achieve robust methods to understand and predict the complex propagation of wind-turbine induced wavefields or to reduce their impact on seismic stations.

One challenge of modeling the seismic waves that are produced by wind turbines lies within the multiple sources, since wind turbines are mostly arrange in wind farms. Neuffer et al. (2019) approximated the increase of noise by multiple wind turbines by a factor of $\sqrt{N}$, where N is the number of wind turbines. However, the interference of wavefields from multiple wind turbines is much more complicated and challenges the calculation of a representative seismic radiation from a wind farm (Limberger et al., 2021). Furthermore, various effects along the travel path affect the signal, and hence the noise amplitude, at the distant seismometer. Such effects can arise from the local geological setting of the subsurface, the topography between the wind farm and the seismic station, or the attenuation of the wave by specific rock properties (Limberger et al., 2022). It is known that seismometers in boreholes with an adequate depth can reveal significantly lower noise levels than seismic surface stations. The capability of borehole installations to reduce the impact from wind turbines was experimentally shown by Zieger and Ritter (2018); nevertheless, detailed estimations of the effectivity of such borehole installations on the various frequencies of the signals emitted by wind turbines were not performed.

By reviewing these points, this thesis aims to develop methods to improve the experimental and numerical analysis of seismic signals produced by wind turbines, including complex effects on the seismic waves caused by the multiple sources of a wind farm and the travel path. In focusing on the interference of the wavefields produced by multiple wind turbines and the effect of local topography and attenuation, the studies in this thesis help to better understand the seismic radiation from wind farms and the amplitude decay with distance and enable the prediction of noise amplitudes at seismometers in the far field. Moreover, borehole installations, as a solution to decrease the impact of wind turbines on seismic

measurements, are studied and the methods provided in the thesis, which complements possible measures for sustainable noise reduction at seismometers.

In the scope of this thesis, the following key questions are answered. These answers form the basis for the final summaries and conclusions made in Chapter 6.

1. Is it possible to reliably quantify the amplitude decay of seismic signals with distance from a wind farm and to model the seismic radiation from a complete wind farm including the wavefields produced by multiple wind turbines?

2. Are there significant effects of wavefield interferences, the local topography, and the wave attenuation on the seismic signals in respect to distance?

3. Is a borehole installation effective to reduce the impact of wind turbines on seismic measurements, and if so, what are the necessary criteria?

1.2 Outline of the Thesis

This thesis is a cumulative project including three separate papers with the common goal of finding advanced ways to model seismic waves that are produced by wind turbines and their possible impact on seismic measurements close to a wind farm. Each paper focuses on different topics; nevertheless, they share common approaches and ideas. Hence, there is some overlap between the introductions and sections about methodologies.

Chapter 2 introduces the basics of seismic wave propagation to prepare for the various topics treated in the three papers. The origin of seismic waves and their attenuation with distance are described, and specific characteristics concerning wind turbines as seismic sources are given. Furthermore, basis for computing synthetic seismograms are given.

The first paper (Chapter 3) focuses on the characterization and analytical modeling of the frequency-dependent amplitude decays derived from long-term measurements collected in the vicinity of a small wind farm close to Würzburg, Germany. The complex interference of wavefields from the multiple wind turbines is described by an analytical solution, which enables the modeling of the amplitude as a function of distance from the wind farm for various frequencies (Limberger et al., 2021).

The second paper (Chapter 4) presents the development of a numerical modeling method in three dimensions to predict the noise amplitudes that are produced by a wind farm north of Frankfurt am Main, Germany. These noise signals are measured at the permanent seismological station TNS, which is 11 km away from a wind farm. The modeling includes complex effects of the local topography, attenuation, and the interferences of the wavefields from seven wind turbines (Limberger et al., 2022).

The third paper (Chapter 5) deals with the reduction of the impact of wind turbines on seismic measurements using borehole installations. With numerical simulations, the effectivity and capability of such borehole installations is studied to estimate possible noise

amplitude reductions if a seismometer is deployed in a borehole close to a wind turbine. The estimations are validated with data from two real boreholes (Limberger et al., 2023, under review).

Chapter 6 contains a short summary of each paper and the conclusions of the thesis based on the results and findings of the three papers. Finally, the thesis ends with a short section about possible future developments to further improve the prediction of seismic signals that are produced by wind farms and their impact on seismic measurements at the earth's surface or in boreholes.

2. Seismic waves produced by wind turbines

This chapter introduces the basics of the propagation of seismic waves and their attenuation over distance from a wind farm, which is the seismic source. Furthermore, the main characteristics of the seismic signals that are produced by wind turbines are described. The basics to compute synthetic seismograms are given at the end of this chapter. Some of the points presented here are described in detail in the papers (Chapter 3, 4, and 5). Therefore, this chapter provides an overview of the theoretical context rather than a detailed and complete review of the methods used and described in the papers.

2.1 Seismic wave equation and attenuation

A medium shows an elastic deformation caused by an exciting force if the body returns to its original state after the deformation process of stress and strain. Based on the law of Hooke, the stress tensor $\boldsymbol{\tau}$ can be described as a tensor in dependency of the strain tensor $\boldsymbol{e}$ and the elastic tensor $\boldsymbol{c}$ (Aki & Richards, 1980):

$$\tau_{ij} = c_{ijkl} e_{kl} \tag{1}$$

This relation underlies three symmetries:

$$c_{ijkl} = c_{jikl} \quad (2) \qquad c_{ijlk} = c_{ijkl} \quad (3) \qquad c_{ijkl} = c_{klij} \quad (4)$$

Equations (2) and (3) are symmetries because of $\tau_{ij} = \tau_{ji}$ and $e_{kl} = e_{lk}$. Equation (4) is true for adiabatic deformation processes, which is given for seismic waves since the time scale of the elastic deformation during the seismic wave is much shorter than the time scale of thermal diffusion in the rock. These symmetries simplify $\boldsymbol{c}$ in case of an isotropic medium:

$$c_{ijkl} = \lambda \delta_{ij} \delta_{kl} + \mu\left(\delta_{ik}\delta_{jl} + \delta_{il}\delta_{jk}\right) \tag{5}$$

The only independent parameters here are λ and μ, the Lamé parameters, and δ_{ij} is the Kronecker dalta.

Furthermore, the strain can be described as the gradient of a displacement $\boldsymbol{u}$:

$$e_{ij} = \frac{1}{2}\left(\frac{\partial \mathrm{u_i}}{\partial \mathrm{x_j}} + \frac{\partial \mathrm{u_j}}{\partial \mathrm{x_i}}\right) \tag{6}$$

Equation (1) and (6) lead to the relation of stress and displacement:

$$\tau_{ij} = c_{ijkl} \frac{\partial u_k}{\partial x_l} \tag{7}$$

Seismic waves are time dependent, and the related elastic displacement of the particles in a homogenous isotropic medium is defined as follows (Shearer, 2009):

$$\rho \frac{\partial^2 u_i}{\partial t^2} = \frac{\partial \tau_{ij}}{\partial x_j} + F_i \tag{8}$$

In this equation ρ is the density and t is the time. F_i denotes additional body forces, e.g., gravitational forces. However, the gravity term can be neglected due to the relatively long wavelengths compared to seismic waves.

After substituting (7) in (8), it follows that

$$\rho \frac{\partial^2 u_i}{\partial t^2} = \frac{\partial}{\partial x_j}\left(c_{ijkl} \frac{\partial u_k}{\partial x_l}\right) \tag{9}$$

The written-out form of equation (9) in case of an inhomogeneous medium is

$$\rho \frac{\partial^2 u_i}{\partial t^2} = \frac{\partial}{\partial x_i}\left(\lambda \frac{\partial u_k}{\partial x_k}\right) + \mu\left(\nabla^2 u_i + \frac{\partial}{\partial x_i}\left(\frac{\partial u_k}{\partial x_k}\right)\right) + \frac{\partial}{\partial x_k}\left(\frac{\partial u_i}{\partial x_k} + \frac{\partial u_k}{\partial x_i}\right) \tag{10}$$

This is simplified for the homogenous medium as

$$\rho \frac{\partial^2 u_i}{\partial t^2} = \lambda \frac{\partial^2 u_k}{\partial x_i \, \partial x_k} + \mu\left(\frac{\partial^2 u_i}{\partial x_k \, \partial x_k} + \frac{\partial}{\partial x_i}\left(\frac{\partial u_k}{\partial x_k}\right)\right) \tag{11}$$

and can be written using the Nabla operator ∇ and the vector notation $\boldsymbol{u} = u_i$:

$$\rho \frac{\partial^2 \boldsymbol{u}}{\partial t^2} = (\lambda + 2\mu)\nabla(\nabla \cdot \boldsymbol{u}) - \mu \nabla \times \nabla \times \boldsymbol{u} \tag{12}$$

This seismic wave equation can be separated to find a solution for P-waves (compressional waves) and S-waves (shear waves) by taking the divergence and curl of equation (12). P-waves are polarized in the direction of the propagation, while S-waves are transversally polarized and have two components in horizontal (SH) and vertical (SV) direction. The P-

wave and S-wave can be expressed by the potentials ϕ (scalar unit) and $\boldsymbol{\Psi}$ (vector unit). Based on the Helmholtz decomposition theorem (Aki & Richards, 1980) it follows that

$$\boldsymbol{u} = \nabla\phi + \nabla \times \boldsymbol{\Psi}, \quad \nabla \cdot \boldsymbol{\Psi} = 0 \tag{13}$$

This further implies that

$$\nabla \cdot \boldsymbol{u} = \nabla^2\phi \tag{14}$$

and

$$\nabla \times \boldsymbol{u} = \nabla \times \nabla \times \boldsymbol{\Psi} = \nabla\nabla \cdot \boldsymbol{\Psi} - \nabla^2\boldsymbol{\Psi} = -\nabla^2\boldsymbol{\Psi} \tag{15}$$

The parts of the P-wave and S-wave of equation (11) are then

$$\nabla^2\phi = \frac{1}{\alpha^2}\frac{\partial^2\phi}{\partial t^2}, \quad \text{using } \nabla \cdot (\nabla \times \boldsymbol{\Psi}) = \mathbf{0} \tag{16}$$

and

$$\nabla^2\boldsymbol{\Psi} = \frac{1}{\beta^2}\frac{\partial^2\boldsymbol{\Psi}}{\partial t^2}, \quad \text{using } \nabla \times (\nabla\phi) = \mathbf{0} \tag{17}$$

The velocity of the P- and S-wave are defined by α and β:

$$\alpha = \sqrt{\frac{\lambda + 2\mu}{\rho}} \qquad \beta = \sqrt{\frac{\mu}{\rho}}$$

This implies that the velocity of the P- and S-wave depends on the Lamé parameters and the density of the medium. The wave equation depends on the velocity of the seismic body, whereby the P-wave velocity is always higher than the velocity of the S-wave. The explained equations are valid for cartesian coordinates; however, seismic waves are often described spherically since body waves propagate on a spherical surface through the medium.

In the case of spherical symmetry, the wave equation for P-waves is then (Shearer 2009)

$$\frac{1}{r^2}\frac{\partial}{\partial r}\left(r^2\frac{\partial^2\phi}{\partial r}\right) = \frac{1}{\alpha^2}\frac{\partial^2\phi}{\partial t^2} - 4\pi\delta(r)f(t) \tag{18}$$

with the radial distance r to a point source with a source time function $4\pi\delta(r)f(t)$ at the origin.

A solution for equation (18) at $r \neq 0$ is

$$\phi(r,t) = \frac{1}{r}\ S(t \pm r/\alpha) \tag{19}$$

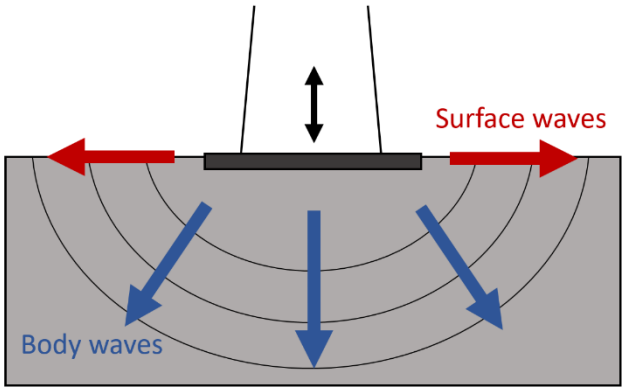

Figure 1 Illustration of the propagation of body waves and surface waves, produced by a wind turbine.

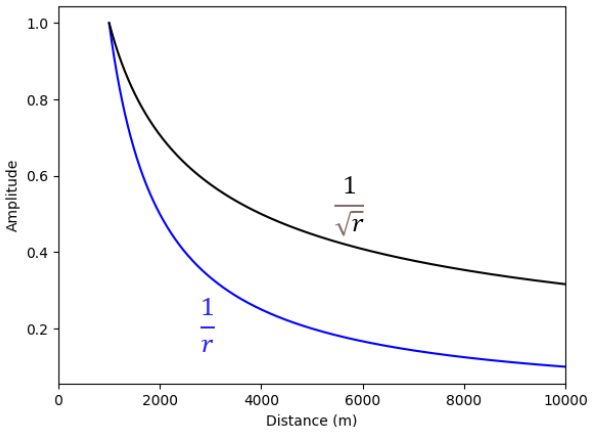

Figure 2 Geometrical spreading of surface waves ($1/\sqrt{r}$) and body waves ($1/r$), normalized to an amplitude of 1 at a distance of 1000 m.

This solution expresses a wave that is propagating radially away from a source, and S denotes an arbitrary function solving equation (18) (e.g., a sine function). The factor $1/r$ expresses the decay of the amplitude of the body wave with radial distance to the source. This phenomenon, known as geometrical spreading, is due to the expansion of the wave front of body waves on a spherical surface.

Seismic body waves interact with the earth's surface, which generates two types of surface waves: Love waves and Rayleigh waves. Love waves are polarized transversally to the wave propagation direction and are generated by multiple interferences of SH-waves at the surface. Rayleigh waves are more complex since they are generated by SV- and P-waves. This implies that they have a polarization in radial direction, in addition to an SV component. Their particle motion consists of a retrograde elliptical motion in the vertical plane, parallel to the direction of propagation. Rayleigh waves exist at every free surface. Surface waves expand their wave front on a cylindrical area (e.g., radially propagating away from a point at the surface) and not a sphere; the geometrical spreading of surface waves is scaled by $1/\sqrt{r}$ for signal amplitudes, which means in general that surface waves have a lower loss of energy due to geometrical spreading (Figure 2). Furthermore, surface waves travel slightly slower than

S-waves. I refer to Aki and Richards (1980) and Shearer (2009) for detailed information about the generation surface waves.

In addition to the geometrical aspects of the wave energy loss, seismic waves underlie the effects of scattering and the intrinsic attenuation because of inelastic processes of the rock. Scattering of the wave is due to small inhomogeneities of the subsurface by which the wave loses its energy during the propagation. Furthermore, surface waves can scatter, e.g., due to pronounced topography. Usually, the amount of wave scattering increases with increasing frequency due to a shorter wavelength of the wave, which in turn makes the wave more sensitive to inhomogeneities of the subsurface or topography. Intrinsic attenuation depends on the properties of the rock and the wavelength of the seismic wave (Eulenfeld & Wegler, 2016). According to Shearer (2009), the amount of the loss of energy per cycle of the seismic wave is expressed by the value of the quality factor Q:

$$Q(\omega)^{-1} = \frac{\Delta E}{2\pi E} \tag{20}$$

Here, ω is the angular frequency. E is the peak strain energy and ΔE is the energy loss per cycle. High values of Q mean a weak attenuation. In seismology, Q is assumed to be >> 1, and the amplitude decay due to intrinsic absorption is then approximated by

$$A(r) = A_0 e^{-\omega(r-r_0)/2cQ} = A_0 e^{-\pi f(r-r_0)/cQ} \tag{21}$$

where r is the radial distance from the source measured in direction of the propagation, A_0 is the reference amplitude at the corresponding reference distance r_0 from the source, c is the velocity of the seismic wave (P-, S- or surface waves), and f is the frequency of the wave. The value of Q depends on the type of wave, where Q is generally higher for the P-wave than for the S-wave or surface waves, due to higher energy losses by friction of the shear motion. Equation (21) indicates that high frequency waves attenuate more strongly than low frequency waves, which is of importance for seismic waves that are produced by wind turbines. Waves with a high frequency have more cycles on a section of distance compared to low-frequency waves. As shown, the amplitude decay of a seismic wave is defined by its geometrical spreading, intrinsic attenuation, and the scattering. In many publications concerning seismic signals from wind turbines, the amplitude decay with distance from a seismic source is described by a single power law r^{-b}, where the exponent b defines the amount of damping and hence incorporates all mentioned types of attenuation (e.g., Stammler & Cerana, 2016; Zieger & Ritter, 2018). This enables a fast and practical solution to quantify the attenuation of seismic waves in a specific region or geological environment; however, the b-value is not physically linked to geophysical parameters (e.g., the quality factor Q), which is a disadvantage.

Besides the attenuation of waves with distance along the surface of the earth, surface waves have a penetration depth. This means that the amplitude of a surface wave generally decreases in respect to the depth. The aspect of amplitude decrease with depth is advantageous for obtaining low seismic noise levels at seismometers when they are deployed in boreholes of an adequate depth. Borehole installations can increase the earthquake detectability and decrease the amplitude of seismic signals from noise sources in the vicinity of the seismometer. The effectivity of such borehole installations concerning wind-turbine induced noise is studied in detail in Chapter 5. For a homogeneous medium, the amplitude decay with depth (Figure 3) can be described analytically (Barkan, 1962; Richart, 1970). If the medium is not homogeneous, this behavior becomes more complex due to possible disturbances by wave-guiding layers in the subsurface, wave reflections, and wave refractions. While the amplitude of the horizontal component of a Rayleigh wave decreases relatively quickly with depth, the vertical component reaches deeper. Again, this depends dominantly on the wavelength, which implies that low-frequency waves and high-velocity media lead to a deep penetration depth of Rayleigh waves, due to the larger wavelength. Because of the penetration depth of surface waves, the general attenuation of the wave is also controlled by the characteristics of the near-surface geology, which in turn can affect the amplitude decay with distance.

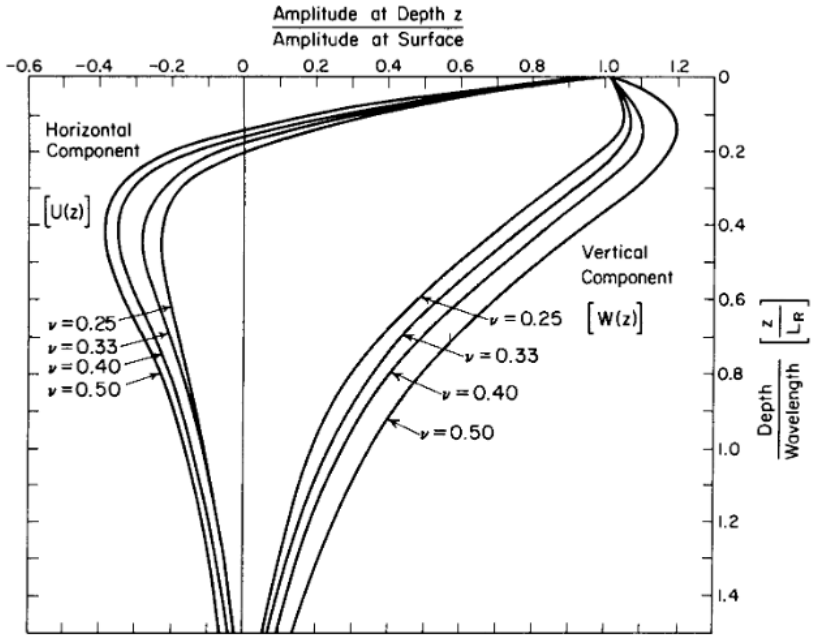

Figure 3 The ratio of wave amplitude depending on depth, wavelength, and the Poisson's ratio of the rock (by Richart et al., 1970).

The general attenuation of seismic waves that propagate within an inhomogeneous medium can be affected by refractions and reflections the waves at layer boundaries and geological structures in the subsurface. The refracted and reflected signals are often used to localize structures in the subsurface and to determine geophysical parameters of the geological layers, since seismic waves are sensitive to changes of the velocity and density of the medium (Shearer, 2009). Regarding seismic noise from sources at the surface (e.g., wind

turbines), reflections or refractions along near-surface layer boundaries are of interest since they might generate modulations of the waves measured at the surface or affect the general attenuation of the wave. However, this depends on the geometry of the geological setting (e.g., layer thicknesses) but also on the wavelength, and hence the frequency of the seismic wave. In addition, the local topography can have effects on the wave propagation in terms of scattering, which consequently causes an additional energy loss and constructive modulations of the wave, which can result in amplitude amplifications in the far field of a seismic source (Lee et al., 2008, Limberger et al., 2022). Besides the geometrical setting of source, receiver, and the shape of the topography, such topographic effects depend on the wavelength. Therefore, the frequency content of the signals of interest is highly relevant.

Typical signals from earthquakes or explosions are characterized by a transient signal with a specific beginning and end in time. Their frequency content can be determined appropriately based on the amplitude spectra of the corresponding signals. The frequency content of various earthquake signals covers a wide range of signal periods from milliseconds to many seconds, depending on the distance between the receiver and seismic source and the mechanism of the rupture. Compared to this, the signals from e.g., the atmosphere, traffic, and other anthropogenic sources (such as wind turbines) are continuous and persist in time. These types of signals $S(t)$ are often confined by a specific frequency band and are better characterized using the power spectral density (PSD) *P(ω),* generally defined as (Aki & Richards, 1980):

$$\mathrm{P}(\omega) = \int_{-\infty}^{\infty} \langle S(t)S(t+\Delta t)\rangle \, e^{-i\omega\Delta t} d(\Delta t) \tag{22}$$

where ⟨ ⟩ denotes the average over time and *i* is the imaginary unit. The expression $\langle S(t)S(t+\Delta t)\rangle$ is the autocorrelation of $S(t)$, which implies that the signal is analyzed for similarity with a time-lagged version (lagged by Δt) of itself. $P(\omega)$ is the Fourier transform of the autocorrelation function. By definition, $\langle S(t)S(t+\Delta t)\rangle$ is the mean of $S^2(t)$ in case of $\Delta t = 0$, which is furthermore the variance of the signal and can also be defined as the power of a stationary process $S(t)$. The power of a signal is the signal's energy per a specific time window. This is practical concerning periodic and continues signals (e.g., signals from wind turbines), since the total energy of the signal would become infinite. Compared to an amplitude spectra and its corresponding phase spectra, the PSD does not provide information about the phase of the signal. However, with the calculation of the PSD of a continuous signal, the frequency content can be appropriately characterized. In terms of seismological recordings with discrete time samples and a finite length, the signal $S(t)$ is typically divided into *N* (overlapping) time segments with a time period from t_i to t_{i+1}. After tapering the cut signal, the PSD is then calculated for each segment. All PSDs are averaged to derive an overall PSD of the signal (Welch, 1967):

$$\mathrm{P}(\omega) = \frac{1}{N}\sum_{n=1}^{N} S^2(\omega) \tag{23}$$

with the Fourier transform

$$S(\omega) = \int_{t_i}^{t_{i+1}} S(t) e^{-i\omega t} dt \tag{24}$$

The unit of $P(\omega)$ is the squared unit of $S(t)$ divided by the frequency (e.g., (m/s)²/Hz, in case of ground velocity).

2.2 Wind farms as sources of seismic waves

Seismic waves that are produced by wind turbines are based on the general physics of elastic waves and their attenuation with distance and depth, as described in section 2.1. However, in the scope of this thesis, some specific characteristics are important for understanding the seismic radiation from wind farms. Wind turbines transform wind power into electrical power using a generator and are coupled to the soil by a foundation that transfers the vibration of the tower, rotor, and rotor blades to the subsurface. As mentioned before, this interaction produces seismic waves that can be measured by nearby seismometers. Furthermore, the installation of a new wind farm close to a seismic station or network is detectable in the seismic records (Stammler & Cerana., 2016). The vibration of the wind turbine that is transferred to the subsurface is dominated by the bending of the tower, which has specific eigenfrequencies caused by various bending modes (Zieger et al., 2019). Every time the blade passes the tower, it is excited for oscillation. The frequencies of the signals that are typically emitted by wind turbines are between 0.5 Hz and 20 Hz (Styles et al., 2005; Saccorotti et al., 2011; Gaßner & Ritter, 2022), covering the different oscillation modes of the wind turbine, which are designed specifically to avoid resonances of the construction. Depending on the type of earthquake, this frequency band is shared with the signals from an earthquake. The motion of the wind turbine's foundation is very complex since it can adapt to up and down motion, tilting, and circulating motions (Neuffer et al., 2021). The different patterns of motions are of interest in the very near field of the wind turbine to understand and describe the wind turbine itself as a seismic source. It is commonly understood that primarily surface waves are produced, dominated by Rayleigh waves (e.g., Styles, 2005). However, Neuffer et al. (2021) showed that for some frequency bands, Love waves are generated as well. Seismic stations that are deployed in the vicinity of a wind farm show a significant increase of the noise level at specific frequencies when the wind turbines are operating. It is shown that the noise level clearly correlates with the rotor speed of the wind turbine and wind speed (e.g., Figure 4). This correlation follows the

characteristics of the wind turbines' operation (Lerbs et al., 2020). Typically, wind turbines switch on their rotation when the wind speed exceeds approximately 3 m/s.

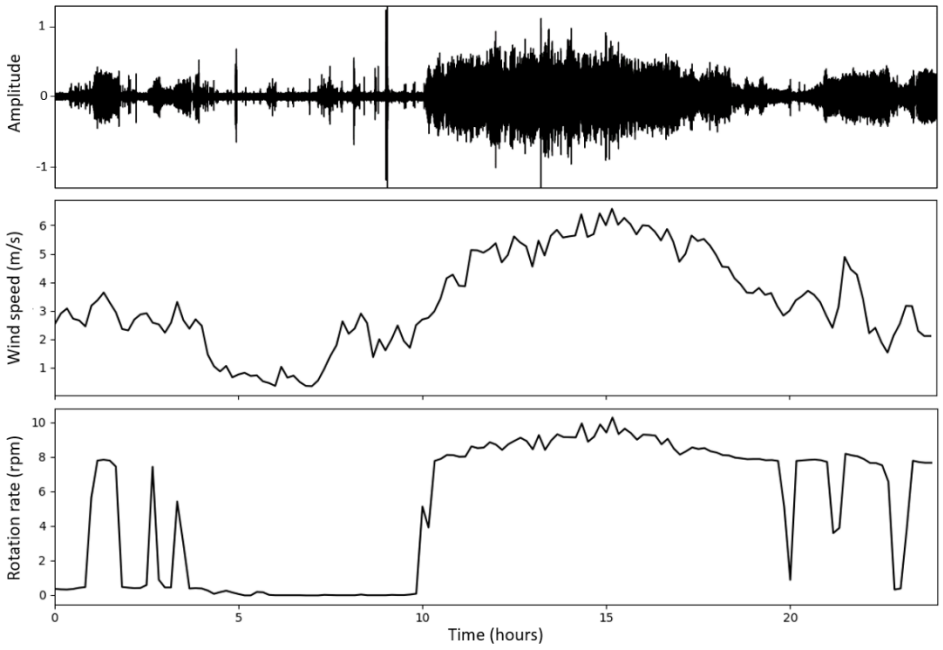

Figure 4 Example of a correlation between signal amplitude (top), wind speed (center), and rotation rate (bottom) in rounds per minute (rpm) over a time period of 24 hours. The distance between wind turbine and seismometer in this example is about 250 m. The time series is filtered to a frequency range of 2 Hz to 6 Hz. After the time stamp of 10 hours, the wind speed increases, and therefore, the wind turbine starts to rotate, which significantly increases the signal amplitudes at the seismometer.

The level of noise increase depends on the distance between the seismometer and the wind turbines, due to the geometrical spreading and the attenuation of the wave. This implies that the geology of the subsurface between the wind farm and the seismometer plays a relevant role. If the subsurface is dominated by relatively compact rock with weak attenuation, the impact of the wind turbines on a nearby seismometer is likely higher than in an area that is defined by strong attenuation, as shown in the previous chapter.

To approach the modeling of a single wind turbine as a seismic source and estimate the amplitude decay with increasing distance (in the far field) from the wind turbine, it is suitable to assume a sinusoidal up-and-down motion of the foundation (Limberger et al., 2021):

$$S(t,r) = A\,cos(kr - \omega t + \varphi) \tag{25}$$

Equation (25) is an analytical solution of the seismic wave equation and depends on the amplitude A of the signal, wavenumber k, radial distance r, and the signal phase φ. The signal frequency f is covered by $\omega = 2\pi f$.

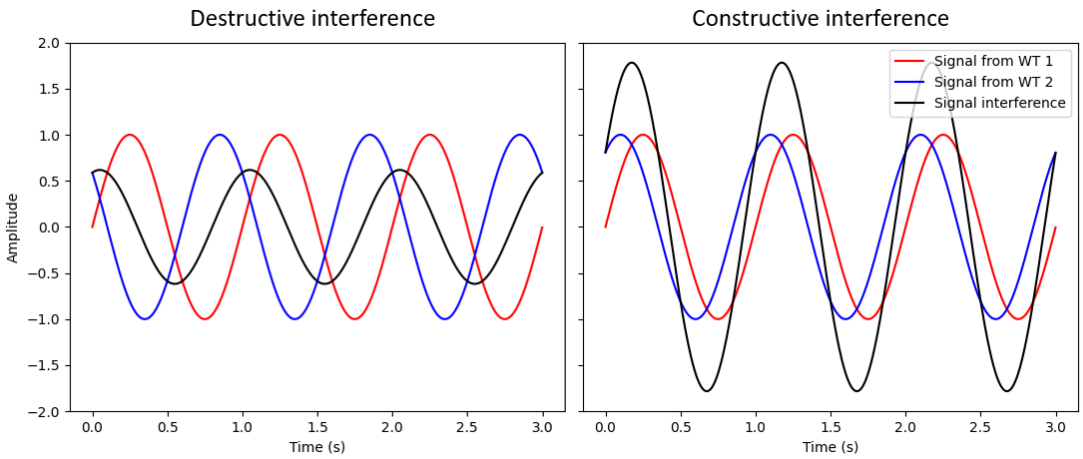

Figure 5 Exemplary demonstration of a destructive (left) and constructive (right) interference of 1 Hz signals from two wind turbines.

Usually, a number of wind turbines are located closely to each other, arranged in a wind farm. Equation (25) can then be applied for every wind turbine; however, the question of the interference of the single wavefields of multiple wind turbines is very important to be considered to model the seismic radiation from a wind farm. In case of $\varphi = 0$ (for all wind turbines of the wind farm), all wind turbines would vibrate in phase, which furthermore would generate one specific interference pattern of the emitted wavefields since the wave would locally interfere constructively and destructively (Figure 5), depending on the geometry of the wind farm and the wavelength. Because it is shown that multiple wind turbines vibrate independent of each other, the calculation of one specific interference pattern would not lead to a representative radiation (Limberger et al., 2021, 2022). One focus of this thesis is the solution of this problem, which is demonstrated in detail in Chapters 3 and 4. By applying the "phase shift elimination method," it is possible to estimate the signal amplitude in the far field of multiple wind turbines while avoiding the domination of one specific interference of the wavefields. Hence, the radiation pattern of surface waves can be simulated analytically including aspects of wave damping with distance (Limberger et al., 2021). Such an analytical approach is sufficient to make estimations for relatively simple geological models but is limited if the subsurface is complex or in the presence of pronounced topography. Then, advanced numerical methods are better suited to compute synthetic seismograms including more complexity of the model.

2.3 Forward modeling: Computing synthetic seismograms

The possibilities to calculate synthetic seismograms vary from simple one-dimensional analytical solutions to very complex numerical algorithms. The most suitable approach should be chosen depending on the problem to be solved. However, all methods share one goal, which is to compute a synthetic seismogram at a specific receiver location based on making assumptions of the source and model. This is a classic forward modeling problem. Simple analytical solutions are limited concerning complicated sources and models and become inaccurate with increasing complexity, whereas modern numerical methods can solve the complex wave propagation through a heterogeneous medium (Shearer, 2009). The increasing capability of computational power enables the application of numerical solvers on very complicated models with high accuracy of the synthetic seismograms. Such methods are primarily finite-element methods (FEM), finite-difference methods (FDM), and spectral-element methods (SEM). These methods solve the wave equation over a set of grid points or model elements that discretize the medium. The advantage of these numerical methods is the applicability on complicated models with almost arbitrary structures. The costs of computation increase with the size and number of necessary elements, which in turn is regulated by the wavelength of interest; 3D models are more costly than the corresponding 2D models. The wave equation is solved over discrete timesteps, and a complete synthetic wavefield is calculated, including body waves and surface waves. The challenge in using FDM is the handling of adequate absorbing boundaries at sharp interfaces (e.g., topography) where FEM is the better choice. FEM and FDM require many grid points to resolve one wavelength appropriately (roughly 20 grid points according to Shearer [2009]). The great advantage of SEM is the relatively low computational cost since SEM require much less grid points per wavelength (roughly 2 grid points) to accurately simulate a signal. Of course, in the case of sharp changes of the velocity in the model, more grid points are required. Having been developed mainly by Komatitsch et al. (2002), SEM gained much attention in the last few years and is applied for wavefield modeling at all scales, from local micro seismic events to global seismology. Nevertheless, inaccuracies of synthetic seismograms occur and have their origin mostly in wrong assumptions of the model or very complicated models that force the method to its limits. The modern techniques to produce synthetic seismograms and the increasing computer capacities support the research in the wide field of seismology tremendously and make numerical studies very effective.

The software package *Salvus* by Mondaic AG/Ltd provides techniques and tools to perform wavefield modeling based on SEM in two and three dimensions (Afanasiev et al., 2018; Afanasiev et al., 2019). *Salvus* was used for all numerical simulations performed within the research for this thesis; therefore, the most important aspects of numerically modeling seismic wave propagation with SEM are described in the following paragraphs. The possibility of running the wavefield calculations parallelized on high-performing computing clusters for variable meshes of the model enables the forward modeling of accurate and highly resolved wavefields, including elastic and acoustic domains, topography, anisotropy, anelasticity, and attenuation. Basically, the wave equations

established in section 2.1 are solved by *Salvus* for each time step of the simulation and mesh element within the model. However, boundary conditions at the boundaries of the computational domain (Figure 6) need to be defined in order to obtain a unique solution (Afanasiev et al., 2019). The outer surface of the model (Earth's surface) needs to be free of tractions, which implies that traction (and hence stress $\boldsymbol{\tau}$) in normal direction $\vec{n}$ out of the domain is disabled, which is known as the free-surface condition:

$$\tau_{ij}\,\vec{n} = 0 \tag{26}$$

Interface conditions define the link of interfaces within the model with different physical properties or discontinuities. There are two types of conditions, one for a solid-solid interface and another for a solid-fluid interface. The solid-solid condition does not involve a change of the physics of wave propagation since both media are based on elastic wave propagation. The jump of the quantity, e.g., displacement, is entirely due to the discontinuity of the material property. Hence, the solid-solid condition requires the continuity of displacement and traction. On the other hand, the fluid-solid condition involves a change of physics since fluids are characterized by an acoustic wave propagation with an absence of shear waves. Such differentiation is necessary to allow for correct wave transmission and reflection at interfaces of two different media. Waves that hit the artificial boundaries of a finite model (e.g., at the bottom) should not be reflected to avoid artificial signal amplitudes in the synthetic seismograms. One approach to absorb these waves on the boundaries is to relate the traction at the boundary to the normal component ($\partial_t u_{\vec{n}}$) and tangential components ($\partial_t u_{\vec{\tau_i}}$) of the particle velocity (Clayton & Enquist, 1977; Komatitsch et al., 2000):

$$\tau_{ij} \cdot \vec{n} = \alpha\rho\partial_t u_{\vec{n}} + \sum_i \beta\rho\partial_t u_{\vec{\tau_i}} \tag{27}$$

The velocity of the P-wave and S-wave are α and β. The absorbing condition (27) is a simplified approximation, which still allows for small reflections of the wave at the artificial boundaries. However, the order of amplitude is just a small fraction of the amplitude of the direct waves from the source and has no significant impact on the synthetic seismograms. Furthermore, this approach has low computational costs, which is a general advantage. To improve the absorption in case of waves with relatively steep incident angles at the boundaries, *Salvus* can include an artificial sponge layer at the boundary, which additionally tapers the wave and further decreases reflections at the boundaries. Besides the mentioned options of wave absorptions, perfect matched layers (PML) are often implemented in modeling software to enable a very effective wave attenuation in a layer attached to the computational domain. However, with regard to complex models with various physical properties and discontinuities, PML is not yet sufficient and requires more research.

In addition to boundary, interface, and absorbing conditions, the initial condition defines the status of the model at t=0. Typically, the computational domain is under rest initially, which leads to the assumption that there is no displacement.

$$\boldsymbol{u}(\boldsymbol{x}, t = 0) = 0 \quad , \quad \partial_t \boldsymbol{u}(\boldsymbol{x}, t) = 0 \tag{28}$$

A crucial aspect of modeling seismic wavefields is the meshing of the model. The model is discretized in elements, for which the wave physics are calculated. A discretization is necessary in time (time step) and space (element size and grid points per element). Of course, the refinement of a model is higher the more elements that are used. However, another quantity to control the refinement of the mesh is the polynomial order of each element, which implies that an element has more grid points if the polynomial order is high (Figure 6). A high polynomial order efficiently decreases the error of the numerical simulation, and through that a lower number of elements per wavelength is necessary, which is generally advantageous for reducing computational costs.

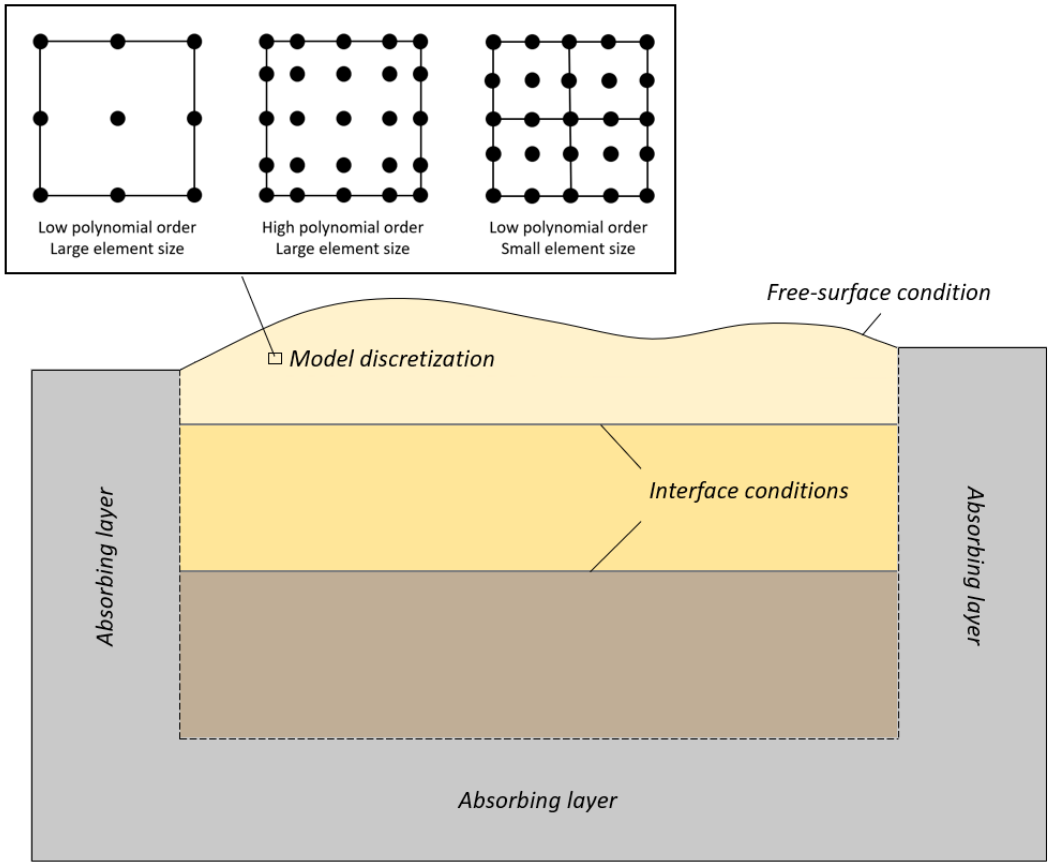

Figure 6 Schematic illustration of a 2D computational domain including boundary conditions and the model discretization based on polynomial order and element size or grid-spacing (The illustration of the elements is modeled after Afanasiev et al. [2019].).

Nevertheless, sharp discontinuities within the model require relatively small elements at the interface to account for the change of material properties and the corresponding change of the wave across the boundary. Additionally, the solving becomes intensive with increasing polynomial order. Hence, a suitable compromise of polynomial order and element size is important to derive accurate results and to optimize the computational costs. In the event that the refinement is too low, the spatial dispersion error increases and simulation results become inaccurate. According to the developer of *Salvus*, the error can be approximated by

$$\epsilon(p) \approx \frac{1}{2p(2p+1)}\left(\frac{p!}{(2p)!}\right)\left(\frac{2\pi}{n_\lambda}\right)^{2p} \tag{29}$$

where p is the polynomial order and n_λ is the number of wavelengths per element. With increasing polynomial order and number of elements, the error decreases. However, highly refined models require small time steps of the simulation, which again increases the computational costs. Generally, in SEM the time step needs to be below a specific value to guarantee a convergence of the simulation. An example of such a condition is the Courant–Friedrichs–Lewy (CFL) condition, which is widely used in SEM (details are described in Courant et al., 1967). The CFL condition is a function of the seismic velocity and element size of the mesh. This implies that the lower the velocity, the shorter the wavelength and the smaller the necessary element size. In addition, similar to the spatial dispersion error, the temporal dispersion error should be minimized. This error is proportional to the product of time-step size and wave frequency. Hence, the time step must become smaller with increasing frequency to avoid an increase of the temporal dispersion error.

As presented in this section, an accurate modeling of wavefield propagation in three dimensions using complex models requires intensive mathematical solutions of a number of problems, such as wave equation, boundary conditions, absorbing boundaries, and temporal and spatial refinement of the model. At the same time, these solutions should be minimized concerning computational costs to enable a practical application.

Personal contribution

Please note that I am the first author of the papers in this thesis. The used methods of analysis and modeling were performed upon consultation with my supervisor, Prof. Dr. Georg Rümpker. I experimentally collected data used in Chapter 3. I analyzed the majority of the data used for the papers, set up the analytical and numerical models and produced and processed the simulation data. The interpretation of the results was discussed based on the contribution of all co-authors. I wrote the initial versions of the papers and the co-authors edited the manuscripts before submission. The author contributions to each chapter are listed below and are at the end of the corresponding paper.

Chapter 3: Seismic radiation from wind turbines: observations and analytical modeling of frequency-dependent amplitude decays
F. Limberger, M. Lindenfeld, H. Deckert, G. Rümpker
FL and ML performed the field work and data analysis. FL set up the modeling approach and performed model calculations. GR participated in data interpretation, model development and supervised the article outline. HD and GR initiated the project and provided the computational framework. FL, ML, GR and HD edited the article.

Chapter 4: Development of a numerical modelling method to predict the seismic signals generated by wind farms
F. Limberger, G. Rümpker, M. Lindenfeld, H. Deckert
F.L. processed the seismic data and performed the numerical simulations. G.R. provided the motivation for this study and the seismic data, participated in developing the model, and supervised the writing of the article. F.L. and G.R. interpreted the results and completed the manuscript together. M.L. was involved in the measurements at the wind farm. F.L., G.R., M.L. and H.D. each edited the article.

Chapter 5: The impact of seismic noise produced by wind turbines on seismic borehole measurements
F. Limberger, G. Rümpker, M. Lindenfeld, H. Deckert
All authors developed the thematic idea of the study. F.L. performed the numerical simulations and processed the data. G.R. participated in developing the model, and supervised the writing of the article. F.L., M.L., and G.R. interpreted the results. F.L., G.R., M.L. and H.D. each edited the article.

3. Seismic radiation from wind turbines: observations and analytical modeling of frequency-dependent amplitude decays

This chapter has been **published** in:

Limberger, F., Lindenfeld, M., Deckert, H., and Rümpker, G. (2021): Seismic radiation from wind turbines: observations and analytical modeling of frequency-dependent amplitude decays. Solid Earth, 12, 1851–1864, doi:10.5194/se-12-1851-2021

Solid Earth, 12, 1851–1864, 2021
https://doi.org/10.5194/se-12-1851-2021

Solid Earth Open Access EGU

Seismic radiation from wind turbines: observations and analytical modeling of frequency-dependent amplitude decays

Fabian Limberger[1,2], **Michael Lindenfeld**[1], **Hagen Deckert**[2], **and Georg Rümpker**[1]

[1]Institute of Geosciences, Goethe-University Frankfurt, 60438 Frankfurt am Main, Germany
[2]Institute for Geothermal Resource Management (igem), 55411 Bingen, Germany

Correspondence: Fabian Limberger (limberger@igem-energie.de)

Received: 1 March 2021 – Discussion started: 11 March 2021
Revised: 14 July 2021 – Accepted: 15 July 2021 – Published: 19 August 2021

Abstract. In this study, we determine spectral characteristics and amplitude decays of wind turbine induced seismic signals in the far field of a wind farm (WF) close to Uettingen, Germany. Average power spectral densities (PSDs) are calculated from 10 min time segments extracted from (up to) 6 months of continuous recordings at 19 seismic stations, positioned along an 8 km profile starting from the WF. We identify seven distinct PSD peaks in the frequency range between 1 and 8 Hz that can be observed to at least 4 km distance; lower-frequency peaks are detectable up to the end of the profile. At distances between 300 m and 4 km the PSD amplitude decay can be described by a power law with exponent b. The measured b values exhibit a linear frequency dependence and range from $b = 0.39$ at 1.14 Hz to $b = 3.93$ at 7.6 Hz. In a second step, the seismic radiation and amplitude decays are modeled using an analytical approach that approximates the surface wave field. Since we observe temporally varying phase differences between seismograms recorded directly at the base of the individual wind turbines (WTs), source signal phase information is included in the modeling approach. We show that phase differences between source signals have significant effects on the seismic radiation pattern and amplitude decays. Therefore, we develop a phase shift elimination method to handle the challenge of choosing representative source characteristics as an input for the modeling. To optimize the fitting of modeled and observed amplitude decay curves, we perform a grid search to constrain the two model parameters, i.e., the seismic shear wave velocity and quality factor. The comparison of modeled and observed amplitude decays for the seven prominent frequencies shows very good agreement and allows the constraint of shear velocities and quality factors for a two-layer model of the subsurface. The approach is generalized to predict amplitude decays and radiation patterns for WFs of arbitrary geometry.

1 Introduction

In recent years, debates on the emission of seismic waves produced by wind turbines (WTs) and its potential effects on the quality of seismological recordings have led to increased research efforts on this topic. The main objectives are the characterization of WT-induced seismic signals, the definition of protection radii around seismological stations, and the modeling-based prediction of WT effects on seismological recordings in advance of the installation of WTs. Styles et al. (2005) reported about discrete frequency peaks in seismic noise spectra that increase with wind speed and the rotation rate of a nearby WT and assigned the observed peaks to vibration modes of the WT tower and rotor rotation. Zieger and Ritter (2018) and Stammler and Ceranna (2016) confirmed discrete frequency peaks between 1 and 10 Hz and analyzed signal amplitude decays with distance to the WTs described by a power law. Saccorotti et al. (2011) observed seismic signals with a frequency of about 1.7 Hz that were associated with WTs at distances of up to 11 km. Friedrich et al. (2018) used a migration analysis to identify seismic signals from nearby wind farms (WFs) and were able to distinguish between various WFs based on differences in frequency content. Polarization analyses was used by Westwood and Styles (2017) to show that Rayleigh waves dominate the wave field emitted from WTs. This observation was confirmed by numerical simulations (Gortsas et al., 2017). The increase of the noise amplitude with the square root of the number of

WTs ($\sqrt{N}$) was observed by Neuffer et al. (2019) based on WT shutdown tests. Lerbs et al. (2020) proposed an approach to define protection radii, e.g., 3.7 km around the Collm Observatory (CLL) in Germany, using a power law to describe the spatial wave attenuation. Furthermore, the ground motion polarization near a single WT was analyzed and provided insights into the interaction of WT nacelle movement and emitted seismic signals.

Approaches to model the seismic radiation from WTs are rare and focus mostly on modeling the ground vibration of a single WT (Gortsas et al., 2017) or its operational components only (e.g., Zieger et al., 2020) but not on wave field propagation considering superimposed wave fields and amplitude decay with distance to multiple WTs simultaneously. However, Saccorotti et al. (2011) used an analytical approach to model the observed amplitude decays by summing up the calculated noise amplitudes produced by several WTs, including an intrinsic attenuation law, but they did not study possible effects of multiple WTs on the interference of the emitted wave fields.

In this paper, we present an analytical approach to model frequency-dependent seismic radiation and amplitude decays with distance in comparison to robust long-term observed decay curves, measured at a WF in Uettingen (Bavaria, Germany). In a first step, we derive distance-dependent noise spectra from recordings of up to 6 months in duration and characterize the relation between signal frequency and amplitude decay. We face the challenge of handling phase differences between multiple source signals that have strong effects on the seismic radiation due to significant changes in interference pattern of the superimposed wave fields. We apply the phase shift elimination method (PSE method) to generate representative source signals as an input for the analytical modeling of the observed amplitude decays. The comparison between modeled and observed amplitude decays also allows the constraining of the parameters of a simple two-layer model of the subsurface. We further show how it is possible to generalize the approach to predict radiation patterns for arbitrary WF geometries.

2 Observational data

Our surveys were conducted in the neighborhood of a WF in Uettingen, about 9 km west of Würzburg in Bavaria. The WF consists of three WTs positioned in a NW–SE line with a spacing of 350 m and 450 m, respectively. The Nordex N117 type WTs have 2400 kW rated power and a tower height of 141 m. Their maximum rotation rate is about 12 rpm (rotations per minute). To measure the amplitude decay of the seismic WT signals we deployed 19 seismic stations along a profile of 8.3 km length, starting at the easternmost of the three WTs and running in NE direction approximately perpendicular to the geometrical layout of the WF (Fig. 1). Additionally, we placed three stations in the WT basements in order to record the seismic source signal of each WT. The instruments were installed between July and November 2019, and data recording will extend until August 2021. All stations are equipped with Trillium Compact posthole sensors (20 s) and Centaur data loggers (Nanometrics) recording continuously at a sampling frequency of 200 Hz. To improve the signal and noise conditions the sensors of the profile stations were placed in shallow boreholes of 1–2 m depth.

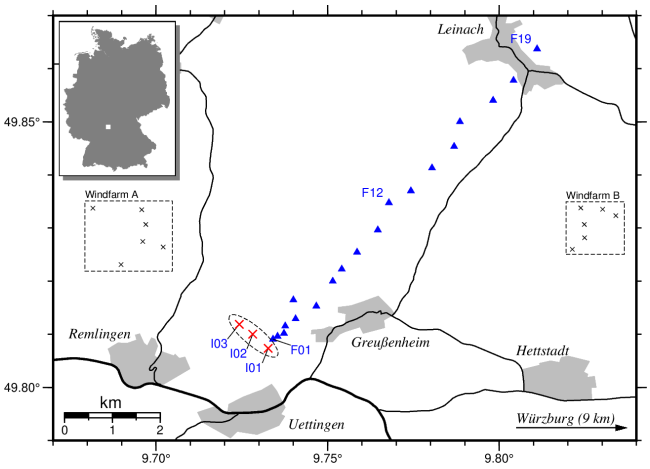

Figure 1. Location of the wind farm in Uettingen (red crosses) and seismic profile stations F01 to F19 (blue triangles). Three additional seismic stations are positioned in the WT cellars (I01, I02, I03). Wind farms A and B (dashed boxes) are not targeted by our experiment but are located in the area.

The local near-surface geology is defined by Triassic sedimentary rocks. Beneath a thin soil layer, limestones of the Muschelkalk are situated over clastic sediments of the Buntsandstein, mainly terrestrial quartzite, sandstone, and claystone layers. Geologic cross sections suggest that the lower Muschelkalk under the topographic surface reaches a thickness of up to several tens of meters (Bayerisches Geologisches Landesamt, 1978). However, at some seismic stations the Muschelkalk–Buntsandstein boundary is only a few meters below the surface. In topographic depressions the Muschelkalk can be completely missing, i.e., thin quaternary soft sediments directly cover Upper Buntsandstein rocks.

2.1 Calculation of average power spectral densities (PSDs)

We analyzed a continuous dataset between September 2019 and March 2020, covering a range of 159 to 207 d depending on the exact station installation date. We associate the measured amplitudes in the seismic waveform data with the corresponding WT parameter (in this case "rotor speed") at a resolution of 10 min. For this reason, the recordings of each profile station were split into 10 min segments that were transformed to power spectral density spectra using the method of Welch (1967). Each of these spectra were

then sorted according to the respective rotor speed into bins of 1 rpm width. With this procedure we generated close to 10 000 single PSDs within the bin of maximal rotor speed (11–12 rpm) called "full power" status for each station, and about 2000 single PSDs for the "zero power" status of the WT (0–1 rpm). In order to reliably remove outliers and reduce the impact of local transient noise (e.g., traffic on nearby roads), we excluded 75 % of the largest PSD amplitudes and used only 25 % of the single PSDs to calculate the final average PSD spectra. This seems to be a relatively strong limitation of the dataset. However, due to the long observation period there are still enough data left to calculate robust average spectra. We think that this approach provides a reliable and conservative estimate of the spectral WT amplitudes with a minimized influence of interfering transient signals. Figure S1 in the Supplement illustrates the influence of different percentiles on the calculated average PSD at station F01.

Figures 2 and 3 show the resulting average PSDs (25 % percentile) for the full power and the zero power WT status, respectively. Besides the strong microseismic peak at about 0.2 Hz, we identified nine peaks of significant energy centered at 1.14, 1.7, 2.3, 3.5, 4.8, 6.0, 7.6, 10.5, and 17.2 Hz. All of them show a systematic amplitude decrease with increasing station distance, indicating that their origin is located at the WT. For peaks 1 to 7 we fitted the observed amplitude decay with a power law model (see next section). Because of the rapid amplitude decay at frequencies > 10 Hz, we were not able to reliably fit peaks 8 and 9. For comparison we show the respective average PSDs recorded during zero power status (0–1 rpm) in Fig. 3. In this case the observed spectral peaks 1 to 9 have completely disappeared. The remaining (sharp) peaks show no systematic dependence with distance to the WF or the rotation rate of the WTs, which is an indication that their origin is not related to the WTs. High-frequency signals at > 4 Hz have a large amplitude in the near field only. Similar peak distributions have been observed by Neuffer et al. (2019) and Lerbs et al. (2020).

2.1.1 Power-law fitting of the observed amplitude decay

To quantify the PSD amplitude decay, the respective peak maxima of the full power PSDs (Fig. 2) were picked at each station. Figure 4 shows the resulting attenuation curves for peak 1 (1.14 Hz) to peak 7 (7.6 Hz) using a double-logarithmic representation, i.e., the logarithm of peak amplitude is shown versus the logarithm of the station distance. If the PSD amplitude decay corresponds to a power law, which is the basic assumption, there should be a linear correlation between log(amplitude) and log(distance). The attenuation factor, b, can then be calculated as the slope of a linear fit of the attenuation curves. As Fig. 4 shows, the measured PSD amplitude decays can be described in good approximation with a power law between station F02 and F12, which corresponds to a distance range of 300 to 4000 m. Beyond F12, the measured PSD amplitudes increase with larger distances, except for peak 1 (1.14 Hz), and it was not possible to identify clear peak maxima, since the background noise dominates the spectra. Towards the end of the seismic profile the stations get closer to a high-speed railway track and populated areas with raised ambient noise conditions, which might explain the observed excessive PSD amplitudes in this region. However, the first two stations of the profile – F01 (194 m) and F01a (239 m) – also show deviations from a power law attenuation. Due to the proximity of these stations to the WT, the amplitudes may also be affected by near-field effects.

Table 1. Calculated b values for the PSD amplitude decay, b_{PSD}, and corresponding b values of the signal amplitude decay, b_{AMP}. The latter was derived from b_{PSD} by the application of factor 0.5.

f (Hz)	b_{PSD}	b_{AMP}
1.14	0.39	0.20
1.7	0.73	0.37
2.3	0.76	0.38
3.5	1.57	0.79
4.8	2.40	1.20
6.0	3.39	1.70
7.6	3.93	1.97

For these reasons we decided to restrict the analysis of the amplitude decay to the distance range between 300 and 4000 m and to estimate the attenuation factor, b, using a linear least-squares fit between station F02 and F12 for all seven peak frequencies. The results show a systematic increase with frequency and yield values from $b = 0.39$ at 1.14 Hz up to $b = 3.93$ at 7.6 Hz. In Fig. 5 we show the frequency dependence of the attenuation factor b. It exhibits a nearly perfect linear relationship between b and frequency, at least within the analyzed frequency range from 1.14 to 7.6 Hz. The comparison to results from other authors is discussed below (Sect. 5).

The b values quantify the decay of PSD peaks in the vicinity of the Uettingen wind farm. Since PSD amplitudes are proportional to the square of amplitudes in the time domain it is possible to estimate the corresponding b values for time signals by applying a factor of 0.5. Table 1 lists both types of attenuation factors: b_{PSD} for the PSD decay, and b_{AMP} for the corresponding time amplitude decay. This should enable a better classification of our results.

2.2 Observation of phase shifts between multiple WT vibrations

Each WT can be considered a seismic source. By analyzing the seismograms measured simultaneously in the three WTs (I01, I02, and I03) of the WF Uettingen, we observe phase shifts between the individual wave forms (Fig. 6a). As an example, three time series (vertical component), each recorded in one of the WT cellars during a rotation rate of about 11.5 rpm, are filtered to a narrow bandwidth around

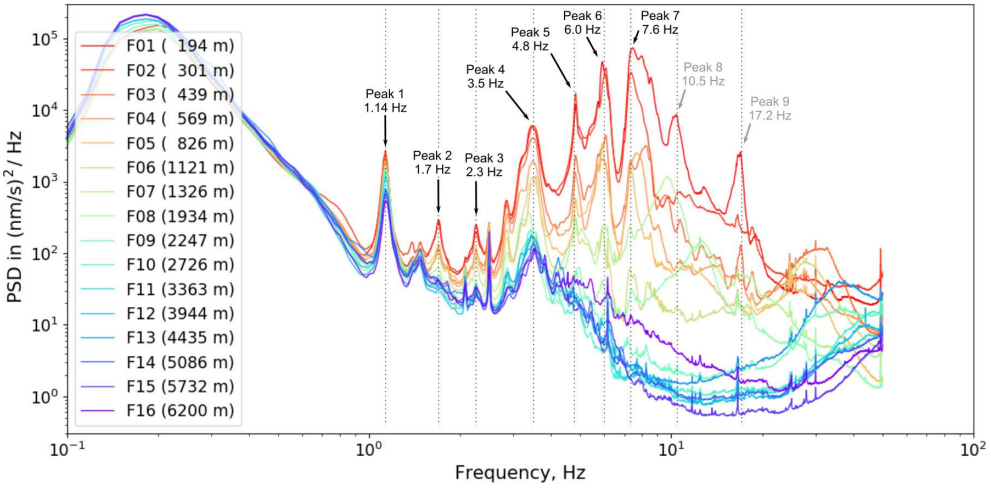

Figure 2. Average PSD spectra at full power status (11–12 rpm), calculated at profile stations F01 to F16 in the time range from September 2019 to March 2020. The distance of each station to the WT is color coded and indicated in the figure legend. In total, nine energy peaks are identified between 1.14 and 17.2 Hz, all of which show a systematic amplitude decrease with increasing station distance. The amplitude decays of peaks 1 to 7 have been measured and fitted by a power law.

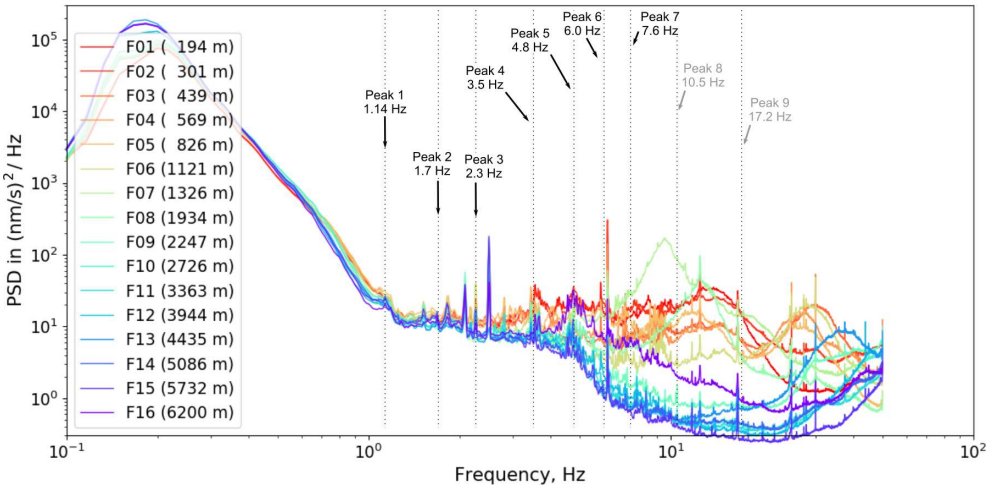

Figure 3. Average PSD spectra at zero power status (0–1 rpm), calculated at profile stations F01 to F16 in the time range from September 2019 to March 2020. The identified peaks at full power (Fig. 2) have disappeared. The remaining sharp peaks show no systematic decrease with increasing distance, indicating that they have a different origin.

frequency peak 1 with 1.14 Hz (1.10–1.18 Hz) and are compared within a time window of 22 s. In the first 2 s, the signal phase of seismic station I03 is shifted by π compared to signal I01 and I02, which are in phase. Between 10 and 13 s, all signals are almost in phase, which consequently means that the WTs are vertically vibrating in phase. After 15 s, all three signals are shifted to each other and are not in phase anymore. For a longer time period of 1 h, the phase shifts between signals measured at I01 and I02 are determined using a cross-correlation analysis with a moving time window of 5 s (= 720 time segments) along the 1 h time segment. The temporal shift is converted to the corresponding phase shift between $-\pi$ and π for each window. The distribution of all 720 resulting phase shifts is almost uniform (Fig. 6b) and shows no systematic behavior with time (Fig. 6c), which leads to the conclusion that phase differences between source signals appear rather randomly, especially over longer time periods.

3 Analytical modeling approach

In the following section, we model the observed amplitude decays and set up a mathematical formulation that includes a source function, attenuation factors, geological properties, and the superposition of multiple wave fields (produced by multiple WTs). In view of the observation that the source

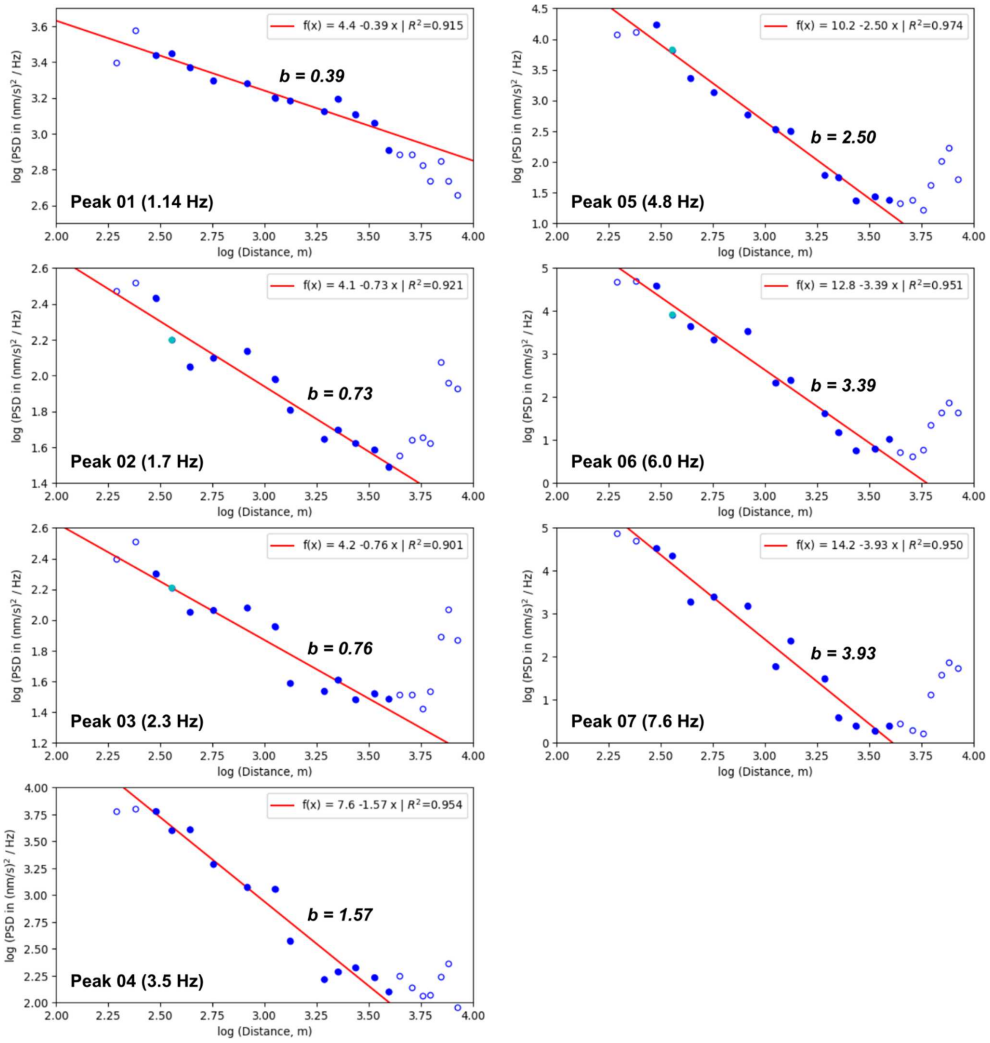

Figure 4. Double logarithmic representation of PSD amplitude decay at seven different peak frequencies. Blue circles mark the measured amplitudes from station F01 (194 m) to station F19 (8413 m) at full power status of the WT. Filled symbols denote data points that were used for power law fitting (red lines) between station F02 (301 m) and F12 (3944 m) with attenuation factor b and correlation coefficient R^2.

signals of neighboring WTs are not in phase, we study the influence of possible signal phase differences on the amplitude decay and propose a solution as to how to account for or "eliminate" this effect in the calculation.

3.1 Surface wave field approximation

Previous research suggests that mainly vertically polarized Rayleigh waves are emitted from WTs and that they dominate the WT-induced seismic noise (Westwood and Styles, 2017; Neuffer and Kremers, 2017; Gortsas et al., 2017). However, recent studies indicate that both Rayleigh and Love waves are emitted from WTs (see Lerbs et al., 2020; Neuffer et al., 2021). In our models, we assume that surface wave amplitudes decay proportionally to $r^{-1/2}$ (with distance r to the source) due to geometrical spreading of the surface wave front on a cylindrical area in the 2D surface plane

$$G = \sqrt{\frac{r_0}{r}}, \tag{1}$$

where r_0 is a reference (minimal) distance (Bugeja, 2011).

Geometrical spreading is independent of wave frequency. In addition, attenuation due to intrinsic absorption reduces the wave amplitude with distance to its source

$$D = \exp^{\frac{-wr}{2cQ}}. \tag{2}$$

The damping factor, D, depends on frequency $w = 2\pi f$, seismic wave velocity c, and again the travel distance r of the wave (Bugeja, 2011). Furthermore, D is a function of the seismic quality factor Q, which describes the loss of energy per seismic wave cycle due to anelastic processes or friction inside the rock during the wave propagation. The damping of

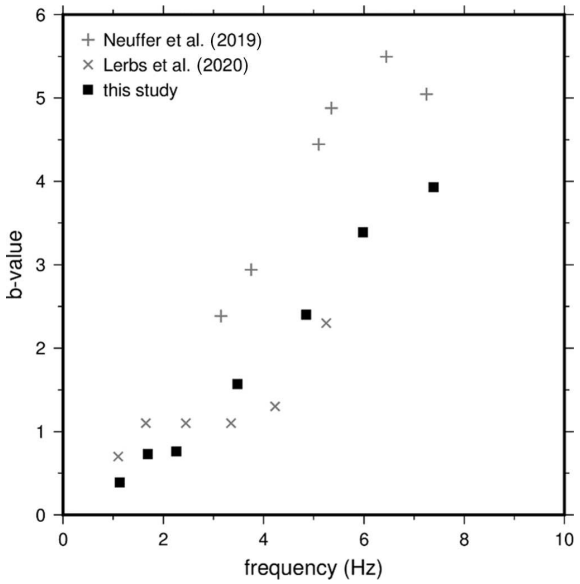

Figure 5. Frequency dependence of b values for peak 1 to peak 7 (filled symbols, cf. Fig. 4). Plus signs and crosses mark calculated b values of Neuffer et al. (2019) and Lerbs et al. (2020), respectively.

the wave is decreasing with increasing Q. The source signal $S(t)$ itself is approximated by a continuous periodic cosine-function to simulate the periodic motion at the base of the WT in vertical direction

$$S(t) = A\cos(kr - wt + \Phi), \tag{3}$$

where $S(t)$ is a function of time t, signal frequency $w = 2\pi f$, amplitude calibration factor A, wave number $k = w/c$, and signal phase Φ.

Assuming a homogeneous half-space, the wave amplitude can be calculated for any distance r to the source (Fig. 7). Considering N source points (WTs), the amplitude at each point and hence the total wave field is derived by summation over all N wave fields

$$Z(t) = \sum_{i=1}^{N}\left[S_i(t)G_i D_i\right] = \sum_{i=1}^{N}\left[A_i\cos(k_i r_i - w_i t + \Phi_i)\cdot\sqrt{\frac{r_{0,i}}{r_i}}\cdot\exp^{\frac{-w_i r_i}{2c_S Q_S}}\right], \tag{4}$$

where index i corresponds to source point i and the relative radial distance to the source points is given by $r_{0,i}/r_i$. Shear quality factor Q_S and seismic shear wave velocity c_S are model parameters and define the properties of the material the wave is traveling through. $Z(t)$ is the superposition of the individual wave fields and can be calculated at any time t.

By modeling the interference wave field as a function of time, this approach allows to derive root-mean-square amplitudes (rms amplitudes) at any point at the surface. For the calculation, the amplitude calibration factor A_i will be set to 1 for every source signal, since all three WTs of the Uettingen WF are of the same type. It should be noted that body waves (P, S) are not considered in this modeling approach, since the simulated wave field approximates a wave field dominated by Rayleigh waves. The velocity of Rayleigh waves c_R is generally slightly lower than the shear wave velocity c_S, whereas the c_R/c_S ratio depends on the Poisson ratio ν (e.g., Rahman and Michelitsch, 2006). Assuming theoretical values of ν from 0.0 to 0.5, the ratio c_R/c_S can reach values between 0.87 and 0.95 (Leiber, 2003; Hayashi, 2008), which means that the Rayleigh wave velocity is maximally about 13 % lower than the shear wave velocity. However, it is possible to approximate surface wave fields using the shear wave velocity (Kumagai et al., 2020). The penetration depth of Rayleigh waves, which is influenced by the physical properties of near-surface geological layers and the wavelength, plays an important role in approaching the modeling of WT-induced seismic wave propagation. The correct quantification of the penetration depth of Rayleigh waves is widely studied; however, so far there is no general consensus on their penetration depth in relation to the seismic wavelength λ. Based on results of Hayashi (2008), Kumagai et al. (2020) claim that surface wave velocity reflects the average S-wave velocity of the geological layers down to a depth between $\frac{1}{4}\lambda$ and $\frac{1}{2}\lambda$, whereas $\frac{1}{3}\lambda$ is often chosen to be the most suitable assumption (e.g., Larose, 2005). Moreover, it is common to derive depth information from observed wave attenuation applying modeling or tomography methods to seismological data (e.g., Siena et al., 2014). Due to Rayleigh wave dispersion, it is known that low-frequency surface waves reach deeper into the subsurface and thus will travel through materials with likely higher Q and seismic velocities c. Consequently, the damping is reduced compared to high-frequency surface waves (Karatzetzou et al., 2014; Farrugia et al., 2015). Taking this into account, we use the following relation for wavelength depth conversion

$$d_{\lambda/3} = \frac{1}{3}\lambda\left(\lambda = \frac{c_S}{f}\right). \tag{5}$$

In this study, we take advantage of the link between frequency-dependent amplitude decays (depending on Q_S and c_S, Eq. 4) and surface wave penetration depth to derive information about shear wave velocities and quality factors in the subsurface (Eq. 5).

3.2 Effect of source-signal phase on seismic radiation and amplitude decay

Since we observe significant changes of the phase shifts between signals measured at the three WTs (Sect. 2.3), we aim to study its effect on the wave field that is emitted by the three WTs in Uettingen. Hence, three wave fields are calculated using three different source phase compositions assuming a 1.14 Hz source signal frequency, 1500 m s^{-1} wave velocity and equality factor of 30 as an exemplary model. Source points are located at $x_1 = x_2 = x_3 = 0$ m and $y_1 = 350$ m,

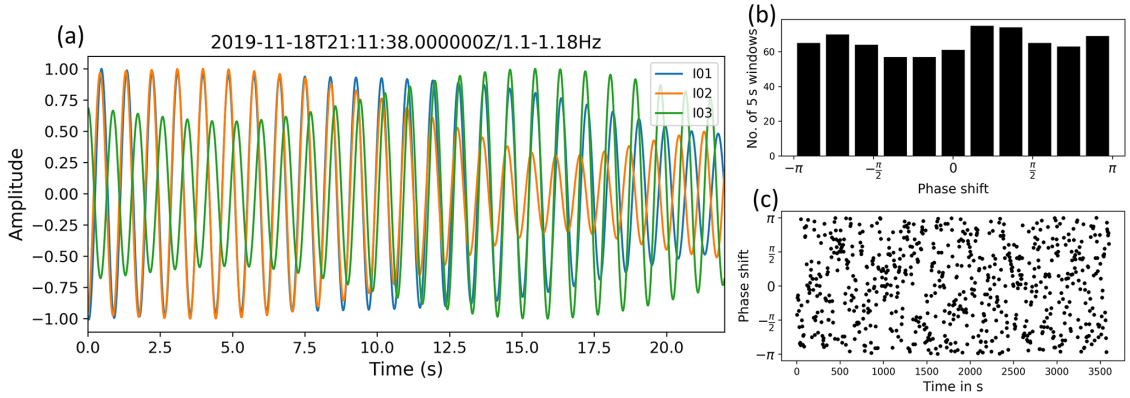

Figure 6. (a) Comparison of seismograms (vertical components) measured simultaneously in each of the three WTs at a rotation rate of 11–12 rpm. Waveforms are filtered to 1.10–1.18Hz, and amplitudes are normalized to their maximum. **(b)** Distribution of phase shift between signals in 5 s time segments measured in two WTs (I01 and I02) during a period of 1 h with WT rotation rates of 11–12 rpm. **(c)** Temporal development of the phase shift between the signals measured in the two WTs (I01 and I02).

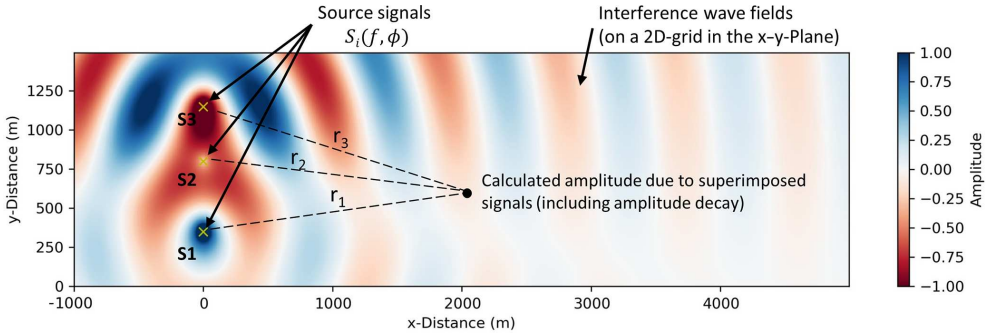

Figure 7. Schematic figure of the analytical modeling approach. Amplitudes as functions of time are calculated at points (x, y).

$y_2 = 800$ m, and $y_3 = 1150$ m (Fig. 7). Amplitudes are calculated along a profile extending from source signal S1 (see Fig. 7) and perpendicular to the WF line, which approximates the real geometry of the WF and seismic profile in Uettingen. The results show a clear dependence of the amplitude decays on the source signal phase composition (Fig. 8). In addition, amplitudes at the end of the 5000 m long profile differ significantly from each other. In the third scenario (Fig. 8c), the expected amplitude is a quarter of the amplitude that is reached if the WTs are vibrating in phase (Fig. 8a). Furthermore, strong effects appear in the first 2 km of the profile. Scenario (a) shows increased amplitudes due to constructive wave interference in the near field, whereas scenario (c) indicates a rapid decay of amplitudes within the first 1000 m of the profile. Scenario (b) shows a smoother and steadier decay of the amplitudes and reaches an amplitude at the end of the profile that is reduced by a fifth compared to scenario (a). These exemplary scenarios demonstrate only three out of infinite possibilities of different source signal phase compositions. Taking this into account, the seismic radiation of a WF is affected by phase differences of the source signals which can lead to strong changes in the wave field interference.

3.3 Phase shift elimination and data fitting

In this section we propose a method of how to handle the observed time-varying source signal phases and their effect on the seismic radiation using the assumption of a random appearance of signal phase constellation of multiple WTs, especially regarding long time periods. To define representative source signals, we developed a phase shift elimination method (PSE method). Within this PSE method, 500 radiation patterns (i.e., wave fields) are calculated using random signal phases Φ (between 0 and π) for each individual source signal. All 500 calculated wave fields are then averaged, and the average amplitude decay is extracted along the profile, which in turn is independent of the individual source signal phases. We experienced that the wave field averaging process and hence final amplitude decay calculation is sufficiently stable after 500 wave field simulations, whereas a number of < 100 seems too low to generate a reproducible result. We apply this method to the Uettingen WF setup and compare the modeling results with the observed amplitude decays in Uettingen during rotation rates between 11 and 12 rpm (all WTs under full power). Since the observed PSD

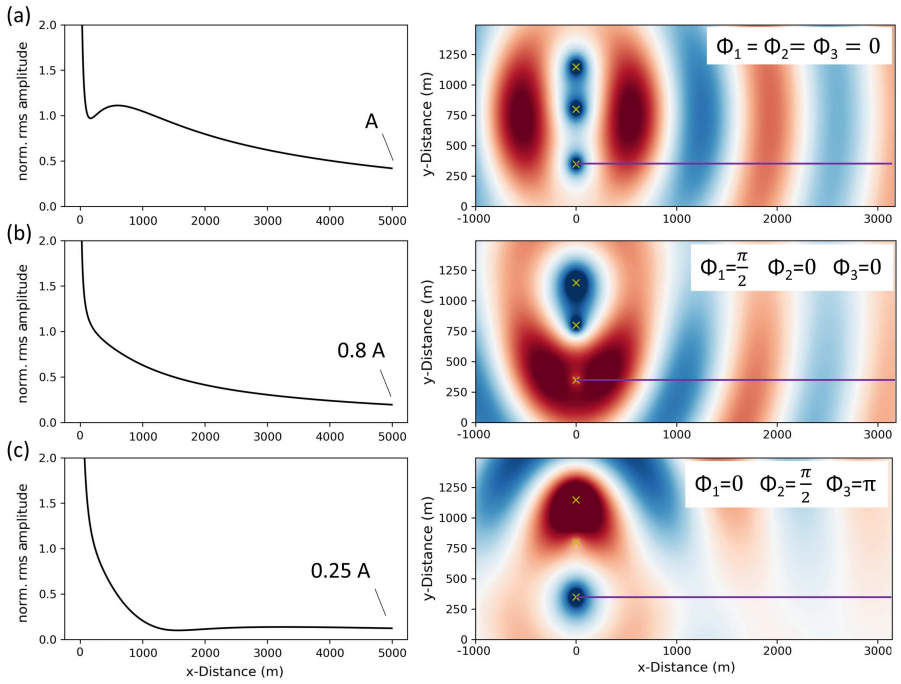

Figure 8. Calculated amplitude decay curves (in the direction of the magenta line) for three scenarios with different source signal phase compositions using **(a)** $\Phi_1 = \Phi_2 = \Phi_3 = 0$ (vibration in phase), **(b)** $\Phi_1 = \pi/2$, $\Phi_2 = 0$, $\Phi_3 = 0$, and **(c)** $\Phi_1 = 0$, $\Phi_2 = \pi/2$, $\Phi_3 = \pi$. Index 1 represents the source point S1. All decay curves are normalized to the amplitude at $x = 300$ m.

amplitudes are proportional to squared ground motion amplitudes in the time domain (rms amplitudes), we compare our modeling results (rms amplitudes) with the square root of the observed PSD amplitudes. The analysis is performed for signals with center frequencies of 1.14, 1.69, 2.26, 3.5, 4.85, 5.98, and 7.6 Hz, representing the 7 PSD peaks in Uettingen (see Sect. 2.1). For comparison, all decay curves are normalized to the amplitude measured in 300 m distance (seismic station F02), to be consistent with the attenuation analysis presented in Sect. 2.2. The calculated radiation pattern covers an area of 6000 m in length (x) and 1500 m in width (y) with a grid space of 10 m.

Calculated and observed data are fitted by a Q_S–c_S grid search to find the best model parameters. The data is grouped into signals with low frequencies < 4 Hz (1.14, 1.69, 2.26, and 3.5 Hz) and high frequencies > 4 Hz (4.85, 5.98, and 7.6 Hz) to distinguish between shallow and deep geological effects on the amplitude decay due to the frequency-dependent penetrating depth of surface waves. All amplitude decays per group are fitted with one Q_S–c_S model. To set up the grid search, model parameter c_S are varied from 400 to 3000 m s^{-1} using steps of 20 m s^{-1}, and the parameter Q_S is varied between 6 to 250 using a step size of 2. An averaged (500 decay curves) amplitude decay with distance is calculated for each combination of Q_S and c_S and is compared to the observed data by calculating the root-mean-square error (RMSE):

$$\mathrm{RMSE} = \sqrt{\frac{\sum_{i=1}^{M} (\mathrm{obs}_i - \mathrm{sim}_i)^2}{M}}, \tag{6}$$

where M represents the 14 seismic stations along the profile that are included in the fitting process. This process is performed for 16 114 different models per frequency (Fig. 9).

Moreover, the normalized root-mean-square error (NRMSE) is obtained to quantify the fitting quality. To determine the NRMSE, each RMSE is divided by the range (maximum value − minimum value) of the observation amplitudes for each frequency in order to scale the comparison between the datasets. The total NRMSE is then given by the mean of all normalized RMSE:

$$\mathrm{NRMSE} = \frac{\mathrm{RMSE}}{\mathrm{obs}_{\max} - \mathrm{obs}_{\min}}. \tag{7}$$

4 Results

To fit modeled and observed amplitudes we performed a separate grid-search for both the group with high-frequency signals and with low-frequency signals. During each individual fitting process, the PSE method was applied to ensure results that are independent of source signals phases. Regarding the group of low-frequency signals (< 4 Hz), we obtain $Q_S = 40$ and $c_S = 960$ m s^{-1} (Table 2) as the best model parameters. The values of the 20 best models range between

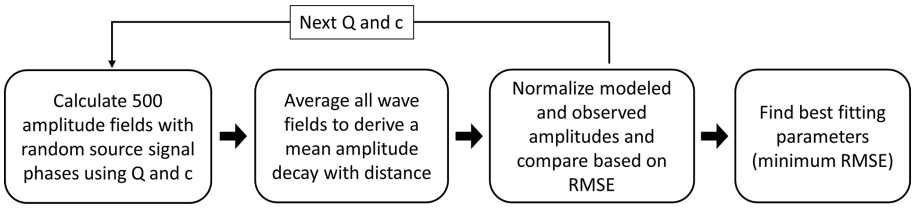

Figure 9. Description of the fitting process to find the best model parameters from the comparison of calculated and observed amplitudes.

36 and 60 for Q_S and 920 m s^{-1} and 1040 m s^{-1} for c_S. Regarding the group of high-frequency signals (>4 Hz), we obtain $Q_S = 16$ and $c_S = 540$ m s^{-1} as the best parameters. Results of the 20 best models range between 12 and 32 for Q_S and between 540 and 660 m s^{-1} for c_S (Fig. 10). By fitting two frequency groups, we can derive a two-layer model (one layer with a half-space below), after converting the frequency-dependent wavelength to the corresponding penetration depth (Eq. 5). Thus, we expect a shear wave velocity of 540 m s^{-1} down to 37 m depth and 960 m s^{-1} until 280 m depth (Fig. 11). However, transition between the two layers (37 m to 91 m) is not clearly defined due to missing information for frequencies between 3.5 and 4.85 Hz. Furthermore, we can only gain information about the attenuation of signals down to a frequency of 1.14 Hz. Hence, we are limited concerning the conversion of wavelength to depth information, and we can only derive values (c_S and Q_S) to a estimated depth of about 280 m. We cannot give information about the properties of deeper layers. The velocity error is approximated by the range of the 20 best models (Fig. 10). During the fitting process, we noticed that it was not possible to fit all seven amplitude decays with only one c_S–Q_S model successfully, especially regarding signals with frequencies >4 Hz. A homogeneous model is consequently not reasonable in this case. However, the corresponding results are given in the Supplement (Fig. S2). Modeled and observed data are generally in very good agreement for each of the seven analyzed frequencies (Figs. 12 and 13). The very slow decrease of observed amplitudes, especially at 1.14 Hz (Fig. 12a), and the relatively strong decrease of signals with 7.6 Hz (Fig. 13c) are simulated correctly and confirm a higher attenuation with higher frequencies, as expected. For a frequency of 1.14 Hz, between $x = 2000$ and 4000 m, modeled amplitudes are underestimated in comparison to the observations. Minor deviations between modeled and observed data for frequencies >4 Hz might be explained by local effects that are not represented in our laterally homogeneous models. Interestingly, a local increase of amplitude with distance is observable in the real data, especially for the 3.5 and 4.85 Hz signals, as well as in the simulated data (Figs. 12d and 13a). This undulation is likely caused by superimposed wave fields of multiple WTs, as indicated by the modeled radiation pattern. Moreover, the sensitivity concerning the source signal phase compositions decreases clearly with increasing frequency, which indicates

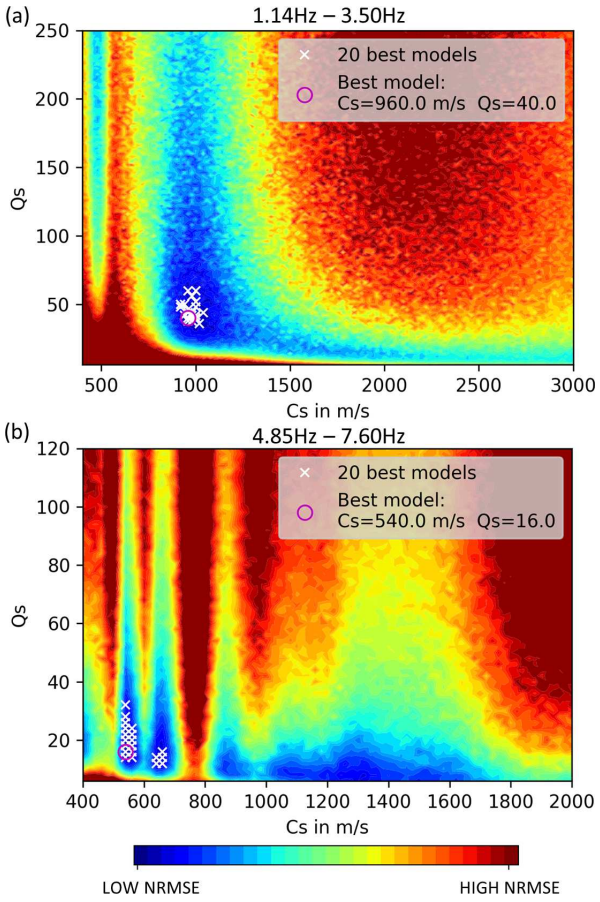

Figure 10. Distribution of the NRMSE of the fit between modeled and observed amplitude decays obtained by a Q_S–c_S grid search. The 20 best models (white cross) and the very best model (magenta circle) that fit amplitude decays of signals with **(a)** 1.14, 1.69, 2.26, and 3.50 Hz and **(b)** 4.85, 5.98 and 7.60 Hz.

that effects of phase differences between source signals are more significant for lower frequencies. The radiation patterns off the profile are quite symmetrical since the WTs are positioned in a clear geometry (in a line with similar distances between the WTs). This might not be given if the WTs are arranged in more complex layouts that could lead to locally increased or decreased amplitudes due to wave field interferences.

Table 2. Best model parameters (c_S and Q_S) to fit observed and calculated amplitude decays of low- and high-frequency signals. Depth d is estimated by assuming a surface wave penetration depth of $\lambda/3$.

	f in Hz	$c_{S,mean}$ in m s^{-1}	Q_S	$d_{\lambda/3}$ in m
Low-frequency group	1.14, 1.69, 2.26, 3.5	960	40	91–280
High-frequency group	4.85, 5.98, 7.6	540	16	0–37

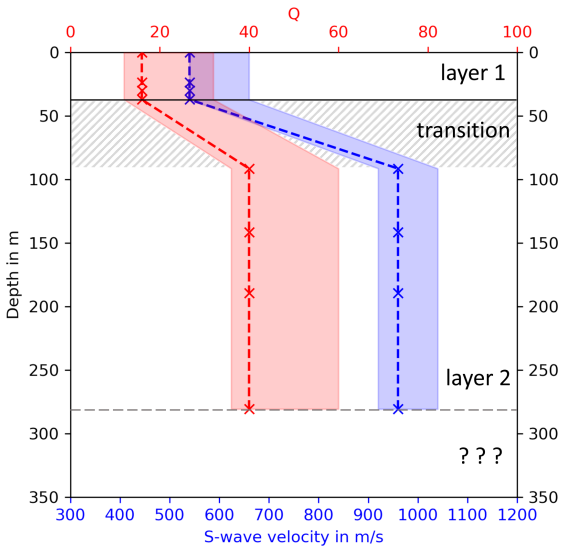

Figure 11. Two-layer model derived by fitting observed and modeled amplitude decays. The best model parameters (c_S and Q_S) for the two layers are found by performing a grid search to optimize the fitting of amplitude decays of signals < 4 and > 4 Hz separately. The depths of the layer interfaces are obtained by assuming a penetration depth of surface waves of $\lambda/3$. The transition between layer 1 and layer 2 and the area below layer 2 is unclear, due to the lack of amplitude decays of signals between 3.5 and 4.85 Hz and below 1.14 Hz.

5 Discussion

The aim of this study is to present reliable amplitude decays of seismological signals produced by multiple WTs and to model these amplitude decays with an analytical approach. The propagation of WT-induced seismic signals has been the subject of numerous studies. Many authors found that the amplitude decay with increasing distance (r) between WT and observation point can be described by a power law of the form $1/r^b$. In general, the absorption factor, b, increases with increasing frequency. Results found in our study show a near-perfect linear increase of the b value with frequency and range from $b = 0.39$ at 1.14 Hz up to $b = 3.93$ at 7.6 Hz. By converting the b values from the spectral domain (PSD) into the time domain (Table 1), we find b values < 0.5 at frequencies ≤ 2.3 Hz, which is lower than the theoretical value for geometrical spreading of a single source surface wave. An explanation for this is the interference of the three wave fields from the three WTs. Although the decay of signals from a single WT would likely not be lower than the geometrical spreading attenuation, we can show that the superposition of wave fields could significantly increase the amplitudes along the profile. The b factors derived by the various authors cover a broad range of values, even for similar frequency ranges. Flores Estrella et al. (2017) published b values from 0.73 to 1.87 for frequencies between 2.7 and 4.5 Hz. Zieger and Ritter (2018) derived values from 0.78 to 0.85 at 1–4 Hz and $b = 1.59$ at 5.5 Hz. The results from Lerbs et al. (2020) range between 0.7 and 1.3 at 1–4 Hz and $b = 2.3$ at 5 Hz. Neuffer et al. (2019) derive b values of 2.4 at 3 Hz and values of $b > 5$ at frequencies of 6–7 Hz. In Fig. 5, we compare our results with the b values of Neuffer et al. (2019) and Lerbs et al. (2020). These studies yield a similar frequency dependence. However, the results of Neuffer et al. (2019) show systematically higher b values. This observation could be due to different geological conditions with stronger attenuation effects during wave propagation. Furthermore, Neuffer et al. (2019) used so-called "differential" PSD spectra to measure the peak amplitude decay. These amplitudes are calculated from the difference between the PSD peaks at full power and the PSD peaks at zero power, which could lead to an overestimation of the amplitude decay. Lerbs et al. (2020) get similar b values; however, compared to our results the scatter is significantly larger. Most authors explain the observed b-value scattering using different local geological conditions that influence the attenuation of the emitted seismic WT signals. It should be noted, however, that some of the above-mentioned studies use relatively short time windows to estimate the spectral amplitudes at increasing distances. Flores Estrella et al. (2017) analyze time series of 2 h lengths, and Lerbs et al. (2020) use 6 h. In this case the measured amplitudes could be affected by transient signals such as earthquakes or local anthropogenic noise sources, which may result in uncertain b-value estimates. In contrast, Neuffer et al. (2019) extend the analysis to 6.5 weeks. Since the knowledge of the amplitude decay plays a fundamental role in the modeling of the WT signals, we decided to use significantly longer time windows (6 months) in order to derive robust average PSD spectra at the installed profile stations.

In terms of modeling approaches, most of the recent publications focus on modeling the seismic signals that are emitted by one single WT (e.g., Gortsas et al., 2017) or the whole WF is considered as one emitting source. Since we observe time-varying phase differences between the signals that are

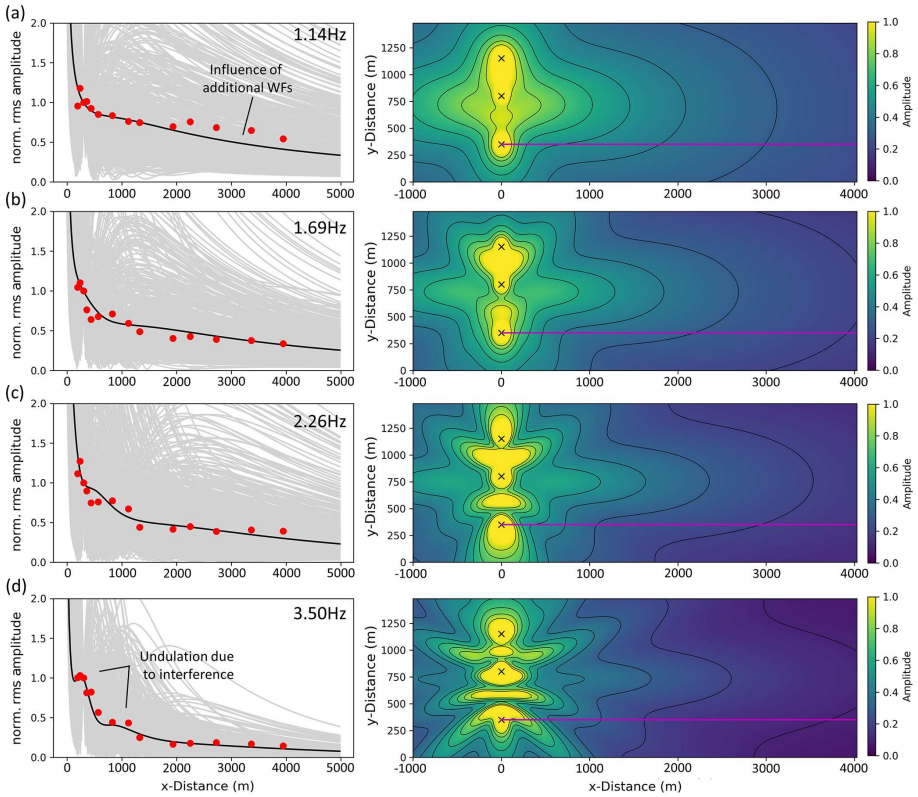

Figure 12. Averaged modeled radiation patterns (right) and averaged amplitude decays (left, black line) along the profile (magenta line) by averaging 500 wave fields and decay curves (gray lines), based on random ϕ (between $0, \pi$) to eliminate the effect of phase differences between source signals. Red dots represent the observed amplitudes in Uettingen at **(a)** 1.14 Hz, **(b)** 1.69 Hz, **(c)** 2.26 Hz, and **(d)** 3.50 Hz.

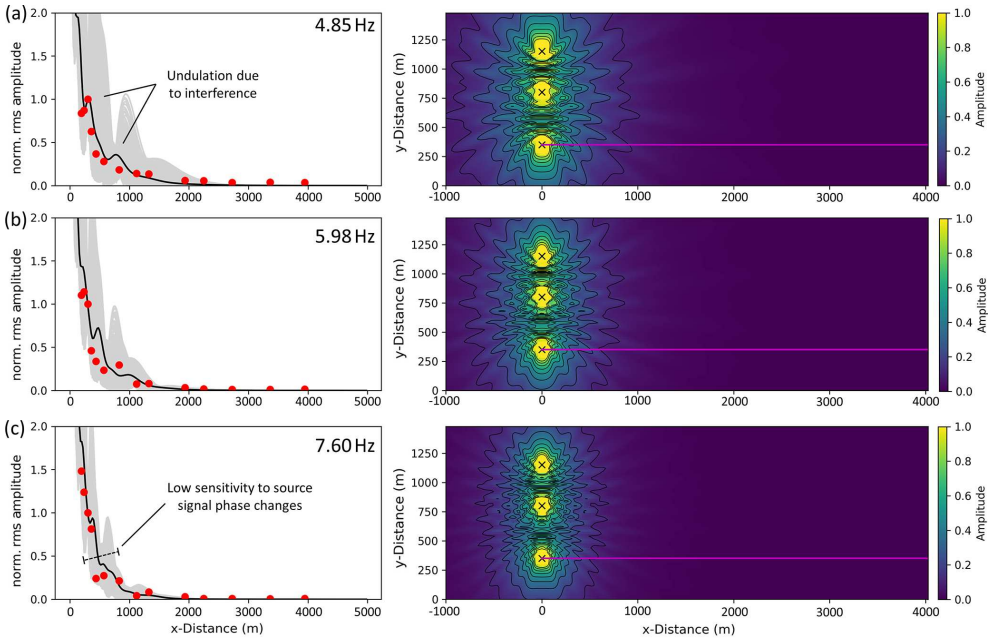

Figure 13. Averaged modeled radiation patterns (right) and averaged amplitude decays (left, black line) along the profile (magenta line) found by averaging 500 wave fields and decay curves (gray lines) based on random ϕ (between $0, \pi$) to eliminate the effect of phase differences between source signals. Red dots represent the observed amplitudes in Uettingen at **(a)** 4.85 Hz, **(b)** 5.98 Hz, and **(c)** 7.60 Hz.

measured directly at the three individual WTs of the WF Uettingen, we propose that this effect must be included in the modeling of WFs. Our observations confirm the significance of phase differences between the seismic signals from the WTs of a wind farm and that the signal phase of a single WT is not stable over time. Hence, we expect that phase differences between source signals vary randomly, which was already presumed by Saccorotti et al. (2011). Superimposed wave fields lead to constructive and destructive interferences (which depend on, e.g., signal phases) and affect the spatial amplitude decay, as we can show in this study (Fig. 8). Similar to our approach, Saccorotti et al. (2011) modeled amplitude decays on the basis of superimposed wave fields and attenuation laws but did not include phase shift variations between signals of the WTs. However, they noticed that the increase of noise depends on WT number, which was later shown by Neuffer et al. (2019). Saccorotti et al. (2011) suggest that more accurate results can be derived by considering WTs that are not vibrating in phase. Here, we can prove the randomness of these phase differences between WTs and propose a solution by applying the PSE method to the modeling. Only with this consideration we can reproduce the observed amplitude decay. The PSE-method (averaging 500 wave fields calculated with random signal phases) is generally difficult to apply if full wave form propagation simulation is needed (e.g., FEM, finite element methods), since the required computation time would increase rapidly. Within our modeling approach, the source amplitude is chosen to be uniform for the three WTs. Previous studies (e.g., Lerbs et al., 2020) showed that WTs emit signals with time-varying amplitude and azimuths. In terms of modeling radiation patterns for very short time periods, this should be considered when choosing representative source characteristics. To model radiation patterns that represent long time periods (quasi-static processes), a uniform source amplitude should be sufficient, provided that the WTs are of the same type.

For the Uettingen WF the discrepancy between observed and simulated amplitude decays for 1.14 Hz in distances larger than 2000 m to the WTs are likely due to the other nearby WFs A and B (Fig. 1). We assume that the low-frequency signals of these WFs travel farther compared to higher-frequency signals and are measured in addition to the signals from the targeted three WTs in Uettingen (Fig. 1). This could lead to an overestimation of the signal amplitudes, especially in the far field of the WF Uettingen. However, since we observe peaks at identical frequencies in the near and far field of the WF, it is reasonable to assign these signals mainly to the wave field produced by the WTs in Uettingen. Signals from various WFs can generally be distinguished using, e.g., a migration approach (Friedrich et al., 2018). However, detailed analysis of the effect of additional WFs around Uettingen is beyond the scope of this study, but their impact should be considered in future analysis. Interestingly, the sensitivity to source signal phases (gray lines in Figs. 12 and 13) is significantly higher for 1.14 Hz signals than 7.6 Hz and is generally decreasing with increasing frequency. This indicates that the signal phases are not as important for higher frequencies than for lower frequencies (e.g., 1.14 Hz). It should be noted that some of the individual input source signal phase compositions led to decay curves that could not fit the observation data at all. This is solved using the PSE method.

Lerbs et al. (2020) proposed a solution that describes the wave attenuation with distance using an attenuation model solely based on a power law assumption (b values). This approach does not allow a more universal application to other WFs or regions since b values are not directly assigned to geological properties. The approach used in our study includes the intrinsic attenuation factor, which depends on two geological parameters, the seismic wave velocity and quality factor. We find frequency-dependent Q values of 16 and 40 and c_S of 540 and 960 m s^{-1}. The local geology is dominated by sedimentary rocks of the Buntsandstein, which could explain the relatively low Q values (high damping). The attenuation is very likely dominated by intrinsic attenuation and not scattering, since the topography around Uettingen is relatively smooth and large damaging zones or faults are missing. A homogeneous half-space is therefore the basic assumption within our model. However, we show that the effect of layered media in the underground should be considered assuming frequency-dependent velocity and quality factors, due to significant dispersion effects of surface waves. It is generally an advantage to include geological properties in the model: (1) to consider actual physical properties of the medium the waves are traveling through and (2) to enable the possibilities of studying the effect of various geological conditions on the seismic radiation and amplitude decays.

To demonstrate the capability and possible application of the modeling approach used in this study, we modeled the radiation pattern of the original WF in Uettingen for 1.14 and 7.6 Hz signals and compared the results with the case where three imaginary WTs are arbitrarily added to the existing WF (Fig. 14). Model parameters are $c_S = 960$ m s^{-1} and $Q_S = 40$ for 1.14 Hz and $c_S = 540$ m s^{-1} and $Q_S = 16$ for 7.6 Hz. The pattern of the radiation for 1.14 Hz signals is clearly affected by adding three WTs to the WF in Uettingen, whereby amplitudes are significantly increased, even in remote areas, for example in the NNW of the WF (Fig. 14a and c). The effect on the characteristic radiation of 7.6 Hz signals is negligible since the signal amplitude is damped rapidly in both cases, i.e., modeling three WTs or six WTs (Fig. 14b and d). As the demonstration shows, the modeling approach allows the estimation of the characteristic seismic radiation pattern of an arbitrary WF in order to identify locations of low or high noise amplitudes or to evaluate WF geometry effects. Furthermore, the source locations, source signal frequencies and amplitudes, and the expected local underground are free for researchers to choose (with limitations regarding their complexity), which enables an approximation

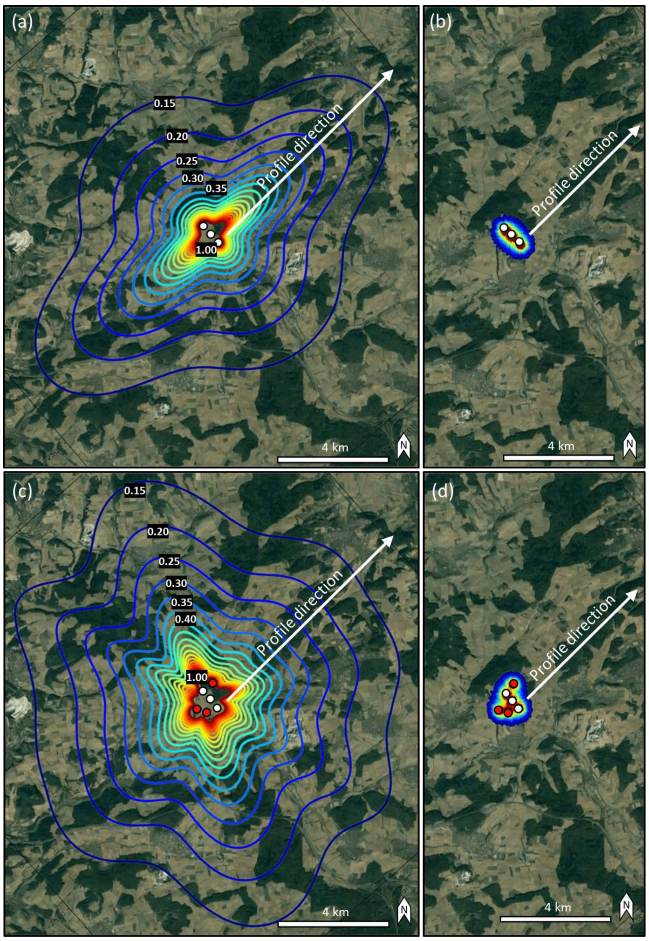

Figure 14. Estimated seismic radiation pattern (red showing high amplitudes) of **(a)** the Uettingen wind farm (white dots) for 1.14 Hz and **(b)** 7.6 Hz. Three arbitrary WTs (red dots) are added to the existing WF and affect the radiation for **(c)** 1.14 Hz and **(d)** 7.6 Hz. Model parameters are $c_S = 960\,m\,s^{-1}$ and $Q_S = 40$ in **(a, c)**, whereas they are $c_S = 540\,m\,s^{-1}$ and $Q_S = 16$ in **(b, d)**. Calculations are based on 500 averaged wave fields using random source signal phases. Contour lines show the amplitude decay factor from 1 to 0.15 (map data: © Google Maps, 2021).

of the surface wave field emitted by WFs with various layouts.

6 Conclusions

We recorded the seismic signals emitted from a three-turbine WF in Uettingen, Bavaria, over a period of 6 months and analyzed the spectral characteristics and spatial amplitude decays. During the full power operation mode of the WTs we identify seven prominent spectral peaks in the frequency range from 1.14 to 7.6 Hz. The attenuation of the peak amplitudes with respect to the WT distances can be described by a power law with exponent b. We find that the calculated b values increase linearly with increasing peak frequency and range between 0.39 and 3.93. Due to the relatively long observation period, the calculated values provide a stable basis for the analytical simulation of the emitted wave field.

An analytical approach was developed to model the seismic radiation of the WF. From measurements we observe that WTs are not vibrating in phase and that the phase differences vary randomly over time. Furthermore, the results of the simulation show a strong influence of phase differences between single WT source signals on the radiation pattern and hence on the spatial amplitude decays. We applied a phase shift elimination method (PSE method) to eliminate this effect with the aim of deriving a representative seismic wave field. Modeling results were compared to the observed frequency-dependent amplitude decays to derive model parameters (Q_S and c_S) for a two-layer model that provides information about the local geology. Concerning the modeling of WT-induced seismic signals, we can show that the signal phases of multiple source signals (multiple WTs) have significant influence on the seismic radiation of the WFs. This effect should be carefully considered when selecting suitable source signals to avoid misleading simulation results.

Code and data availability. The code and data used in this research are currently restricted.

Supplement. The supplement related to this article is available online at: https://doi.org/10.5194/se-12-1851-2021-supplement.

Author contributions. FL and ML performed the field work and data analysis. FL set up the modeling approach and performed model calculations. GR participated in data interpretation and model development and supervised the article outline. HD and GR initiated the project and provided the computational framework. FL, ML, GR, and HD edited the article.

Competing interests. The authors declare that they have no conflict of interest.

Disclaimer. Publisher's note: Copernicus Publications remains neutral with regard to jurisdictional claims in published maps and institutional affiliations.

Acknowledgements. We would like to thank ESWE Versorgungs AG for providing access to the wind farm facilities in Uettingen and their operational data, and we would especially like to thank Ulrich Schneider for his support in initiating the project. We appreciate the support of the mayors of Uettingen, Greußenheim, Remlingen, and Leinach as well as their respective municipal administrations. Special thanks are given to Wolfgang Reinhart, Joachim Palm, and Ana Costa for their help during fieldwork and station maintenance

and to Gabriele Schmidt (ESWE), who was our contact person regarding technical matters of the WF Uettingen.

Financial support. This research is part of the project KWISS and has been supported by the German Federal Ministry for Economic Affairs and Energy (FKZ no. 0324360) and ESWE Innovations und Klimaschutzfonds.

This open-access publication was funded
by the Goethe University Frankfurt.

Review statement. This paper was edited by Charlotte Krawczyk and reviewed by Joachim Ritter and Hortencia Flores Estrella.

References

Bugeja, R.: Crustal Attenuation in the region of the Maltese Islands using CodaWave Decay, PhD thesis, Department of Physics, University of Malta, 2011.

Bayerisches Geologisches Landesamt: Geologische Karte von Bayern 1 : 25.000, Blatt 6124, Remlingen, München, 1978.

Farrugia, D., Paolucci, E., D'Amico, S., Galea, P., Pace, S., Panzera, F., and Lombardo, G.: Evaluation of seismic site response in the Maltese archipelago, in: Establishment of an Integrated Italy–Malta Cross–Border System of Civil Protection, Geophysical Aspects, 79–98, Chapter: V, 2015.

Flores Estrella, H., Korn, M., and Alberts, K.: Analysis of the Influence of Wind Turbine Noise on Seismic Recordings at Two Wind Parks in Germany, Journal of Geoscience and Environment Protection, 5, 76–91, https://doi.org/10.4236/gep.2017.55006, 2017.

Friedrich, T., Zieger, T., Forbriger, T., and Ritter, J. R. R.: Locating wind farms by seismic interferometry and migration, J. Seismol., 22, 1469–1483, https://doi.org/10.1007/s10950-018-9779-0, 2018.

Gortsas, T. V., Triantafyllidis, T., Chrisopoulos, S., and Polyzos, D.: Numerical modelling of micro-seismic and infrasound noise radiated by a wind turbine, Soil Dyn. Earthq. Eng., 99, 108–123, https://doi.org/10.1016/j.soildyn.2017.05.001, 2017.

Hayashi, K.: Development of the Surface-wave Methods and Its Application to Site Investigations, PhD thesis, Kyoto University, Japan, 2008.

Karatzetzou, A., Negulescu, C., Manakou, M., François, B., Seyedi, D. M., Pitilakis, D., and Pitilakis, K.: Ambient vibration measurements on monuments in theMedieval City of Rhodes, Greece, B. Earthq. Eng., 13, 331–345, https://doi.org/10.1007/s10518-014-9649-2, 2014.

Kumagai, T., Yanagibashi, T., Tsutsumi, A., Konishi, C., and Ueno, K.: Efficient surface wave method for investigation of the seabed, Soils Found., 60, 648–667, https://doi.org/10.1016/j.sandf.2020.04.005, 2020.

Larose, E.: Lunar subsurface investigated from correlation of seismic noise, Geophys. Res. Lett., 32, L16201, https://doi.org/10.1029/2005gl023518, 2005.

Leiber, C.-O.: Assessment of safety and risk with a microscopic model of detonation, Elsevier, Amsterdam Boston, ISBN 0444513329, 2003.

Lerbs, N., Zieger, T., Ritter, J., and Korn, M.: Wind turbine induced seismic signals: the large-scale SMARTIE1 experiment and a concept to define protection radii for recording stations, Near Surf. Geophys., 18, 467–482, https://doi.org/10.1002/nsg.12109, 2020.

Neuffer, T. and Kremers, S.: How wind turbines affect the performance of seismic monitoring stations and networks, Geophys. J. Int., 211, 1319–1327, https://doi.org/10.1093/gji/ggx370, 2017.

Neuffer, T., Kremers, S., and Fritschen, R.: Characterization of seismic signals induced by the operation of wind turbines in North Rhine-Westphalia (NRW), Germany, J. Seismol., 23, 1161–1177, https://doi.org/10.1007/s10950-019-09866-7, 2019.

Neuffer, T., Kremers, S., Meckbach, P., and Mistler, M.: Characterization of the seismic wave field radiated by a wind turbine, J. Seismol., 25, 825–844, https://doi.org/10.1007/s10950-021-10003-6, 2021.

Rahman, M. and Michelitsch, T.: A note on the formula for the Rayleigh wave speed, Wave Motion, 43, 272–276, https://doi.org/10.1016/j.wavemoti.2005.10.002, 2006.

Saccorotti, G., Piccinini, D., Cauchie, L., and Fiori, I.: Seismic Noise by Wind Farms: A Case Study from the Virgo Gravitational Wave Observatory, Italy, B. Seismol. Soc. Am., 101, 568–578, https://doi.org/10.1785/0120100203, 2011.

Siena, L. D., Thomas, C., Waite, G. P., Moran, S. C., and Klemme, S.: Attenuation and scattering tomography of the deep plumbing system of Mount St. Helens, J. Geophys. Res.-Sol. Ea., 119, 8223–8238, https://doi.org/10.1002/2014jb011372, 2014.

Stammler, K. and Ceranna, L.: Influence of Wind Turbines on Seismic Records of the Gräfenberg Array, Seismol. Res. Lett., 87, 1075–1081, https://doi.org/10.1785/0220160049, 2016.

Styles, P., Stimpson, I., Toon, S., England, R., and Wright, M.: Microseismic and Infrasound Monitoring of Low Frequency Noise and Vibrations from Windfarms, PhD thesis, Keele University, UK, 2005.

Welch, P.: The use of fast Fourier transform for 335 the estimation of power spectra: A method based on time averaging over short, modified periodograms, IEEE Transactions on Audio and Electroacoustics, 15, 70–73, https://doi.org/10.1109/tau.1967.1161901, 1967.

Westwood, R. F. and Styles, P.: Assessing the seismic wavefield of a wind turbine using polarization analysis, Wind Energy, 20, 1841–1850, https://doi.org/10.1002/we.2124, 2017.

Zieger, T. and Ritter, J. R. R.: Influence of wind turbines on seismic stations in the upper rhine graben, SW Germany, J. Seismol., 22, 105–122, https://doi.org/10.1007/s10950-017-9694-9, 2018.

Zieger, T., Nagel, S., Lutzmann, P., Kaufmann, I., Ritter, J., Ummenhofer, T., Knödel, P., and Fischer, P.: Simultaneous identification of wind turbine vibrations by using seismic data, elastic modeling and laser Doppler vibrometry, Wind Energy, 23, 1145–1153, https://doi.org/10.1002/we.2479, 2020.

4. Development of a numerical modelling method to predict the seismic signals generated by wind farms

---

This chapter has been **published** in:

Limberger, F., Rümpker, G., Lindenfeld, M., and Deckert, H. (2022): Development of a numerical modelling method to predict the seismic signals generated by wind farms. Scientific Reports, 12, doi:10.21203/rs.3.rs-1621492/v1

---

scientific reports

Check for updates

OPEN

Development of a numerical modelling method to predict the seismic signals generated by wind farms

Fabian Limberger[1,2]✉, Georg Rümpker[1,3], Michael Lindenfeld[1] & Hagen Deckert[2]

In efforts to reduce greenhouse gas emissions, renewable energies have been increasingly leveraged to generate power; in particular, the number of wind turbines has risen sharply in recent years and continues to grow. However, being mechanically coupled to the earth, wind turbines also generate ground vibrations, which can have adverse effects on the capability of seismic observatories to detect and analyse earthquakes; nevertheless, the distances at which these signals modulate seismic records are disputed between the operators of wind farms and seismic observatories. Here, to quantify the noise signal amplitudes at distant seismometers, we develop the first numerical model to predict the seismic wavefield emitted by wind farms and simulate the complex effects of wavefield interferences, surface topography and attenuation. This modelling approach can reliably quantify the influences of multiple wind turbines on ground motion recordings and thus provide necessary information to aid decision-making in advance of wind farm installation.

The development and exploitation of renewable energies play a key role in slowing the warming of the global climate. Wind is a crucial source of renewable energy; consequently, increasing the number of wind turbines (WTs) to be installed in the coming decade is an important step toward a fossil-free energy supply. Nevertheless, WTs can have impacts on their environment such as audible acoustic noise, infrasound, and shadow cast. Thus, to minimize negative effects on the surrounding environment, WTs are often erected in remote areas with preferably windy conditions. Seismic stations are typically sited in similarly quiet areas to minimize the noises resulting from industries, railways, and traffic. However, research has shown that seismic stations record seismic signals produced by nearby WTs. These signals, which are considered noise, can have a significant adverse impact on the recordings of earthquakes required by various agencies to detect and analyse seismic activity. An increase in the background seismic noise at a seismic station decreases its ability to detect seismic waves emitted by earthquakes, especially if they have a small amplitude and share a common frequency range with noise signals from WTs. Therefore, governmental agencies in Germany have proposed regulations defining protected areas and minimum radii (e.g., 5 km at the Gräfenberg array in Germany[1]) that must be maintained between planned WTs and existing seismic stations. Such policies have led to strong conflicts of interest, as the operators of both WTs and seismic stations in some regions must compete for space in the same suitable areas.

With the aim of better understand the seismic emission of WTs, a number of recent studies have sought to detect and characterize the seismic noise produced by both individual and groups of WTs[1–4]. Furthermore, the correlation between meteorological data, the operation of the WT and its seismic emissions have been studied by various authors[5–7]. For instance, the interference of the wavefields emitted by multiple WTs has been modelled analytically[8], and numerical simulations have been successfully applied to earthquakes[9–12] and seismology[13]. Nonetheless, reliable estimates of the seismic wavefields produced by WTs and wind farms (WFs) in advance of their installation are still rather limited, making it difficult to judge whether the quality of records from nearby seismic stations might be strongly influenced by those wavefields. In particular, few approaches have been developed to model the seismic wavefields radiating from WTs, and these methods focus mostly on modelling the ground vibrations emitted by a single WT[14,15]. Additionally, although the effects of topography on earthquake waves have been studied for many years[16,17], the effects of topography on the seismic surface waves, which are mainly produced by a WT, have yet to be elucidated.

[1]Institute of Geosciences, Goethe-University Frankfurt, 60438 Frankfurt am Main, Germany. [2]Institute for Geothermal Resource Management (IGEM), 55411 Bingen, Germany. [3]Frankfurt Institute for Advanced Studies (FIAS), 60438 Frankfurt am Main, Germany. ✉email: limberger@igem-energie.de

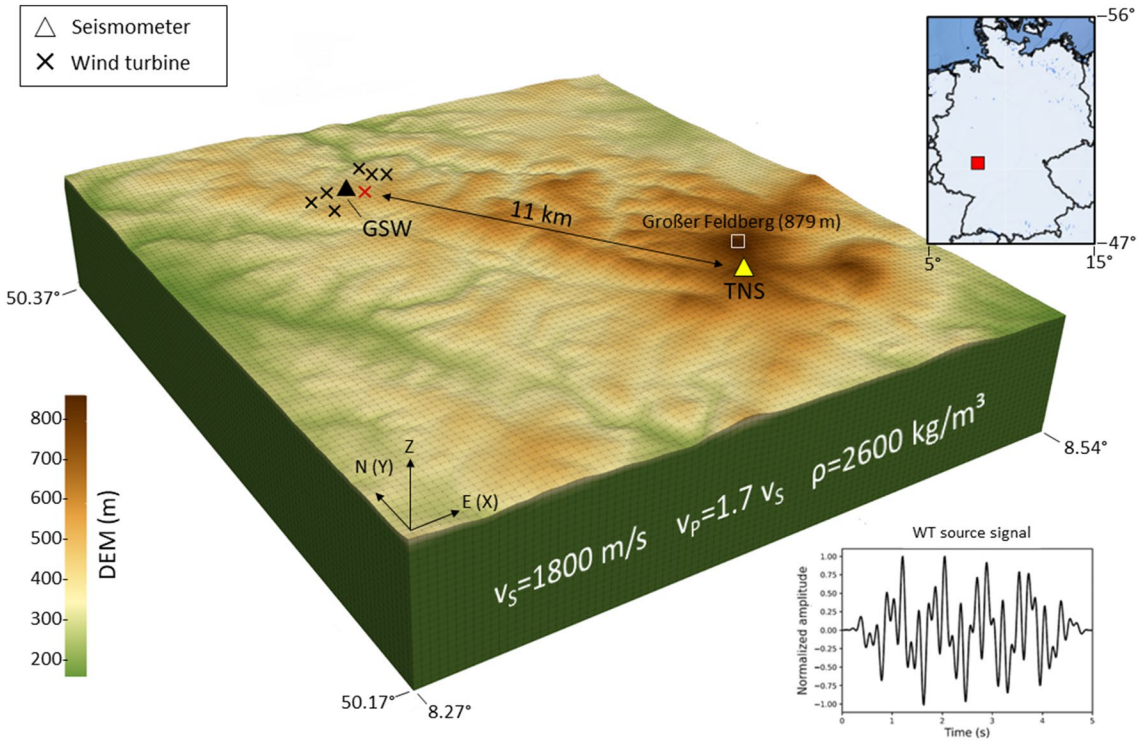

Figure 1. Model setup with a digital elevation model (DEM) of the local topography. The source time function of the WT used for modelling (bottom right) is obtained by summing three sinusoidal curves with frequencies of 1.15 Hz, 3.5 Hz and 6.0 Hz, each with a duration of 5 s. The temporary seismic station (GSW) is located within the Weilrod WF. The permanent seismic station (TNS) is located approximately 11 km from the WF atop the Kleiner Feldberg (about 1.3 km to the southwest of Grosser Feldberg). The coordinates of the model are given in WGS84. The thin grey lines indicate the computational mesh elements. The position of the WT used for simulations with one source only is marked by red cross. The computational model covers an area of 17 km × 19 km and a depth of 3.2 km.

In view of the above research gap, this study aims to develop a numerical approach to simulate the complete 3D seismic wavefield generated by 7 WTs comprising the Weilrod WF, situated northwest of Frankfurt am Main (Germany). Considering the interference of the seismic signals generated by all 7 WTs and including complex topographic effects on signal amplitudes, we compare the modelling results with observations from the closest permanent seismic station at the Taunus Observatory (TNS) located 11 km from the WF. Finally, by including wave-attenuation effects between the WF and the TNS observatory, we are able to precisely predict the noise signal amplitude at TNS based on near-field measurements. This novel approach is suitable to estimate the seismic noise field produced by WFs and to predict the noise amplitude at distant seismic stations by including effects of wavefield interferences, topography and attenuation.

Results

Observation of seismic signals emitted by wind turbines in the near and far fields. Seismic station TNS is located atop the Kleiner Feldberg (825 m a.s.l.), the second largest peak northwest of Frankfurt am Main, Germany (Fig. 1). Due to its remote location far from highways, industrial areas and railways, the station has a very low noise level of < 10 nm s^{-1} and has been providing high-quality data for the permanent monitoring of earthquake activity by the German Regional Seismic Network for more than 3 decades. The Weilrod WF, situated 11 km northwest of station TNS, was erected in 2014 and currently consists of seven Nordex N117 WTs that begin to operate if the wind speed exceeds approximately 3 m s^{-1}. To measure the frequency and amplitude of the near-field seismic signals emitted by these WTs, an additional temporary seismic station, GSW, was deployed from August 2015 to November 2015 in the centre of the WF. The Taunus mountain range rises to elevations between 200 and 879 m a.s.l. (the Großer Feldberg being the highest peak). The elevation along a line between GSW at the centre of the WF (source) and TNS (receiver) increases from approximately 450 m to 825 m a.s.l. but fluctuates due to several small valleys.

First, after processing the data (see Methods), we investigate the power spectral density (PSD) to quantify the amplitude of the seismic signals produced by the Weilrod WF at TNS and GSW. The power spectra of the data from both GSW and TNS exhibit peaks at 1.15 Hz and 3.5 Hz, which are correlated with the wind speed (Fig. 2a and c). The peak amplitude is increasing with wind speed, which agrees with the report of a recent publication showing that 1.15 Hz and 3.5 Hz spectral noise peaks are typically associated with the operation of Nordex N117 WTs[8]. However, although the WT-generated signals in the near field (at GSW) are observable between 1 and 10 Hz and even beyond 10 Hz (Fig. 2a), the amplitudes of the three sharp peaks between 2 and 3 Hz at

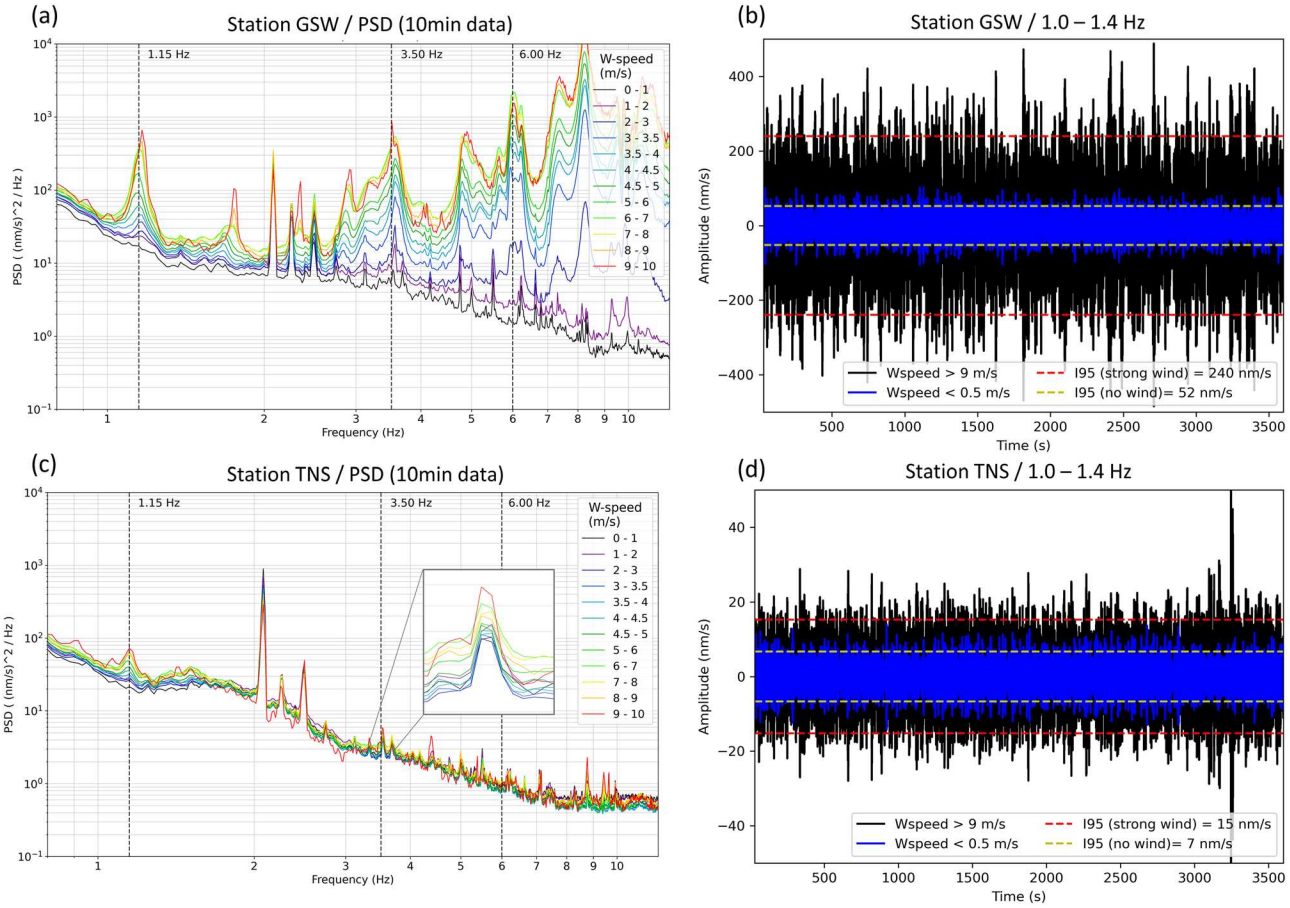

Figure 2. Power spectral density measured at near-field station GSW (**a**) and far-field station TNS (**c**) and correlated with the wind speed (from low wind speeds (black line) to high wind speeds (red line)) registered at the weather station Kleiner Feldberg. The amplitudes of the distinct peaks at 1.15 Hz and 3.5 Hz (inset in **c**) increase with wind speed and are observable at both stations. At TNS, the amplitudes are lower than at GSW due to amplitude decay with distance. One-hour seismological records during wind speeds > 9 m s^{-1} (black waveform) and < 0.5 m s^{-1} (blue waveform) are measured at the station GSW (**b**) and TNS (**d**). The I95 value is calculated for the four records to derive noise amplitudes at TNS and at GSW during strong and low wind conditions. It should be noted that the scale of the y-axis in (b) is an order of magnitude greater than in (**d**).

both stations are not increasing with the wind speed, which indicates that their origin is not related to the WTs. Moreover, additional discrete high-frequency (e.g., 6.0 Hz) peaks are observed at the near-field station (GSW), whose data are dominated by the WT-emitted signals (GSW is only 150 m from the closest WT), whereas this peak is not identified at TNS. These observations support the assumption that the two spectral peaks at 1.15 Hz and 3.5 Hz observed at TNS are associated with the operation of the Weilrod WF but are reduced in amplitude relative to those at GSW due to the decay of wave energy with increasing distance from the WF. Signals beyond 3.5 Hz that are detectable at GSW are not observable at TNS, due to attenuation and geometrical spreading effects and therefore are not considered further in the modelling.

Next, to better quantify the spectral noise amplitudes of the WF signals with 1.15 Hz in terms of maximum ground velocities at GSW and TNS (Fig. 2b and d), we determine the I95[18] values (95.45% of the amplitudes are within two times the standard deviation) of the bandpass-filtered signals with cutoff frequencies of 1 Hz and 1.4 Hz. As in similar previous studies, we use noise levels in units of ground motion velocity to allow for a more direct comparison with signal amplitudes. However, corresponding values for acceleration and displacement at station GSW and TNS are listed in the supplements (Tab. S1). For each station, we select a 1-h time segment with a wind speed < 0.5 m s^{-1} and another one-hour time segment with a wind speed > 9 m s^{-1}. The I95 noise amplitudes at GSW (TNS) in the near (far) field are approximately 240 nm s^{-1} (15 nm s^{-1}) at a high wind speed and 52 nm s^{-1} (7 nm s^{-1}) at a low wind speed. We conclude that at high wind speeds and within the frequency range of 1–1.4 Hz, the Weilrod WF, on average, causes a 2.1-fold increase (from 7 to 15 nm s^{-1}) in the noise level at TNS and that the seismic signals produced by the Weilrod WF are detectable in 11 km at TNS, because of the overall low noise level at TNS. Such an increase can affect the ability to detect small earthquakes and it can also have an impact on the determination of earthquake magnitude.

	Longitude (UTM 32U)	Latitude (UTM 32U)
TNS	460513	5563438
GSW	454005	5572704
WT1	453863	5572310
WT2	453873	5572779
WT3	453421	5572819
WT4*	454786	5572972
WT5	455338	5573613
WT6	454889	5573642
WT7	454789	5574054

Table 1. Coordinates of seismic station TNS and GSW as well as of the WTs in UTM 32U projection. WT4* is used as the source for the modelling of the radiation from a single WT.

Model setup for simulating the seismic signals from WTs. The numerical simulations are based on a 3D model (17 km × 19 km) of the uppermost crust (depth of 3.2 km) and surface topography in the region around the Weilrod WF and station TNS (Fig. 1). The model is a homogeneous half-space characterized by isotropic physical properties (no geological layering). We assign a uniform shear-wave velocity of $v_S = 1800$ m s^{-1} and compressional-wave velocity of

$$v_P = 1.7 v_S \tag{1}$$

and the density is set to 2600 kg m^{-3}. In a first step, anelastic absorption (attenuation) of waves is not included in the model to focus on topographic effects. However, further below we will include attenuation effects by specification of the seismic quality factors Q_S (for S-wave propagation) and Q_P (for P-wave propagation). The location of the source is set on the surface at the coordinate of one of the seven WTs in Weilrod (WT4 in Table 1). The source features only a vertical component (Z) to simulate an up- and downward motion at the foundation of the WT. A receiver is located at the location of TNS to extract synthetic waveforms during the numerical forward modelling. For the source time function, we sum three sinusoidal functions with frequencies of 1.15 Hz, 3.50 Hz and 6 Hz (each with a duration of 5 s), which correspond to the characteristic frequencies of the three peaks measured at GSW and TNS (Fig. 2a and c). The topography in the model is defined based on a digital elevation model (DEM) using data with a resolution of 30 m from the Global Multi-Resolution Topography (GMRT) synthesis project[19].

Simulating synthetic waveforms at TNS. To study the effects of topography on the signal amplitude at TNS, we perform simulations in an isotropic half-space model (see Methods) both including and excluding topography. To simulate wave propagation, we use the software package Salvus[20] provided by Mondaic AG/Ltd in Zurich, Switzerland. The Z, N (Y) and E (X) components of each synthetic seismogram at TNS are bandpass filtered in three frequency bands: 1.15 ± 0.3 Hz, 3.5 ± 0.3 Hz and 6.0 ± 0.3 Hz. By comparing the two model simulations with and without topography, we find that including topography reduces the signal amplitudes on all components of the 6.0 Hz signal and the Z and E components of the 3.5 Hz signal (see supplements Fig. S1), which can be explained by the scattering and reflection of waves along their paths. In contrast, the amplitudes on the N component of the 3.5 Hz signal and on all three components of the 1.15 Hz signal are greater with topography than they are without topography (see supplements Fig. S1), indicating that topography has an amplifying effect on WT-emitted signals at comparatively low frequencies. While high-frequency waves particularly suffer from scattering due to topography, low-frequency waves seem to be focused and modulated in a constructive manner along their travel path; this amplifying effect is observed in a similar way concerning earthquake waves[16,17].

Radiation from a single wind turbine. Here, to further investigate the spatially varying effects of topography on low-frequency signals, we simulate and analyse the propagation of surface waves at 1.15 Hz (the dominant frequency of the signals emitted by the WTs) using a 1.15 Hz sinusoidal source time function and generate maps of the vertical peak ground velocity (PGV) both with and without topography (Fig. 3a and b). In both cases, we use a single WT at the centre of the Weilrod WF as the source. For both model setups, we plot the spatial distribution of the topographic amplification factor A (Fig. 3c) by calculating the signal amplification or reduction in percent (%) based on Eq. (2)[16]:

$$A = \left(\frac{PGV_w}{PGV_{wo}} - 1 \right) \times 100 \tag{2}$$

where PGV_w denotes the PGV obtained with topography and PGV_{wo} denotes the PGV obtained without topography. The map of the resulting amplification factor A (Fig. 3c) indicates that the amplitudes of 1.15 Hz signals are significantly modulated by topography. This effect is especially pronounced on the mountainside to the south–southeast of TNS and Großer Feldberg, reflecting the apparent correlation between the reduction and amplification of the PGV with the DEM. In contrast, the mountain ridge between the WT source and TNS appears to act as a wave guide and preserves the signal amplitude along its path, thus opposing the expected reduction with geometrical spreading. Generally, however, the PGVs decrease with increasing distance from

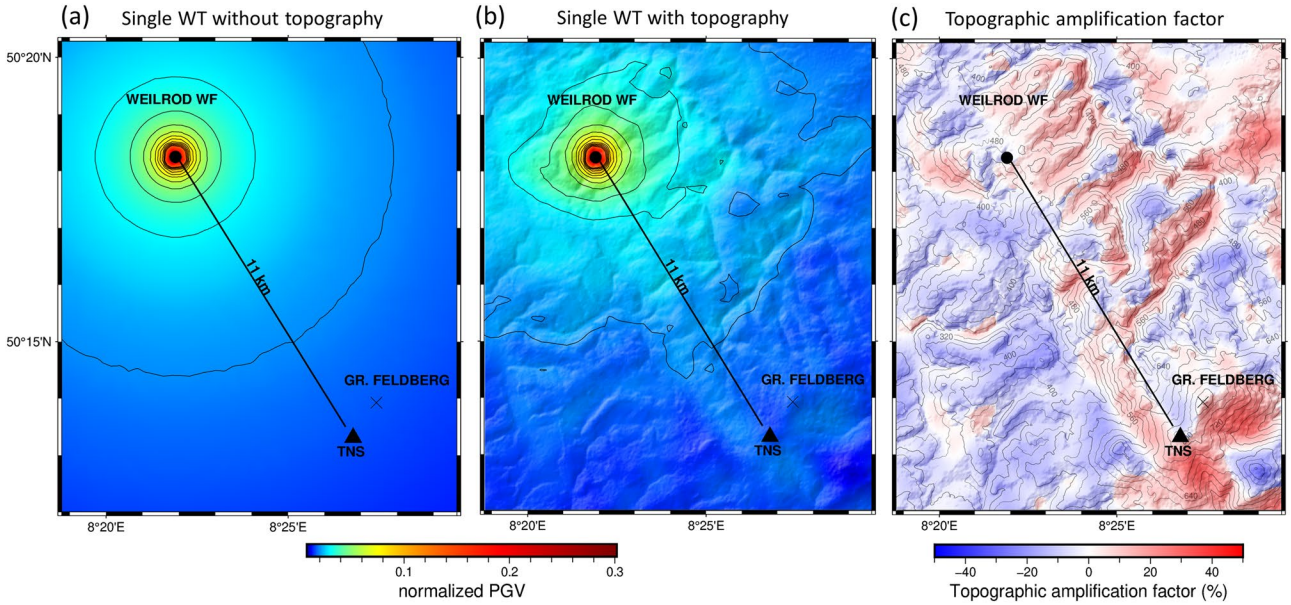

Figure 3. Peak ground velocity (PGV) maps without (**a**) and with (**b**) topography and the resulting map of the amplification due to topography (**c**) for a single WT at the centre of the Weilrod WF showing that the amplitude increases at the permanent station (TNS). The amplitudes in (**a**) and (**b**) are normalized to the maximum amplitude in Fig. 4c (with 7 WTs), to compare the radiation of a single and multiple WTs. Note: The contour lines in (**c**) are representative of the digital elevation model.

the WF. Even for a single WT in Weilrod, however, we can demonstrate the amplifying effect of the topography on the signal amplitude near TNS.

Radiation from multiple wind turbines considering the effects of wavefield interference. The wavefield of a single WT can differ significantly from the complete wavefield of an entire WF due to constructive and destructive interference[8]. To consider these effects in detail, we expand our study and place a source at each of the 7 WTs in the Weilrod WF and numerically simulate 100 PGV maps without topography using a randomly chosen signal phase of the sinusoidal time function for each of the seven sources. The modelling results show both destructive interferences, resulting in a low PGV at TNS (Fig. 4a), and constructive interference, yielding relatively high PGVs (Fig. 4b). Since the WTs are not all expected to vibrate in phase, a single interference pattern can represent only a snapshot of the ground motion before the radiation generates another pattern. Therefore, to derive a representative radiation pattern, we averaged 100 different PGV maps (Fig. 4c), thereby avoiding the predominance of any single interference pattern. The resulting average PGV map (Fig. 4c) shows the decrease in amplitude with increasing distance from the WF, but the obtained pattern differs clearly from the two patterns with either only destructive interference or only constructive interference.

Radiation from multiple wind turbines considering the effects of wavefield interference, topography, and attenuation. Finally, we calculate the average PGV distribution produced by the whole Weilrod WF considering both the effects of topography and the interference caused by the emissions of multiple WTs (Fig. 5a). The same set of randomly chosen phases of the source time functions used for the case without topography (Fig. 4c) is used again in this case, and 100 individual PGV maps are averaged, allowing us to compare the average PGV distributions obtained without (Fig. 4c) and with (Fig. 5b) topography. In the same manner as Fig. 3c, a map of the PGV amplification factor is obtained (Fig. 5b), the distribution of which reveals that amplitudes are preserved along the mountain ridge between the WF and TNS if topography is included in the model. The minimum amplification factor in the study area is − 20% (an amplitude reduction of 20%), while the maximum value is 30% (inset in Fig. 5b); however, such high amplification factors (values > 20%) are limited to a small proportion (< 1%) of the total area. Generally, the map of the amplification factor is comparable to that in the scenario with only a single WT (Fig. 4c), although considering all seven WTs causes some amplification areas to be enlarged, generally along the mountainsides facing away from the source (e.g., to the south of TNS and Großer Feldberg, similar to Fig. 4c). In contrast, amplitude reductions are associated mostly with valleys[16]. By comparing the synthetic waveforms at TNS for each of the 100 interference scenarios with and without topography, we infer that the amplitude at TNS increases by approximately 9% on average if topography is considered (see supplements Fig. S2). Generally, with respect to the 100 specific interferences, an amplification due to the topography near TNS is much more likely than a reduction (see supplements Fig. S2).

To further investigate the decay of the PGV, we extract the PGVs along a straight line connecting the location of GSW to TNS and plot the simulation results both including and excluding topography (Fig. 5c). The amplitude steadily decreases logarithmically with increasing distance from the WF if topography is not included, as expected, whereas the amplitude decreases globally with topography but increases locally (e.g., at distances of

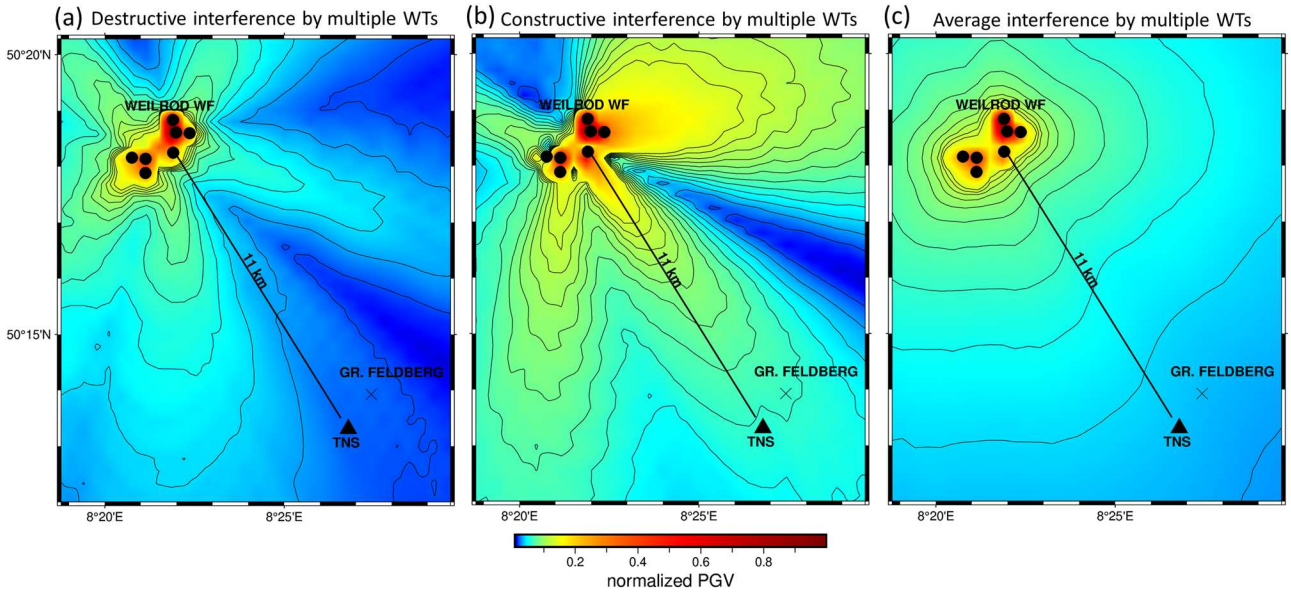

Figure 4. The specific destructive (**a**) and constructive (**b**) interference of the wavefields produced by multiple WTs results in low and high normalized PGVs, respectively, at TNS. The interference (radiation) pattern in (**c**) is obtained by averaging 100 PGV maps calculated with a randomly chosen phase for each source time function of the 7 sources. Topography is not included here. The amplitudes are normalized to the maximum amplitude that occurs and is therefore 1 at the source location.

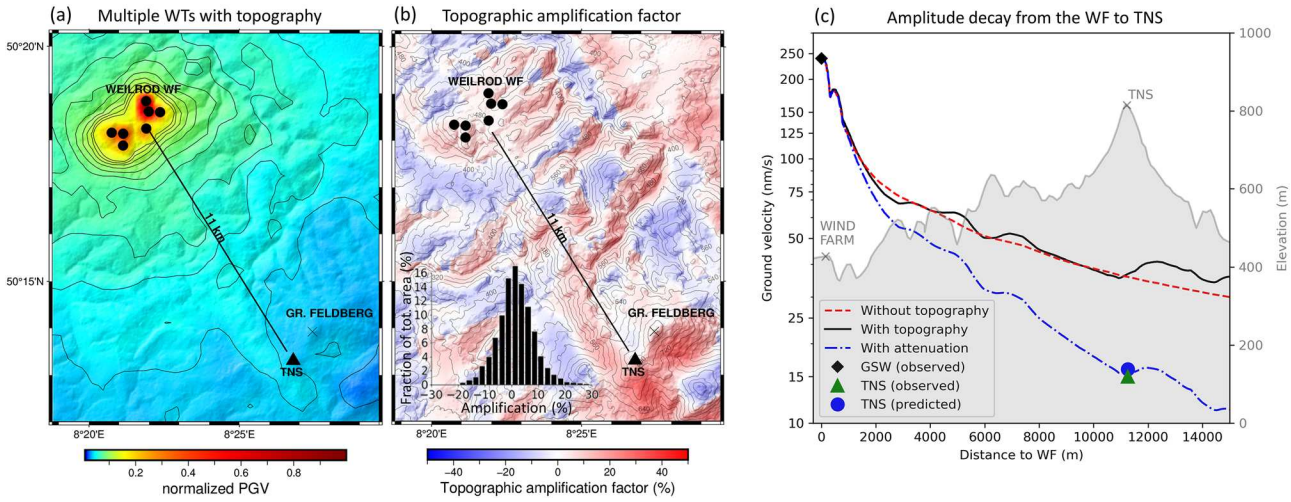

Figure 5. Maps of the average peak ground velocity (PGV) with topography (**a**) and the amplification factor due to topography (**b**) for all seven WTs in the Weilrod WF. On average, the amplification at TNS due to topography is about 9%. The PGVs along a straight line between the centre of the WF (station GSW) and permanent station (TNS) are extracted and calibrated with respect to the measured PGVs at the temporary station (GSW) within the WF (**c**). The measured amplitude at TNS is finally predicted including attenuation in the model. The distribution of the obtained amplification factor in the model domain ranges from − 20 to 30% (histogram in **b**). The amplitudes in (**a**) are normalized to the maximum amplitude that occurs and is therefore 1 at the sources. Note: The contour lines in (**b**) are based on the digital elevation model and the left y-axis in (**c**) is logarithmic.

4–5 km, 6–8 km and 11–15 km). The sudden increase of amplitudes at a distance of 500 m is observable for the case with and without topography and is likely a consequence of wavefield interferences. In case of attenuation using $Q_S = 25$ and $Q_P = 40$, the amplitude decay with distance is higher; however, the local topographic effects remain. As mentioned before, the amplitudes significantly increase on the mountainside behind TNS opposite the WF. The PGVs along the line are calibrated to the noise amplitude (I95) of approximately 240 nm s^{-1} measured at GSW for wind speeds > 9 m s^{-1} (Fig. 2b). This means that the simulated amplitude at the location of GSW is matched up with the I95 value measured at GSW. Furthermore, we measure an amplitude (I95) of approximately 15 nm s^{-1} at TNS at wind speeds > 9 m s^{-1} (Fig. 2d). The resulting simulated amplitude including the effects of interferences, topography, and attenuation fits well with the observed amplitude of 15 nm s^{-1} at

TNS, which means that the measured amplitude at TNS is predictable if these effects are included. Overall, this analysis demonstrates that the amplitude of noise at TNS (and other areas in the Taunus region) caused by low-frequency WT signals is underestimated if topography is neglected.

Discussion

In this study, we present a novel numerical modelling approach to predict seismic noise amplitudes generated by a WF and we show that wavefield interferences of multiple WTs significantly affect the seismic radiation pattern of a WF. Furthermore, we demonstrate that topographic effects lead to local reductions, but also amplifications of the noise signal amplitude, especially for low-frequency signals. Finally, we show that we can predict the noise amplitude at a distant station using near-field measurements at a WF if attenuation is assigned to the model. In terms of aiming noise amplitude predictions, these effects can be significant which is why they should be considered in the modelling process.

Characteristic seismic signals produced by the Weilrod WF are detectable 11 km away at the TNS seismic observatory. The noise amplitudes regarding the I95 criteria are derived from both near- and far-field measurements at wind speeds above a sufficiently high threshold of 9 m s^{-1}, at which the WTs are fully operating. The amplitudes show a significant increase in the seismic noise level at a frequency of 1.15 Hz, which is due to the operation of the WTs. Particularly the low-frequency signals emitted by WTs are of importance since the corresponding waves travel far (here 11 km) due to a weak wave damping and these signals are therefore widely detected[2,8]. Using our 3D model, we numerically simulate the seismic emissions of seven WTs at the Weilrod WF both including and excluding topography. When topography is included during the modelling, the synthetic seismograms at TNS located atop the Kleiner Feldberg display reduced signal amplitudes at high frequencies (e.g., 6.0 Hz) but amplified signals at low frequencies (1.15 Hz). Upon plotting the distribution of the modelled PGV, we find a systematic correlation between the topography and the amplification factor induced by the terrain, such as amplifying and reducing effects of mountain ridges and valleys, respectively[16]. Averaging the seismic radiation patterns guarantees that no single constructive or destructive interference pattern is dominant, and therefore, the average radiation pattern better approximates the representative seismic radiation of the WF. This demonstrates that the inclusion of interferences, topography and attenuation enables the amplitude of WT-induced noise at a distant seismometer to be accurately estimated. Such a prediction requires calibration measurements in the near field of the corresponding WF. If the predictions are necessary before the installation of a WF, we recommend to measure seismic amplitudes in the near field of WTs that have the same or similar type and dimensions as the planned WTs, to enable a sufficient calibration of the modelled amplitudes. Generally, different WT types and numbers can be considered in one and the same model. However, predictions of the signals produced by WTs in a region with pronounced terrain could underestimate the noise amplitude if the local topography is neglected.

The data analysis and modelling in this study are based on specific assumptions and the data used have some limitations to be discussed. We correlate the seismic records with data of wind speeds measured at the TNS observatory and not at the Weilrod WF. A more accurate correlation could be achieved using operational data from the WTs (e.g., rotation rate)[6], however, this data was not available for this study. To calibrate the simulated noise amplitudes at the distant seismometer, we use measurements from one seismic station in the near field of the WF assuming that geological and topographic effects along this short distance from the WT to the seismometer are negligible. This calibration could be improved by using two or more near-field measurements to increase the reliability of the calibration. Furthermore, we assign specific attenuation values to model the noise amplitude at the distant station. The chosen quality factors are plausible to describe upper crustal damping of seismic waves[21,22], however, different values could be considered. Finally, large-scale geological structures in the subsurface, which are not included in this study, might have a significant effect on the wave propagation as well. In view of these points, estimating the amplitudes of noisy signals emitted by a WF prior to its installation encounters three main challenges: the limited availability of robust calibration measurements at a WT with the specifications needed to calibrate the source amplitude, the lack of information regarding possible major structures and geophysical properties in the shallow subsurface, and the lack of access to reliable meteorological data or operational data of the WTs. However, missing information on the subsurface can be obtained by, e.g., using geophysical imaging. Furthermore, the lack of precise operational data of the WTs can be sufficiently filled using open access meteorological data provided by weather services, as we demonstrate in our study. To finally evaluate the effect of a WF on a nearby seismometer, the background noise level measured at seismic stations should be considered, and from this relationship, the effect of a new WF on seismometer measurements can be assessed.

Our results show that the presented modelling approach is capable of simulating the effects of topography, wavefield interference and attenuation and therefore can provide higher-accuracy predictions of the amplitudes of noisy signals generated by multiple WTs. Our approach has been validated with data measured at a temporary seismic station within an existing WF and a permanent station at a distant seismic observatory. A preliminary version of the approach was tested in a previous study[8]. As the first numerical modelling approach that includes topography, interferences and attenuation, our approach can be adapted to consider arbitrary WF geometries. Furthermore, it can be employed in different locations to predict the potential influences of planned WFs on nearby seismometers, thus providing necessary information for authorities and agencies as well as the operators of WFs and seismic observatories. Possible applications are, as presented, the estimation of the seismic radiation of a single WT, multiple WTs or WFs in a region and the effect of replacing (repowering) old WTs by modern ones. In future, the approach will be applied and extended to study the influence of geological structures, specific noise-reducing WF geometries and various source mechanisms of the WTs. This would further improve the understanding of seismic emissions from a WF and would finally result in more precise predictions.

Methods

Data processing and power spectral density. We analysed continuous data (100 Hz sampling frequency) recorded at the two seismic stations, TNS and GSW, between August 20, 2015, and November 26, 2015. At TNS, a Streckeisen STS-2 Sensor and a REFTEK 130 data logger are permanently installed. At GSW, a Nanometrics Trillium Compact (120 s) sensor and a Nanometrics Taurus data logger were installed. The data was restituted to derive true ground motions (ground velocity). We cut the data into 10-min time segments and obtained approximately 15,000 time segments per station, yielding 30,000 segments in total. The power spectral density (PSD) was calculated for each time segment for both data sets using the method proposed by Welch (1967)[23]. We used a moving window length of 60 s to compute the PSD for each 10-min time segment; thus, the PSD of each 10-min segment was generated by averaging the PSDs of 10 shorter segments. Then, to each of the average PSDs derived from the 30,000 10-min time segments, we assigned a wind speed based on meteorological data with a 10-min sampling interval provided by the German Weather Service (weather station Kleiner Feldberg)[24]. The data were assigned by matching up the times of the seismic and meteorological records. Using bin sizes of 0.5 m s^{-1} or 1 m s^{-1}, the PSDs were then binned into wind speeds between 0 and 10 m s^{-1} because the wind speed never exceeded 10 m s^{-1} (during the time period of the measurements). To remove outliers and transient or undesired signals (related to, e.g., mining explosions or earthquakes), we clipped the PSD data set for each station by excluding the 50% of the data set corresponding to the largest spectral amplitudes because we found that the frequency peaks in the spectra became sharper by removing 50% of the data before averaging. For the remaining 50%, we calculated the average power spectrum for each wind speed bin (Fig. 2).

Quantification of noise amplitudes. With the aim of deriving noise amplitudes as ground velocities with respect to the I95[18] criteria at both stations in the case of high and low wind speeds, we examined the meteorological data for one-hour time windows with average wind speeds of < 0.5 m s^{-1} (2015-10-19, 03.00 a.m.) and > 9 m s^{-1} (2015-11-18, 4:00 a.m.) (Fig. 2). For these time periods, we bandpass-filtered the corresponding seismic records from GSW and TNS between 1 and 1.4 Hz with a 4th-order butterworth filter and calculated the corresponding I95 values. We are aware that we compare I95 values (from observations) with PGVs (from simulations), however, PGVs are not suitable to properly describe the observed noise amplitude of the harmonic continuous noise signals from the WTs we were dealing with at TNS and GSW. Therefore, we presumed the I95 values to be representative as a quantification of the noise level and hence to be suitable to be compared with the simulated PGVs.

Numerical simulation of a single wind turbine. To numerically simulate the propagation of waves through an isotropic medium (i.e., ground motions) at the far-field station (TNS), we used the commercial software package Salvus[20], which is a suite of software for performing full waveform modelling and inversion provided by Mondaic AG/Ltd. (Zurich). The topography of the model was obtained from the Global Multi-Resolution Topography (GMRT) synthesis project[19]. The model had an extension of 17 km × 19 km and a depth of 3.2 km. The simulations are performed based on a mesh with minimum 2 elements per signal wavelength. However, to guarantee accurate simulation results, we considered the source frequency (e.g., 1.15 Hz) plus 1 Hz to be the reference for the simulation. Therefore, we derived a grid spacing of about 420 m (1800 m s^{-1}/2.15 Hz/2 elements) when simulating 1.15 Hz signals with an S-wave velocity of 1800 m s^{-1}. This also implies that we used a coarser grid for simulation of 1.15 Hz signals than for simulations with 6 Hz signals. We tested the sensitivity of the results to the resolution using 2 and 4 elements per wavelength and we found no significant difference between the results. The meshing is done internally by the software. The model had a free surface at the top, but sufficiently absorbing boundaries at all other sides. To model the seismic source, we placed a vertical force vector of 1 N m at a WT in the centre of the Weilrod WF. The source is located at the surface of the computational domain at the position of a WT. Based on the signals measured at both GSW and TNS, we simulated the propagation of the wavefield with dominant frequencies of 1.15 Hz, 3.5 Hz and 6 Hz in a homogenous half-space both with and without topography. The source time function was a sum of a 1.15 Hz, 3.5 Hz and 6 Hz sinus function and is tapered with a Tukey window to avoid discontinuities at the beginning and end of the source wavelet.

Numerical simulation of multiple wind turbines. To consider the effects of wavefield interference, we simulated 100 wavefields (scenarios), each with a randomly chosen set of signal phases at each of the 7 WTs (sources), using a 1.15 Hz sinus wavelet as a source time function. Instead of using a random signal phase[8] between 0 and π, we used a value between 0 and 2π to consider as many as possible scenarios of wave interferences. Then, we extracted the peak ground velocity (PGV), which means the maximum occurring magnitude of amplitude at each element in the mesh, for all scenarios. Finally, the PGVs of all scenarios were averaged to obtain a radiation pattern that was not dominated by a single interference source. Then, we interpolated the resulting surface data for better visualization. This procedure is represented graphically in the supplements (Fig. S3) and was executed for the cases both with and without topography. To determine the spatial distribution of the amplification due to topography, the topographic amplification factor was computed from the two average radiation patterns using Eq. (1). The simulated amplitude decay from the WF to TNS was extracted from the simulated radiation pattern and calibrated with the noise amplitude (I95) obtained from measurements at GSW. Finally, we performed the simulation of 100 wavefields including attenuation using seismic quality factors of $Q_S = 25$ (S-wave) and $Q_P = 40$ (P-wave). Again, the simulated amplitude decay was calibrated with the amplitude values obtained from measurements at GSW. The quality factors were chosen in a way, that the predicted amplitude at TNS approximately matched up with the observed amplitude.

Data availability

The raw seismological data that were processed in this study are available from Goethe University Frankfurt. The meteorological data is open source and is provided by the German Weather Service[24]. All datasets used and analysed during the current study are available from the corresponding author (limberger@igem-energie.de) on request.

Code availability

Data processing was performed using the Python packages NumPy, SciPy and ObsPy[25]. The numerical simulations were performed using the commercial software package Salvus[20]. The Figures were partly prepared using Python Generic Mapping Tool (PyGMT v0.5.0, www.pygmt.org)[26].

Received: 4 May 2022; Accepted: 5 September 2022
Published online: 15 September 2022

References

1. Stammler, K. & Ceranna, L. Influence of wind turbines on seismic records of the Gräfenberg array. *Seismol. Res. Lett.* **87**, 1075–1081 (2016).
2. Saccorotti, G., Piccinini, D., Cauchie, L. & Fiori, I. Seismic noise by wind farms: A case study from the Virgo gravitational wave observatory, Italy. *Bull. Seismol. Soc. Am.* **101**, 568–578 (2011).
3. Gaßner, L. *et al.* Joint Analysis of resident complaints, meteorological, acoustic, and ground motion data to establish a robust annoyance evaluation of wind turbine emissions. *Renew. Energy* **188**, 1072–1093 (2022).
4. Westwood, R. F. & Styles, P. Assessing the seismic wavefield of a wind turbine using polarization analysis. *Wind Energy* **20**, 1841–1850 (2017).
5. Zieger, T. & Ritter, J. R. R. Influence of wind turbines on seismic stations in the upper Rhine Graben, SW Germany. *J. Seismol.* **22**, 105–122 (2018).
6. Neuffer, T., Kremers, S. & Fritschen, R. Characterization of seismic signals induced by the operation of wind turbines in North Rhine-Westphalia (NRW), Germany. *J. Seismol.* **23**, 1161–1177 (2019).
7. Lerbs, N., Zieger, T., Ritter, J. & Korn, M. Wind turbine induced seismic signals: The large-scale SMARTIE1 experiment and a concept to define protection radii for recording stations. *Near Surface Geophys.* **18**, 467–482 (2020).
8. Limberger, F., Lindenfeld, M., Deckert, H. & Rümpker, G. Seismic radiation from wind turbines: Observations and analytical modeling of frequency-dependent amplitude decays. *Solid Earth* **12**, 1851–1864 (2021).
9. Olsen, K. B., Archuleta, R. J. & Matarese, J. R. Three-dimensional simulation of a magnitude 7.75 earthquake on the San Andreas fault. *Science* **139**, 1628–1632 (1995).
10. Olsen, K. B. Site amplification in the Los Angeles basin from three-dimensional modeling of ground motion. *Bull. Seismol. Soc. Am.* **90**, S77–S94 (2000).
11. Komatitsch, D., Ritsema, J. & Tromp, J. The spectral-element method, Beowulf computing, and global seismology. *Science* **298**, 1737–1742 (2002).
12. Roten, D., Olsen, K. B. & Takedatsu, R. Numerical simulation of m9 megathrust earthquakes in the Cascadia subduction zone. *Pure Appl. Geophys.* **177**, 2125–2141 (2019).
13. Colombi, A., Roux, P., Guenneau, S., Gueguen, P. & Craster, R. V. Forests as a natural seismic metamaterial: Rayleigh wave bandgaps, induced by local resonances. *Sci. Rep.* **6**, 19238 (2016).
14. Gortsas, T. V., Triantafyllidis, T., Chrisopoulos, S. & Polyzos, D. Numerical modelling of micro-seismic and infrasound noise radiated by a wind turbine. *Soil Dyn. Earthq. Eng.* **99**, 108–123 (2017).
15. Zieger, T. *et al.* Simultaneous identification of wind turbine vibrations by using seismic data, elastic modeling and laser Doppler vibrometry. *Wind Energy* **23**, 1145–1153 (2020).
16. Lee, S.-J., Chen, H.-W., Komatitsch, D., Huang, B.-S. & Tromp, J. Three-dimensional simulations of seismic-wave propagation in the Taipei basin with realistic topography based upon the spectral-element method. *Bull. Seismol. Soc. Am.* **98**, 253–264 (2008).
17. Lee, S.-J., Komatitsch, D., Huang, B.-S. & Tromp, J. Effects of topography on seismic-wave propagation: An example from northern Taiwan. *Bull. Seismol. Soc. Am.* **99**, 314–325 (2009).
18. Groos, J. & Ritter, J. Time domain classification and quantification of seismic noise in an urban environment. *Geophys. J. Int.* **179**(2), 1213–1231 (2009).
19. Ryan, W. B. F. *et al.* Global multi-resolution topography synthesis. *Geochem. Geophys. Geosyst.* **10**, Q03014 (2009).
20. Afanasiev, M. *et al.* Modular and flexible spectral-element waveform modelling in two and three dimensions. *Geophys. J. Int.* **216**, 1675–1692 (2019).
21. Grad, M. & Luosto, U. Seismic velocities and Q-factors in the uppermost crust beneath the sveka profile in Finland. *Tectonophysics* **230**, 1–18 (1994).
22. Tian, W. & Li, Z. *S* wave anelastic attenuation of shallow sediments in mainland China. *Earth Space Sci.* **7**, 10 (2020).
23. Welch, P. The use of fast Fourier transform for the estimation of power spectra: A method based on time averaging over short, modified periodograms. *IEEE Trans. Audio Electroacoust.* **15**, 70–73 (1967).
24. DWD Open Data Server. https://opendata.dwd.de/ (2017).
25. Beyreuther, M. *et al.* ObsPy: A Python toolbox for seismology. *Seismol. Res. Lett.* **81**, 530–533 (2010).
26. Uieda, L., Tian, D., Leong, W. J., Jones, M., Schlitzer, W. *et al.* PyGMT: A Python interface for the Generic Mapping Tools (v0.7.0). Computer software. Zenodo. (2022)

Acknowledgements

We thank the German Federal Ministry for Economic Affairs and Climate Action (FKZ no. 0324360) and ESWE Innovations und Klimaschutzfonds for their support in performing this study.

Author contributions

F.L. processed the seismic data and performed the numerical simulations. G.R. provided the motivation for this study and the seismic data, participated in developing the model, and supervised the writing of the article. F.L. and G.R. interpreted the results and completed the manuscript together. M.L. was involved in the measurements at the wind farm. F.L., G.R., M.L. and H.D. each edited the article.

Funding
Open Access funding enabled and organized by Projekt DEAL.

Competing interests
The authors declare no competing interests.

Additional information
Supplementary Information The online version contains supplementary material available at https://doi.org/10.1038/s41598-022-19799-w.

Correspondence and requests for materials should be addressed to F.L.

Reprints and permissions information is available at www.nature.com/reprints.

Publisher's note Springer Nature remains neutral with regard to jurisdictional claims in published maps and institutional affiliations.

5. The impact of seismic noise produced by wind turbines on seismic borehole measurements

---

This chapter is **under review** in:

Limberger, F., Rümpker, G., Lindenfeld, M., & Deckert, H. (2023): The impact of seismic noise produced by wind turbines on seismic borehole measurements, EGUsphere

---

https://doi.org/10.5194/egusphere-2023-45
Preprint. Discussion started: 7 February 2023

The impact of seismic noise produced by wind turbines on seismic borehole measurements

Fabian Limberger[1,2], Georg Rümpker[1,3], Michael Lindenfeld[1], and Hagen Deckert[2]

[1]Institute of Geosciences, Goethe-University Frankfurt, 60438 Frankfurt am Main, Germany
[2]Institute for Geothermal Resource Management (igem), 55411 Bingen, Germany
[3]Frankfurt Institute for Advanced Studies (FIAS), 60438 Frankfurt am Main, Germany

Correspondence to: Fabian Limberger (limberger@igem-energie.de)

Abstract. Seismic signals produced by wind turbines can have an adverse effect on seismological measurements up to distances of several kilometres. Based on numerical simulations of the emitted seismic wavefield, we study the effectivity of seismic borehole installations as a way to reduce the incoming noise. We analyse the signal amplitude as a function of sensor depth and investigate effects of seismic velocities, damping parameters and geological layerings in the subsurface. Our numerical approach is validated by real data from borehole installations affected by wind turbines. We demonstrate that a seismic borehole installation with an adequate depth can effectively reduce the impact of seismic noise from wind turbines in comparison to surface installations. Therefore, placing the seismometer at greater depth represents a potentially effective measure to improve or retain the quality of the recordings at a seismic station. However, the advantages of the borehole decrease significantly with increasing signal wavelength.

1 Introduction

Global warming, energy crises and hence the goal to reduce the dependency on fossil energies demonstrate the relevance of exploiting renewable energies, including wind power. Thus, the increase of the number of wind turbines (WTs) plays a key role in the coming years. WTs are preferably installed in remote areas with windy conditions to increase the power production and to minimize their impacts (e.g., shadowing, acoustic noise and infrasound) on the environment. Seismic stations are often located in areas with similar conditions due to the low seismic noise levels compared to urban areas with anthropogenic noise sources as traffic, industry and railways. Nevertheless, the vibration of WTs can have a significant impact on seismic stations and networks. However, the effects strongly depend on the distance between the seismometer and the WT.

Seismic signals of WTs are characterized by frequencies between 1 Hz and 10 Hz and have been described in detail in a number of studies (e.g., Saccorotti et al., 2011; Stammler and Ceranna, 2016; Zieger and Ritter, 2018). The systematic decays of the corresponding signal amplitudes with distance from the WT or wind farms (WFs) have been analysed at various WFs (Neuffer and Kremers, 2017; Limberger et al., 2021; Gassner et al. 2022). Analytical and numerical approaches to model the amplitudes have been developed in terms of considering single WTs (Gortsaset al., 2017; Lerbs et al., 2020; Abreu et al., 2022)

https://doi.org/10.5194/egusphere-2023-45
Preprint. Discussion started: 7 February 2023

and complete WFs (Limberger et al., 2021, 2022) including wavefield interferences from multiple WTs. On this basis, methods for predicting and reducing seismic noise from WTs or other noise sources are developed taking into account, e.g., meta materials (Colombi et al., 2016; Abreu et al., 2022), interferences and topographic effects (Limberger et al., 2021, 2022) and denoising methods (e.g., Heuel and Friederich, 2022). However, effective and robust solutions to compensate the seismic noise without losing the quality of the natural seismological signals are missing. It is generally known that seismometers in boreholes have lower noise levels compared to stations at the surface (Withers et al., 1996; Boese et al., 2015) which can improve the detectability of seismic events even in urban areas (Malin et al. ,2018). Boese et al. (2015) reported a noise level reduction of up to 30 dB (average 10 dB) on a 383 m deep borehole sensor compared to a surface sensor for frequencies ≥ 1 Hz. Similar effects of borehole installations on signals from WTs are shown by Zieger and Ritter (2018). They compared signals measured in boreholes with surface data and showed a significant reduction of the surface wave amplitude induced by a nearby WF. Neuffer and Kremers (2017) analysed data from borehole stations as well, but did not systematically study the relation to surface data. Nevertheless, they estimated a noise reduction by an order of magnitude due to the borehole installation. Obviously, borehole installations can play a relevant role in reducing the noise of WTs at seismometers. However, their capabilities, limitations and the predictability of its effectivity has not been studied in detail.

Here, we investigate the effectivity of borehole installations using numerical simulations. We perform sensitivity studies in view of signal frequencies, seismic velocities, homogeneous and layered subsurface structures, attenuation and the distance between source and receivers on depth-dependent signal amplitudes. We compare our numerical results with data from borehole measurements reported by Zieger and Ritter (2018). Our results provide constraints on the distances between WT and seismic stations necessary to reduce the noise levels to a desired level.

https://doi.org/10.5194/egusphere-2023-45
Preprint. Discussion started: 7 February 2023

2 Model setup and data processing

2.1 Description of the numerical model

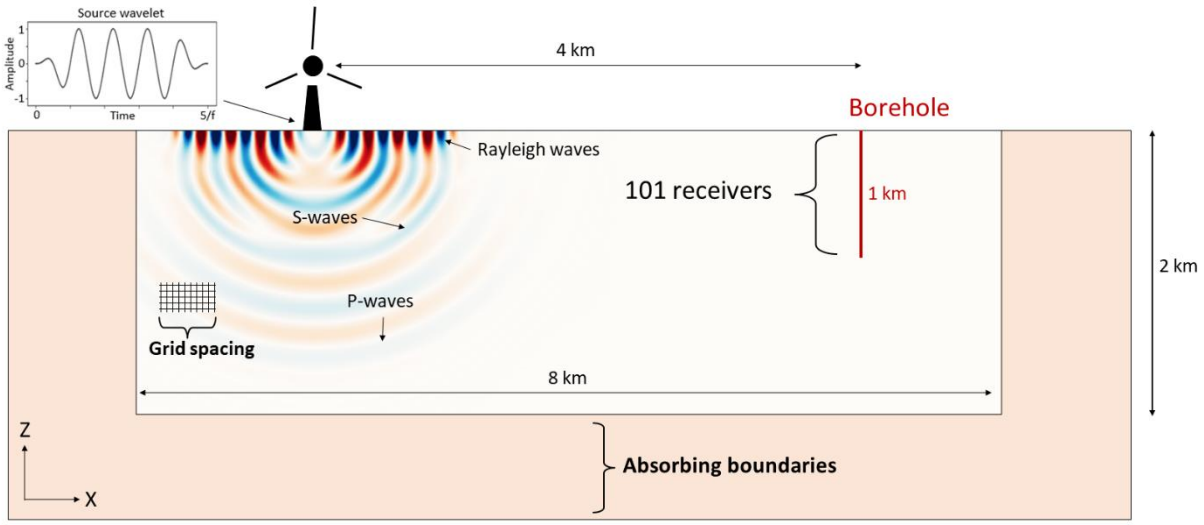

Figure 1: The numerical model includes a sinusoidal source wavelet, receivers located along a line from surface to a depth of 1 km and a sufficient grid spacing (three elements per minimum wavelength of the simulation) as well as absorbing boundaries (two times the maximum wavelength of the simulation). P-waves, S-Waves and surface waves are simulated during the forward modelling. Synthetic seismograms are extracted at positions indicated by the red line (borehole).

The forward modelling of the wave propagation is performed in two dimensions (x-z plane) using the software package Salvus (Afanasiev, et al., 2018), which enables the simulation the complete wavefield (P-wave, S-wave and surface waves, including conversion and scattering effects). A comparison of the results with a simulation in three dimensions shows that a two-dimensional approach seems sufficient for addressing the described problem (the corresponding data are in the supplements (Fig. S1)). The seismic source is located at the surface of the model domain (Fig. 1). The source wavelet is a tapered sinusoidal function with a length of five signal periods, which implies that the source duration increases for simulations with lower frequencies. The exciting force is assumed to be vertically oriented. The modelling domain has a length of 8 km (x-direction) and a depth of 2 km. Absorbing boundaries are added to all sides, except for the free surface on top of the model. The absorbing boundary has a minimum thickness of two times the maximum wavelength used during the simulation to sufficiently suppress reflections at the sides. A synthetic 1-km deep borehole is located in a distance of 4 km from the source. Receivers are located at intervals of 10 m along the borehole to extract the synthetic seismograms at 101 positions. In this work, we study the effects of both homogeneous and layered models including effects of varying seismic velocities. The velocity of the P-wave is calculated from V_P=1.7 x V_S and the density is 2600 kg m^{-3} in every simulation. The source frequency is systematically increased from 0.2 Hz to 6 Hz (step size 0.2 Hz) to cover a wide range of typical signal frequencies observed for WTs (see

https://doi.org/10.5194/egusphere-2023-45
Preprint. Discussion started: 7 February 2023

references). A separate simulation is performed for each frequency and model. The grid spacing is generated using three elements per minimum wavelength to avoid numerical artefacts. All studied models are listed in Table 1. Models 1-9 are used to study general effects of seismic velocities, geological layerings and attenuation. Model 10 is generated based on results from the MAGS2 project (Spies et al., 2017), which provided detailed information on the seismic velocities in the region of Landau in Rhineland-Palatinate, Germany. We use this information about the local subsurface to establish a corresponding average velocity model (Fig. S2) and to perform the real data validation of our proposed solutions.

Table 1: List of models used in this study. Models 1-9 are generic to study effects of geophysical parameters and layers in the subsurface. Model 10 is used for the validation with real data. The quality factor Q describes the loss of energy per seismic wave cycle due to anelastic processes or friction inside the rock during the wave propagation. The damping of the P-wave and S-wave is decreasing with increasing Q_P and Q_S.

ID	DESCRIPTION	V_{S1}	V_{S2}	V_{S3}	V_{S3}	V_P
Model1	Homogeneous half space	500	-	-	-	1.7 V_S
Model2	Homogeneous half space	1000	-	-	-	
Model3	Homogeneous half space	1500	-	-	-	
Model4	Two layers (z=-200m), low velocity	500	1000	-	-	
Model5	Two layers (z=-200m), mid velocity	1000	1500	-	-	
Model6	Two layers (z=-200m), high velocity	2000	3000			
Model7	Three layers (z_1=-200m, z_2=-400m)	500	1000	1500	-	
Model8	Two layers (z=-200m), weak attenuation	Model 4 including Q_S=100, Q_P=200				
Model9	Two layers (z=-200m), strong attenuation	Model 4 including Q_S=30, Q_P=60				
Model10 (Fig. S2)	Landau model (**real data validation**), four layers, no att. (z_1=-200m, z_2=-400m, z_3=-600m)	450	750	900	1150	

2.2 Post-processing of the synthetic seismograms and comparison to analytical solutions

For each single simulation synthetic seismograms (or traces) are extracted at every receiver location in the synthetic borehole (gray lines in Fig. 2). The maximum amplitude for each trace (vertical component) is obtained to derive a frequency-dependent relation between signal amplitude and depth (red line in Fig. 2). The frequency-dependent amplitudes with depth are normalized to the amplitude at the surface. Finally, the interpolation of the resulting data shows the spectral amplitudes in dependency of the borehole depth (Fig. 3a).

https://doi.org/10.5194/egusphere-2023-45
Preprint. Discussion started: 7 February 2023

As a benchmark, we compare the numerical results with two analytical solutions (Fig. 3b). The first solution (coloured interpolation in Fig. 3b) is based on a formulation of Barkan (1962)

$$A_z = \left(-0.2958e^{-\frac{(0.8474)2\pi z}{\lambda}} + 0.1707e^{-\frac{(0.3933)2\pi z}{\lambda}}\right) \quad (1)$$

where the amplitude of the vertical ground motion A_z at depth z is a function of wavelength λ and z. The second analytical solution (dashed black lines in Fig. 3b) is the estimation of the Rayleigh wave penetration depth using various wavelength approximation (λ, λ/2, λ/3). For example, Hayashi (2008) and Kumagai et al. (2020) claim that surface wave penetration depth is down to a depth between *λ/4* and *λ/2*, whereas *λ/3* is often chosen to be the most suitable assumption (e.g., Larose, 2005). This approach is widely used to estimate the depth dependency of surface wave amplitudes in a homogeneous subsurface. The analytical solutions are generally based on the interplay of seismic velocity v, frequency f and wavelength λ:

$$\lambda = v/f \quad (2)$$

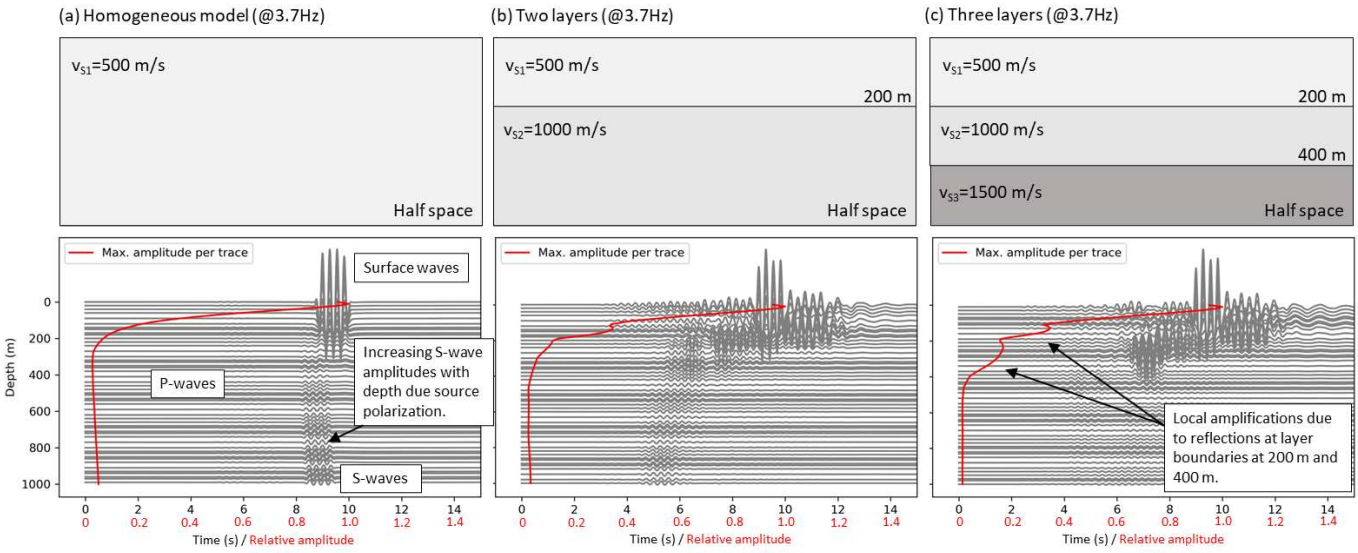

Figure 2: Example of the synthetic seismograms (gray lines) in dependency on the depth for signals at 3.7 Hz. The red line follows the maximum amplitude per trace and is affected by layers in the subsurface. It is normalized to the amplitude at the surface. P-, S-, and Rayleigh waves are simulated. The surface wave is dominating the wavefield near the surface.

https://doi.org/10.5194/egusphere-2023-45
Preprint. Discussion started: 7 February 2023

3 Results

3.1 Homogeneous models

The comparison between analytical and numerical solutions (Fig. 3) applied to a homogeneous half-space model shows very similar results for the amplitude-depth relations per frequency. This implies that on the one hand the numerical simulation reliably reproduced the analytical calculations. One the other hand, an analytical solution might be sufficient, if the subsurface is approximately homogeneous. The estimation of the Rayleigh wave penetration depth fits very well to the more

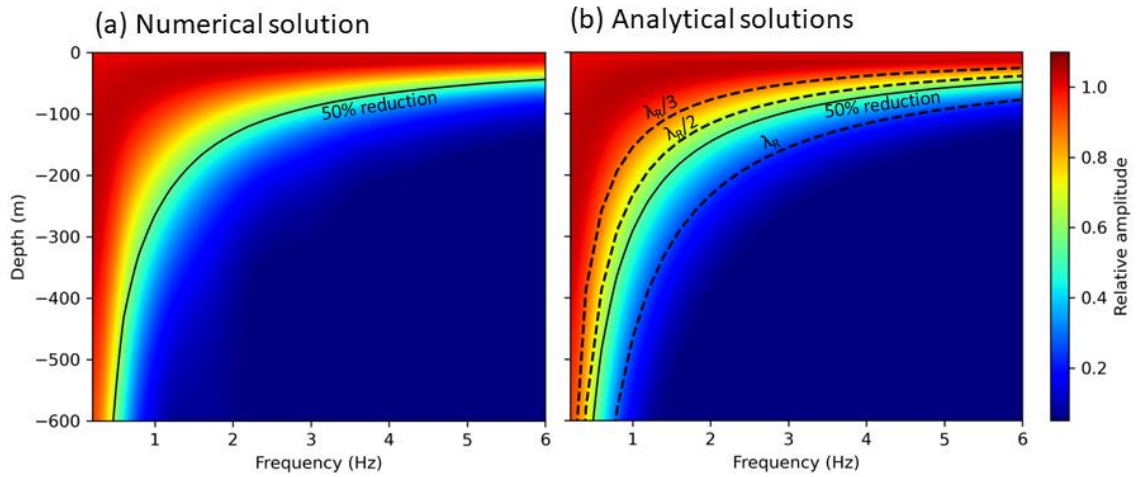

Figure 3: Benchmark - Comparison between numerical solutions and analytical solutions (λ - estimations, dashed lines) for homogeneous models, based on the formulation in Barkan (1962). The results are very similar which proves the reliability of the numerical solution for this simple benchmark.

complex analytical solution (Fig. 3b); however, the fraction of λ should be chosen, carefully considering the preferred reduction of noise with depth. These analytical solutions are limited regarding complex models of the subsurface.

Generally, a borehole should be deeper to yield a reduction of low frequency seismic noise (e.g., 1 Hz) compared to high frequencies (> 4 Hz). This is expectable, since the wavelength of a wave with a low frequency is larger compared to high frequencies. Consequently, the penetration depth of the surface wave is deeper. In view of eq. 2 the seismic velocity impacts this relation. The effects of the seismic velocity, signal frequency, layers in the subsurface, and attenuation on the depth-dependent amplitudes are simulated using homogeneous and layered models (Fig. 4). In case of high seismic velocities in the subsurface, deeper boreholes are required to yield a sufficient noise reduction. Furthermore, from the simulation results we obtain the effect of the signal frequency on the amplitudes. We find, for example, a borehole should be 100 m deep to reduce

https://doi.org/10.5194/egusphere-2023-45
Preprint. Discussion started: 7 February 2023

the noise of 3 Hz signals in 4 km distance to the WT by 50 %, if the velocity of the S-wave is 500 m s^{-1} (Fig. 4a), but the same borehole should be about 280 m deep for a velocity of 1500 m s^{-1} (Fig. 4c).

120

3.2 Layered models

In case of a layered subsurface, we find that the amplitude decay with depth is dominated by the top layer which (here) has a thickness of 200 m. The comparison between Fig. 4d and Fig. 4g shows that a third deep layer with a high velocity has no significant impact on the results. However, again, the estimation of sufficient borehole depths depends strongly on the seismic
125 velocity of the layers (especially the top layer). A borehole with a depth of 200 m seems to be sufficient if the S-wave velocity of the top layer is approximately 500 m s^{-1} (Fig. 4d), but this is not true if the velocity is increased (Fig. 4e,f). Signals > 4 Hz can by suppressed significantly in any case, but signals below this frequency (e.g., at 1 Hz) are not sufficiently affected by boreholes surrounded by rock with high seismic velocities. Hence, the geological setting and the seismic velocities play a key role concerning the evaluation of the effectivity of a borehole installation that aims to reduce the seismic noise produced by
130 WTs.

We further study the effect of attenuation (absorption) by specifying Q_S and Q_P. In model 8 (Fig. 4h), we used relatively high Q values (Q_S=100 and Q_P=200) (Eulenfeld and Wegler, 2016) for a weak attenuation (e.g., compact rock) and in model 9 (Fig. 4i) we used relatively low Q values (Q_S=30 and Q_P=60) to simulate a strong attenuation (e.g., near-surface sedimentary rocks). We find that the general amplitude-depth relation is not significantly affected by attenuation compared with the same model
135 without attenuation (model 4). There are some frequency-dependent effects (e.g., at 4 Hz) showing slightly increased amplitudes below the depth of 200 m in case of strong attenuation (*A* in Fig. 4i). This can be explained by a reduced contrast between the amplitude at the surface and the amplitude in depth. A strong attenuation causes generally lower amplitudes compared to a scenario without attenuation; however, the contrast between the amplitude in the borehole relative to the surface seems to be weakened.

140

https://doi.org/10.5194/egusphere-2023-45
Preprint. Discussion started: 7 February 2023

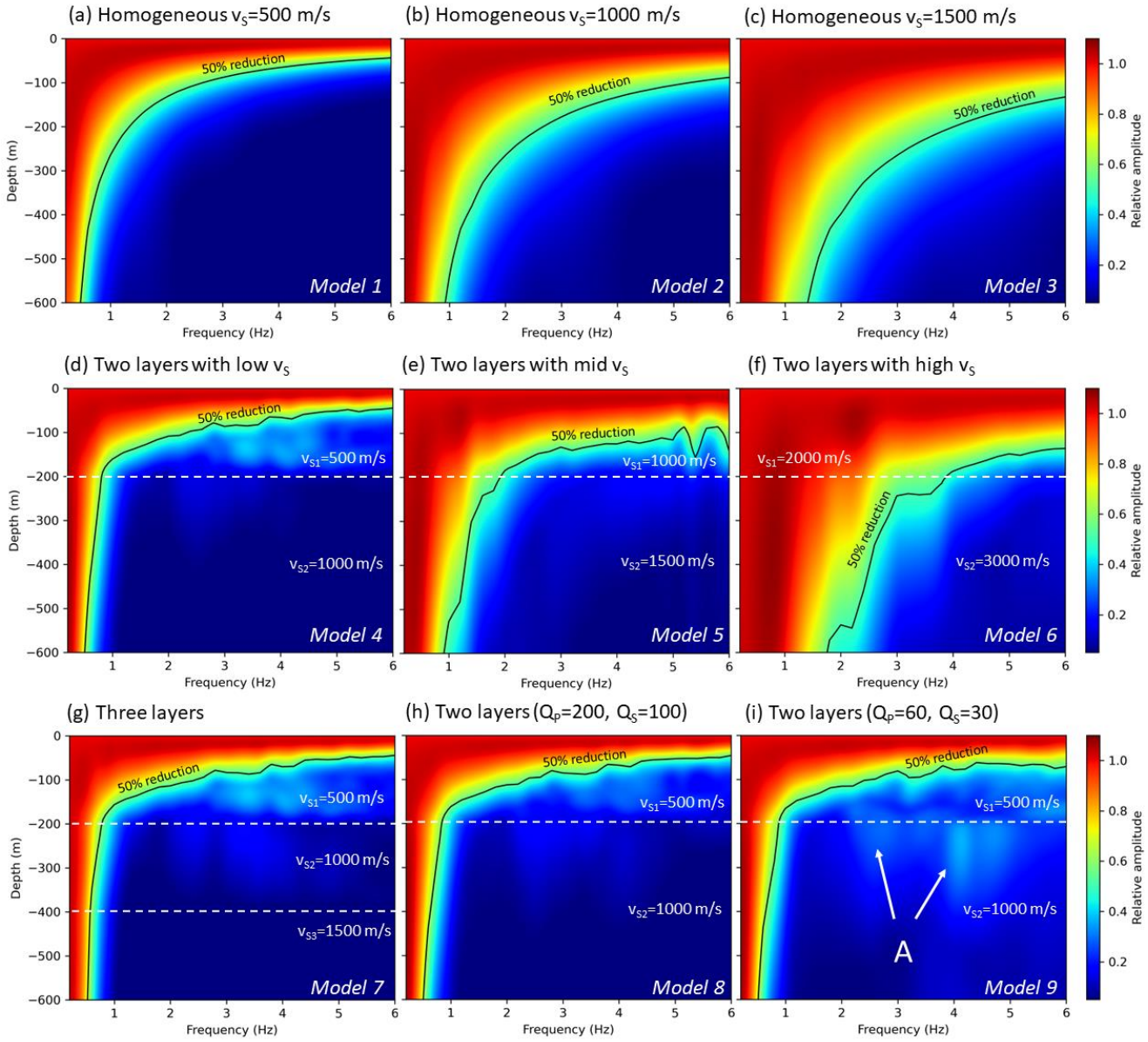

Figure 4: Effect of various models (a-c: homogeneous, d-g: layered, and h, i: with attenuation) on the frequency-dependent amplitude decrease with depth. The white dashed lines denote the layer boundaries. The solid black line indicates the amplitudes of 50 % reduction compared to the corresponding amplitude at the surface. The results are extracted from synthetic seismograms at 4 km distance from the source. Amplitudes as function of frequency are normalized to the corresponding amplitude at the surface.

3.3 Effect of distance between WT and seismic station

https://doi.org/10.5194/egusphere-2023-45
Preprint. Discussion started: 7 February 2023

The frequency-dependent amplitude decay with depth is generally affected by the distance between the WT and the borehole. To simulate these effects regarding the vertical and horizontal ground motion, we use model 4 (two layers with low velocities, see Table 1) and decrease the distance between the source and the receivers systematically from 4 km to 1 km. The results are presented in Fig. 5. With decreasing distance between the source and the borehole, amplitudes increase at frequencies between 2 Hz and 4 Hz up to a depth of 200 m, especially regarding the horizontal component in x-direction of the model. This indicates relatively strong effects at the base of the topmost layer in 200 m depth, likely due to strong reflection concerning the specific frequencies. These effects might change in case of higher velocities, change of frequency or thickness of the top layer. Furthermore, we observe that the amplitude of the horizontal component is decreasing much faster with depth compared to the vertical component. This behaviour can be described analytically (Barkan, 1962). However, layers in the subsurface can have an adverse effect for specific frequencies, as described. The layer boundary in 200 m depth seems to isolate the amplitudes above and below. This means that a borehole could be very effective at depths > 200 m, at least for this specific case.

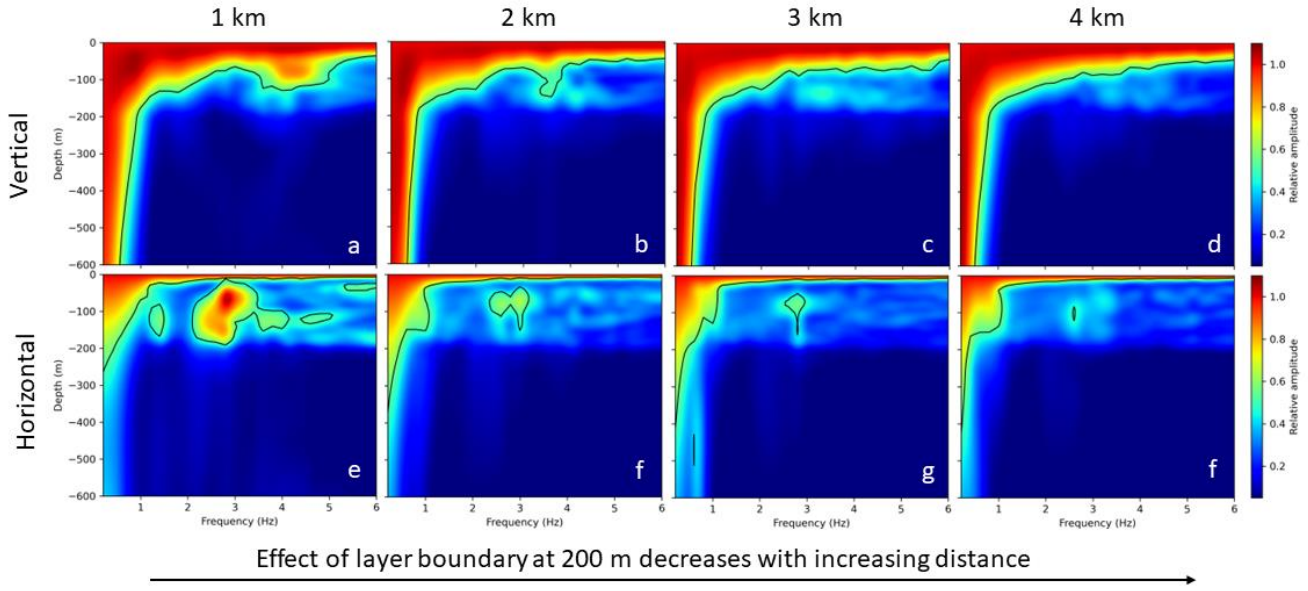

Figure 5: Effect of distance between source and borehole on vertical (z-axis) and horizontal (x-axis) seismogram components. Model 4 is used for these simulations. The distance has an effect on the amplitudes with depth, especially regarding the horizontal components. The layer boundary in 200 m depth is isolating the amplitudes above and below this layer. Amplitudes as functions of frequency are normalized to the corresponding amplitude at the surface.

https://doi.org/10.5194/egusphere-2023-45
Preprint. Discussion started: 7 February 2023

3.4 Effects of attenuation

To investigate the effect of attenuation on the effectivity of a borehole for a specific frequency, we use model 4 including weak and strong attenuation. In this case, we study signals of 3.7 Hz (which is a typical frequency emitted by WTs) and calculated the seismic radiation in the x-z-plane and compare the results to those for the model without attenuation. As expected, we find that a strong attenuation affects the general amplitude decay with distance to the source and with depth (Fig. 6a, 6c, 6e). However, the relative amplitudes between depth and surface are only slightly affected by attenuation. This becomes obvious by looking at the almost identical results when the amplitudes in the depth are normalized to the corresponding amplitude at the surface (Fig. 6b, 6d, 6f). The tendency is that the contrast of amplitudes at the surface compared to amplitudes in depth is lower when strong attenuation exists (Fig. 6f). This implies that a borehole in a strongly attenuating environment might not be as effective as in less attenuating rock. However, the attenuation is not the dominating parameter to evaluate the effectivity of the borehole installation, as shown before. It should be noted that the undulation in x-direction is due to the layering (reflection effects).

With this analysis we can evaluate the distance of a seismometer to the WT. In view of Fig. 6c, we show that the distance between seismometer and WT could be reduced from 4 km to 2 km, if the seismometer is placed in a 100 m deep borehole, thus avoiding a significant increase of the noise level. But it should be clear that this is only an estimation for the specific case in this study and is very likely affected by changes of seismic velocity and the structure of the subsurface.

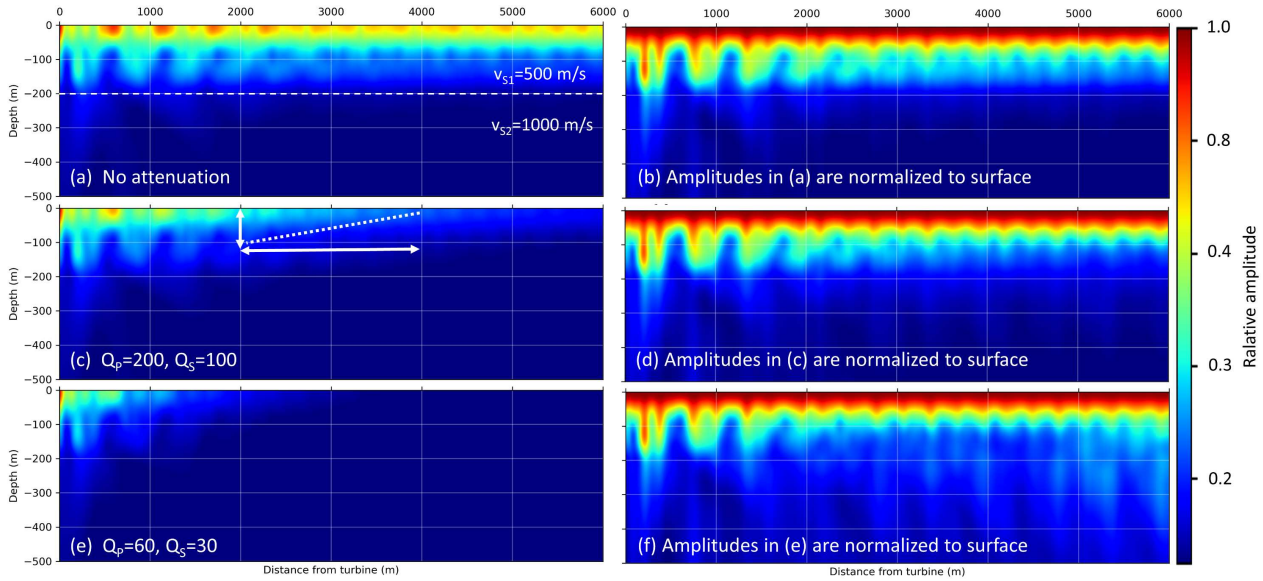

Figure 6: Left panel (a,c,e): Effect of attenuation on amplitude decays, normalized to source amplitude. Right panel (b,d,f): Amplitudes are normalized column wise, which means at each distance in x-direction, the amplitude with depth is normalized to the corresponding amplitude at the surface. The dominant signal frequency in these simulations is 3.7 Hz.

https://doi.org/10.5194/egusphere-2023-45
Preprint. Discussion started: 7 February 2023

3.5 Real data validation

In this section, we validate the presented approach with data from seismic borehole installations. Close to the city of Landau in the upper Rhine valley, two seismic borehole stations with a depth of 305 m (station ROTT) and 150 m (station LDE) are located at distances of approximately 5.5 km (ROTT) and 3.8 km (LDE), respectively, to the next WTs (Fig. 7). These permanent stations are part of the earthquake monitoring system of the geological survey in Rhineland-Palatinate, Germany. Zieger and Ritter (2018) temporarily measured the frequency-dependent noise of the nearby WTs at the surface of the corresponding borehole locations and calculated power spectral densities (PSD) (Fig. S3 in supplements). They showed a clear reduction of measured noise due to the boreholes. We took the PSD values of Zieger and Ritter (2018) and transformed the data into relative ground motions. At frequencies of 1 Hz we find an amplitude reduction of 73 % at the borehole station ROTT. At LDE we observe a reduction of 34 % for 1 Hz signals and 71 % for 3.7 Hz signals by comparing the amplitudes of the borehole seismometer with the surface amplitudes (Fig. S3 in supplements). The signals with 3.7 Hz are not reliably observable at ROTT and are therefore not included in the further analysis. These factors of amplitude reduction are used as a reference for numerical results in our study. A numerical model (Fig. 8a) is built using subsurface information derived from the MAGS2 project (Fig. S2 in supplements) (Spies et al., 2017), which provides detailed seismic velocities and is hence one of the most accurate velocity models of the Landau region. The model of the local subsurface contains relatively low seismic velocities due to the younger sediments in the upper Rhine valley. The model we extracted has four layers with increasing S-wave velocity from 450 m s^{-1} (top layer), 750 m s^{-1} (second layer), 900 m s^{-1} (third layer) to 1150 m s^{-1} (half space). Again, the density is fixed to 2600 kg m^{-3} and the P-wave velocity is 1.7 times V_S. The synthetic boreholes in the numerical models are correspondingly located at distances of 3.8 km (LDE) and 5.5 km (ROTT), respectively, to the source point. From the

https://doi.org/10.5194/egusphere-2023-45
Preprint. Discussion started: 7 February 2023

simulations (Fig. 8b and c), we can calculate the spectral isoline of an amplitude reduction of 73 % (ROTT) and the isoline of 71 % and 34 % (LDE) for all frequencies between 0.2 Hz and 6 Hz. Based on the model of the subsurface a comparison of the numerical results with the observed data from Zieger and Ritter (2018) shows a good agreement and thus validates our amplitude estimations. The model is characterized by a first significant layer boundary at 200 m depth where the S-wave

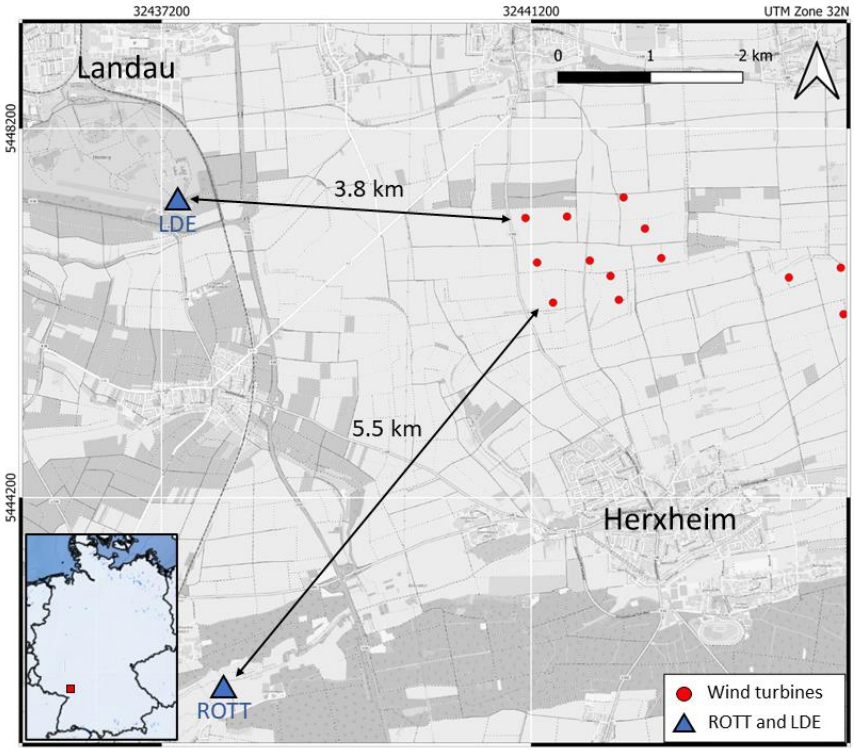

Figure 7: Map of the Landau region with borehole stations ROTT and LDE and the nearest wind farm north of Herxheim. Zieger & Ritter (2018) deployed two seismic stations at top of the boreholes to compare signal amplitudes measured at the surface with amplitudes measured at the borehole stations. (Maps: © OpenStreetMap contributors 2023. Distributed under the Open Data Commons Open Database License (ODbL) v1.0)

velocity increases from 450 m s^{-1} to 750 m s^{-1}. Interestingly, this layer boundary significantly affects the amplitude decrease with depth, especially regarding signals with a frequency between 2 Hz and 4 Hz. This effect is likely due to reflections of the waves that are mainly traveling along the top layer. Considering these effects, the observed amplitude reduction by 71 % of the 3.7 Hz signals can only be reproduced numerically by the layered model and would fail for a homogenous model. The observed reduction by 34 % of the 1 Hz signals at borehole station LDE is also accurately described by our modelling. The reduction by 73 % of the 1 Hz signals at ROTT is simulated appropriately. However, there is a discrepancy between observed and simulated amplitude reductions at a depth of 305 m (ROTT). In this frequency range (around 1 Hz), the amplitude decay with depth is very sensitive and thus challenging to be perfectly fitted.

https://doi.org/10.5194/egusphere-2023-45
Preprint. Discussion started: 7 February 2023

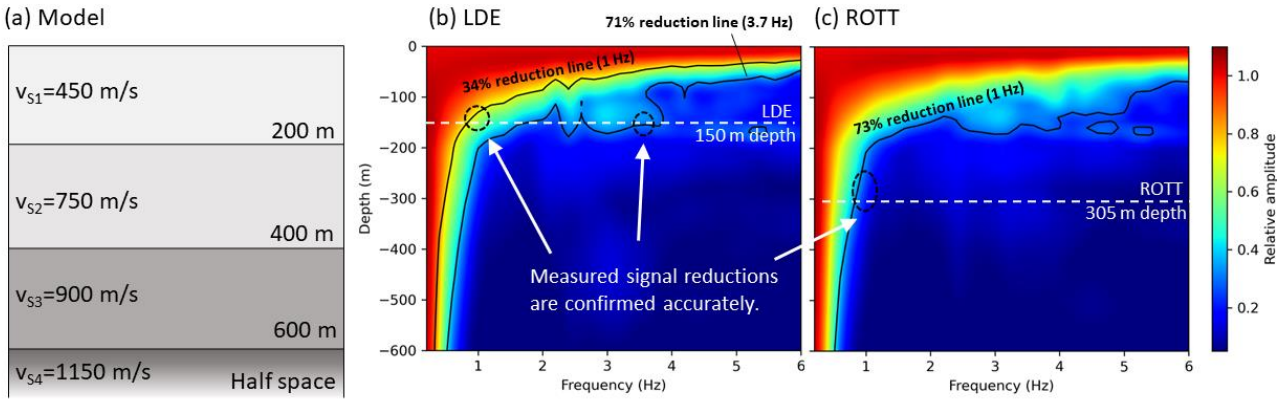

Figure 8: a) A model with three layers above a half space is used for the real data validation. The model is based on information provided by the MAGS2 project (Spies et al., 2017). The results of the simulations are compared to observations made by Zieger and Ritter (2018) and show good agreement, this means that the reduction of noise amplitudes can be reliably estimated using 2D numerical simulations.

4 Discussion and conclusions

In this work, we study the effectivity of borehole installations to reduce the impact of seismic noise produced by WTs on seismological recordings. Based on numerical models, the effect of geophysical parameters, such as seismic velocities and attenuation, and layering of the subsurface are simulated to constrain the depth of seismic borehole stations, to significantly reduce the noise produced by WTs?

We validate our approach by comparisons with existing real data published by Zieger and Ritter (2018). We can reproduce the observed reduction factors by Zieger and Ritter (2018) of signal amplitudes at specific frequencies measured at the surface and in depth at two boreholes close to Landau in Rhineland-Palatinate, Germany (Fig. 8). We point out that this validation is based on simulations using a realistic model of the subsurface which consists of three layers above a half space (based on results given in Spies et al., 2017). Interestingly, we would not be able to explain some of the observations, if the layer boundary at 200 m would not be included in the model. This indicates that simplified analytical solutions (homogeneous half-space model) fail to simulate the wavefield sufficiently. To increase the reliability and to enable a wider application of the method, further borehole data, covering a broad range of frequencies, is necessary and should be studied in the future. Our real data validation is performed for the upper Rhine valley which is characterized by thick relatively young sediments with low seismic

https://doi.org/10.5194/egusphere-2023-45
Preprint. Discussion started: 7 February 2023

velocities (Fig. 8a). Similar simulations could be performed for other geological settings characterized by more compact rock types.

The numerical modelling shows that the effectivity of such boreholes to reduce surface generated seismic noise strongly depends on the interplay of signal frequency, seismic velocity and the wavelength (Fig. 4). Low-frequency signals and high seismic velocities yield a large wavelength, which results in a penetration depth of > 600 m for the most prominent surface waves. In regions with soft sediments, boreholes of a few hundred meters depth are likely effective to reduce the noise from WTs, especially in view of the high-frequency signals. A borehole of only 200 m to 300 m depth can reduce the noise of signals between 2 Hz and 6 Hz by more than 50 %. However, boreholes might not be effective in other regions where more compact rock types and relatively high seismic velocities dominate. The typical frequency range of signals produced by WTs is between 1 Hz and 10 Hz. The reduction of signals with frequencies around 1 Hz seems challenging, due to the relatively large wavelength. These waves travel generally very far in distance and depth. Nevertheless, Zieger and Ritter (2018) demonstrated the reduction of such signals by 73% in a borehole of 305 m depth (5 km to the next WF) and 34 % in case of 150 m depth (3.8 km to the next WF). We confirmed these observations with our modelling (Fig. 8).

The comparison of results for homogeneous models and layered models shows that the amplitude-depth relation is dominated by the top layer, but this depends again on the general wavelength of the surface waves and the thickness of the top layer (Fig. 4). We studied these effects for a top layer of 200 m thickness, which is characteristic for the Upper Rhine valley. The effects of various thicknesses and lateral heterogeneities (such as fault structures or site effects) could be part of future modelling studies.

We further show that borehole installations in geological environments with strong attenuation might not be effective as in environments with weak attenuation. Attenuation reduces the amplitude with distance in general, but it does not affect the relative amplitudes at the surface and in depth significantly (Fig. 6).

We show that the effects of the layer boundary at 200 m depth on the wavefield increases with decreasing distance to the source, especially regarding the horizontal components of the signal (Fig. 5). In our simulations we apply vertically polarized source mechanisms to model the signals from the WTs. This is an approximation to the up and down movement of the foundation of the WT. However, other source mechanisms and polarizations might have additional effects on the wave propagation and should be part of future research. A time-limited wave package is a sufficient approximation of the source signal and a practical solution to numerically simulate effects of the subsurface on the wave propagation. However, WTs usually emit continuous signals which might lead to additional complex wave reflections and interferences in the subsurface. Further signal modulation can also occur by wavefield interferences from multiple WTs, as shown by Limberger et al. (2022).

A key aspect in evaluating the effectivity of a borehole is the general purpose of a specific seismic station. If a station is used for the detection and localization of local earthquakes with a relatively high frequency content (e.g., higher than 5 Hz), a borehole can be very effective to reduce the noise from WTs nearby. However, if the seismometer is used to measure signals with lower frequencies (e.g., 1 Hz in case of teleseismic signals), then borehole installations might fail in reducing the noise, or the necessary borehole would require a depth that is too large to be feasible. In view of our results, we strongly recommend

https://doi.org/10.5194/egusphere-2023-45
Preprint. Discussion started: 7 February 2023

to perform estimations based on the specific characteristics of the location of interest and not to generalize and apply one estimation for all locations and seismic stations. However, besides WTs, our approach can be also applied to other anthropogenic noise sources (e.g., in urban areas) and enables a universal assessment of seismic noise and its effect on borehole installations.

To conclude, the impact of seismic noise produced by WTs on seismometers can be decreased if the seismic sensor is installed within a borehole at an adequate depth. But this strongly depends on various geophysical and geological parameters, such as seismic velocities or layering in the subsurface, and should be carefully evaluated for every geological environment separately. With this study, we provide a robust approach to perform reliable estimations of the effectivity of borehole installations.

Code and data availability. The numerical simulations were performed using the commercial software package Salvus (Afanasiev, 2018). The simulation scripts are available from the corresponding author (limberger@igem-energie.de) on request. The data processing was performed using the Python packages NumPy and SciPy.

Author Contributions. All authors developed the thematic idea of the study. F.L. performed the numerical simulations and processed the data. G.R. participated in developing the model, and supervised the writing of the article. F.L., M.L., and G.R. interpreted the results. F.L., G.R., M.L. and H.D. each edited the article.

Competing Interests Statement. The authors declare no competing interests.

Acknowledgements. We thank the German Federal Ministry for Economic Affairs and Climate Action (FKZ no. 0324360) and ESWE Innovations und Klimaschutzfonds for their support in performing this study.

References

Abreu, R., Peter, D., and Thomas, C.: Reduction of wind-turbine-generated seismic noise with structural measures. *Wind Energy Science*, *7*, 1227–1239, 2022

Afanasiev, M., Boehm, C., van Driel, M., Krischer, L., Rietmann, M., May, D. A., et al.: Modular and flexible spectral-element waveform modelling in two and three dimensions. *Geophysical Journal International*, *216*, 1675–1692, doi:10.1093/gji/ggy469, 2018

https://doi.org/10.5194/egusphere-2023-45
Preprint. Discussion started: 7 February 2023

Barkan, D. D.: *Dynamics of bases and foundations*. McGraw-Hill, page 325, 1962

Boese, C. M., Wotherspoon, L., Alvarez, M., and Malin, P.: Analysis of Anthropogenic and Natural Noise from Multilevel Borehole Seismometers in an Urban Environment, Auckland, New Zealand. *Bulletin of the Seismological Society of America*, *105*, 285–299, doi:10.1785/0120130288, 2015

Colombi, A., Roux, P., Guenneau, S., Gueguen, P., and Craster, R. V.: Forests as a natural seismic metamaterial: Rayleigh wave bandgaps induced by local resonances. *Scientific Reports*, *6*, doi:10.1038/srep19238, 2016

Eulenfeld T. and Wegler U.: Measurement of intrinsic and scattering attenuation of shear waves in two sedimentary basins and comparison to crystalline sites in Germany, *Geophysical Journal International*, 205, 744–757, 2016

Gaßner, L., and Ritter, J.: Ground motion emissions due to wind turbines: observations, acoustic coupling, and attenuation relationships. *EGUsphere*, *2022*, 1–25, doi:10.5194/egusphere-2022-108, 2022

Gortsas, T. V., Triantafyllidis, T., Chrisopoulos, S., and Polyzos, D.: Numerical modelling of micro-seismic and infrasound noise radiated by a wind turbine. *Soil Dynamics and Earthquake Engineering*, *99*, 108–123, doi:10.1016/j.soildyn.2017.05.001, 2017

Hayashi, K.: Development of the Surface-wave Methods and Its Application to Site Investigations, PhD thesis, Kyoto University, Japan, 2008

Heuel, J., and Friederich, W.: Suppression of wind turbine noise from seismological data using nonlinear thresholding and denoising autoencoder. *Journal of Seismology*, *26*, 913–934, doi:10.1007/s10950-022-10097-6, 2022

Kumagai, T., Yanagibashi, T., Tsutsumi, A., Konishi, C., and Ueno, K.: Efficient surface wave method for investigation of the seabed, *Soils Found.*, 60, 648–667, 2020

Larose, E.: Lunar subsurface investigated from correlation of seismic noise, *Geophysical Research Letters.,* 32, L16201, 2005

https://doi.org/10.5194/egusphere-2023-45
Preprint. Discussion started: 7 February 2023

Lerbs, N., Zieger, T., Ritter, J., and Korn, M.: Wind turbine induced seismic signals: the large-scale SMARTIE1 experiment and a concept to define protection radii for recording stations. *Near Surface Geophysics*, *18*, 467–482, doi:10.1002/nsg.12109, 2020

Limberger, F., Lindenfeld, M., Deckert, H., and Rümpker, G.: Seismic radiation from wind turbines: observations and analytical modeling of frequency-dependent amplitude decays. *Solid Earth*, *12*, 1851–1864, doi:10.5194/se-12-1851-2021, 2021

Limberger, F., Rümpker, G., Lindenfeld, M., and Deckert, H.: Development of a numerical modelling method to predict the seismic signals generated by wind farms. *Scientific Reports*, *12*, doi:10.21203/rs.3.rs-1621492/v1, 2022

Malin, P. E., Bohnhoff, M., Blümle, F., Dresen, G., Martínez-Garzón, P., Nurlu, M., et al.: Microearthquakes preceding a M4.2 Earthquake Offshore Istanbul. *Scientific Reports*, *8*, doi:10.1038/s41598-018-34563-9, 2018

Neuffer, T., and Kremers, S.: How wind turbines affect the performance of seismic monitoring stations and networks. *Geophysical Journal International*, *211*, 1319–1327, doi:10.1093/gji/ggx370, 2017

Saccorotti, G., Piccinini, D., Cauchie, L., and Fiori, I.: Seismic Noise by Wind Farms: A Case Study from the Virgo Gravitational Wave Observatory, Italy. *Bulletin of the Seismological Society of America*, *101*, 568–578, doi:10.1785/0120100203, 2011

Spies, T., Schlittenhardt, J., and Schmidt, B.: *Abschlussbericht für das Verbundprojekt MAGS2: Mikroseismische Aktivität geothermischer Systeme 2 (MAGS2) - Vom Einzelsystem zur großräumigen Nutzung*. Bundesanstalt für Geowissenschaften und Rohstoffe, 2017

Stammler, K., and Ceranna, L.: Influence of Wind Turbines on Seismic Records of the Gräfenberg Array. *Seismological Research Letters*, *87*, 1075–1081, doi:10.1785/0220160049, 2016

Withers, M. M., Aster, R. C., Young, C. J., and Chael, E. P.: High-frequency analysis of seismic background noise as a function of wind speed and shallow depth. *Bulletin of the Seismological Society of America*, *86*, 1507–1515, doi:10.1785/bssa0860051507, 1996

https://doi.org/10.5194/egusphere-2023-45
Preprint. Discussion started: 7 February 2023

Zieger, T., and Ritter, J. R. R.: Influence of wind turbines on seismic stations in the upper rhine graben, SW Germany. *Journal of Seismology*, *22*, 105–122, doi:10.1007/s10950-017-9694-9, 2018

Zieger, T., Nagel, S., Lutzmann, P., Kaufmann, I., Ritter, J., Ummenhofer, T., et al.: Simultaneous identification of wind turbine vibrations by using seismic data, elastic modeling and laser Doppler vibrometry. *Wind Energy*, *23*, 1145–1153, doi:10.1002/we.2479, 2020

6. Conclusion and outlook

The results of this thesis increase the understanding and capability to predict seismic waves that are produced by wind farms. The extensive experimental and numerical analysis performed in this research reveal the complexity of wavefields emitted by a complete wind farm while also developing solutions to efficiently model and investigate the emitted wavefields. The knowledge about the characteristic signals from wind turbines measured with seismometers has increased in recent years. However, robust approaches to simulate these signals that incorporate various effects, such as from the sources (e.g., multiple wind turbines) and travel path effects (e.g., topography), have been insufficient. As such, this work presents the experimental analysis of long-term measurements conducted at wind farms and advances the modeling such signals, which furthermore has a high potential of universal application to wind farms with arbitrary layout and geographic location.

6.1 Summary and conclusion

In this chapter the key questions that were formulated in Chapter 1 are answered in order to summarize the findings and results gained from the papers presented in this work.

1. Is it possible to reliably quantify the amplitude decay of seismic signals with distance from a wind farm and to model the seismic radiation from a complete wind farm including the wavefields produced by multiple wind turbines?

In Chapter 3, long-term measurements (about 6 months) along a 4 km profile with 14 seismometers were performed and analyzed for signals from the small wind farm in Uettingen (close to Würzburg, Germany). From average PSDs, seven discrete frequency peaks between 1 Hz and 8 Hz can be clearly assigned to the operation of the wind turbines. Statistically robust amplitude decays with distance showed an almost perfect linear relation between damping factors (*b*-values) and signal frequency. Additional measurements at the base of the three wind turbines revealed no correlation between the vibrations of the single wind turbines. This implies that they vibrate independent of each other. It was shown that the interference of the wavefields that are produced by the multiple wind turbines is temporally rather random and non-systematic, which in turn means that the waves can interfere destructively and constructively depending on location and time. As a solution, this thesis featured a method to calculate a representative seismic radiation pattern of surface waves produced by a wind farm. The method proposes to average many radiation patterns that are calculated with random signal phases of the sources, whereby the resulting radiation covers many possible constellations of interfering wavefields and is not dominated by one specific interference. By applying this method to the wind farm in Uettingen, including velocity and damping parameters of the subsurface, an accurate simulation of the observed frequency-dependent amplitude decays was possible. The

performed grid-search to find the best model parameters revealed that a two-layer model is more sufficient to enhance the simulation results, compared to a homogenous model.
Based on the findings in this study, it is recommendable to collect several months of data to derive robust amplitude decays and information about the wave attenuation. Furthermore, it should not be assumed that wind turbines vibrate in phase (e.g., up and down at the same time), since a specific interference has significant effects on the seismic radiation from a wind farm. As such, the developed method enables a generalized prediction of noise amplitudes in the far field of a complete wind farm with an arbitrary layout if the local subsurface and topography is relatively uncomplex.

2. Are there significant effects of wavefield interferences, the local topography, and the wave attenuation on the seismic signals in respect to distance?

The method developed in Chapter 3 was extended in Chapter 4 using advanced three-dimensional models to simulate the propagation of complete wavefields from multiple wind turbines based on SEM. The aim of Chapter 4 was the simulation of signals that are produced by the Weilrod wind farm (north of Frankfurt am Main, Germany), which are detectable at the seismological observatory TNS (Taunus), which is in a distance of 11 km from the wind farm. TNS is characterized by a very low noise level, which is one reason why a doubling of the noise level, due to the operation of the wind farm, at 1.15 Hz is measurable. The Taunus region is characterized by a pronounced topography, which was included in the 3D model using a digital elevation model. Besides the significant effects from the multiple sources causing constructive and destructive interferences (as shown in Chapters 3 and 4), the topography causes amplitude reductions, due to scattering of the waves, as well as amplifications of the signal, especially concerning low-frequency signals. The comparison of simulations with and without topography revealed that the reduction and amplification are spatially linked to the shape of the topography. It was indicated that the amplitude of the waves produced by the wind turbines is preserved along mountain ridges and increased at the mountainsides that face away from the sources. Hence, this observation could be an explanation for the relatively high signal amplitude at TNS. Including intrinsic attenuation, the modeling results were validated by the measurements at the seismological observatory TNS and in the near field of the wind farm. The application of the modeling on the Weilrod wind farm revealed that topography should not be neglected in the model, especially if it is pronounced. Valleys and mountains might cause scattering but also focusing effects on the waves propagating along the surface and can even amplify the signal measured at a distant seismometer. Suitable parameters of the local subsurface (such as velocity and attenuation) are crucial to achieve reliable modeling results.
For the first time, the complicated aspects of modeling a whole wind farm as a seismic source, the effects of local topography, and attenuation with distance have been incorporated within one model. Furthermore, the presented modeling approach has the potential to be applied for noise amplitude predictions prior to the installation of a new wind farm.

3. Is a borehole installation effective to reduce the impact of wind turbines on seismic measurements, and if so, what are the necessary criteria?

In Chapter 5**,** the reduction of the impact of wind turbines on seismic measurements using borehole installations was studied using 2D numerical models based on SEM. Depth-dependent amplitudes up to a depth of 600 m were simulated including frequencies typically emitted by wind turbines. Possible effects of the seismic velocity, attenuation, and layering of the subsurface were demonstrated. The parameter study revealed that the effectivity of borehole installations near a wind turbine strongly depends on the wavelength of the incoming waves and is hence frequency dependent. A borehole with a depth of 200 m can be very effective regarding high frequencies (e.g., 6 Hz), especially in areas with low seismic velocities, such as the Rhine Valley, Germany. However, a borehole might not be beneficial if signals with frequencies of about 1 Hz (or lower) are of interest (e.g., teleseimic events), due to a large wavelength and thus a deep penetration of the surface waves. Layering in the subsurface can have significant effects on the general wavefield produced by a wind turbine, due to reflections at layer boundaries. It has been shown that a top layer of 200 m thickness isolates the waves from reaching deeper layers, which can promote the installation of a borehole seismometer beneath the top layer. Nevertheless, this effect depends on the thickness of the top layer and the wavelength. The estimations of depth-dependent amplitudes with a layered subsurface are validated with wind-turbine-induced signals measured at the top and bottom of two boreholes with 150 m and 305 m depths. The validation reliably demonstrates that 2D models are suitable to study the potential of borehole installations near wind turbines.
This chapter provided information and a generalized method to perform estimations on the effectivity of a borehole to reduce the impact of wind turbines on seismic stations. This has the potential to improve the general assessment after or prior to the installations of wind farms near a seismic station with the aim to prevent the station from experiencing a drastic increase in noise level.

6.2 Outlook

Within the framework of this thesis, improvements to analyze, model, and predict seismic signals produced by wind farms have been provided to better understand effects of wavefield interferences, topography, and wave attenuation with distance and depth. Nevertheless, further development is suggested. The proposed methods might be extended by testing various source polarizations (e.g., dipole mechanisms), to account for the various patterns of motion of the wind turbine foundation. It would be of interest to study effects of the various source mechanisms on the interferences, and hence, the general prediction of the signal amplitude. Furthermore, the effects of more complex structures in the subsurface, such as faults or graben structures, are of interest since there could be an additional influence on the wave propagation and amplitude in the far field of a wind farm. Seismic waves can be strongly damped by large damaging zones with relatively fractured rock in the subsurface. Such zones between a wind farm and a seismometer could be of advantage to reach a high wave damping along the travel path. In contrast to this, site effects could result in local amplitude amplifications. The characterization of wind-turbine-induced waves with seismic array technologies might be a huge benefit, due to the opportunity to analyze the incoming waves in more detail. So far, the seismic waves were analyzed using single stations, or profile measurements, but not by specifically arranged arrays in the far field of the wind farm, which should be tested in the future. Finally, further validations with broad data from various wind turbines, boreholes with seismometers, and geographic locations with different geological conditions would help to increase the universal capability of the findings and methods developed in this thesis.

Bibliography

Abreu, R., Peter, D., & Thomas, C. (2022). Reduction of wind-turbine-generated seismic noise with structural measures. *Wind Energy Science, 7*, 1227–1239. doi:10.5194/wes-7-1227-2022

Afanasiev, M., Boehm, C., van Driel, M., Krischer, L., & Fichtner, A. (2018). Flexible high-performance multiphysics waveform modeling on unstructured spectral-element meshes. In *SEG Technical Program Expanded Abstracts 2018*. Society of Exploration Geophysicists.

Afanasiev, M., Boehm, C., van Driel, M., Krischer, L., Rietmann, M., May, D. A., Knepley, M. G., and Fichtner, A. (2019). Modular and flexible spectral-element waveform modelling in two and three dimensions. *Geophysical Journal International, 216*, 1675–1692. doi:10.1093/gji/ggy469

Aki, K., & Richards, P. (1980). *Quantitative seismology.* W. H. Freeman and Company, New York.

Barkan, D. D. (1962). *Dynamics of bases and foundations.* McGraw-Hill.

Best, A. I., Sothcott, J., & McCann, C. (2007). A laboratory study of seismic velocity and attenuation anisotropy in near-surface sedimentary rocks. *Geophysical Prospecting, 55*, 609–625. doi:10.1111/j.1365-2478.2007.00642.x

Boese, C. M., Wotherspoon, L., Alvarez, M., & Malin, P. (2015). Analysis of Anthropogenic and Natural Noise from Multilevel Borehole Seismometers in an Urban Environment, Auckland, New Zealand. *Bulletin of the Seismological Society of America, 105*, 285–299. doi:10.1785/0120130288

Bugeja, R. (2011). *Crustal Attenuation in the region of the Maltese Islands using Coda Wave Decay.* Ph.D. dissertation, Department of Physics, University of Malta.

Chandler, A. M., Lam, N. T., & Tsang, H. H. (2006). Near-surface attenuation modelling based on rock shear-wave velocity profile. *Soil Dynamics and Earthquake Engineering, 26*, 1004–1014. doi:10.1016/j.soildyn.2006.02.010

Clauser, C. (2016). *Einführung in die Geophysik.* Springer Berlin Heidelberg. doi:10.1007/978-3-662-46884-5

Clayton, R., & Engquist, B. (1977). Absorbing boundary conditions for acoustic and elastic wave equations. *Bulletin of the Seismological Society of America*, *67*, 1529–1540.

Colombi, A., Roux, P., Guenneau, S., Gueguen, P., & Craster, R. V. (2016). Forests as a natural seismic metamaterial: Rayleigh wave bandgaps induced by local resonances. *Scientific Reports, 6*. doi:10.1038/srep19238

Courant, R., K. Friedrichs, *and* H. Lewy *(*1967*),* On the partial difference equations of mathematical physics*, IBM J. Res. Develop.,* 11*,* 215–234*, doi:*10.1147/rd.112.0215.

Estrella, H. F., Korn, M., & Alberts, K. (2017). Analysis of the Influence of Wind Turbine Noise on Seismic Recordings at Two Wind Parks in Germany. *Journal of Geoscience and Environment Protection, 05*, 76–91. doi:10.4236/gep.2017.55006

Eulenfeld, T., & Wegler, U. (2016). Measurement of intrinsic and scattering attenuation of shear waves in two sedimentary basins and comparison to crystalline sites in Germany. *Geophysical Journal International, 205*, 744–757. doi:10.1093/gji/ggw035

Farrugia, D., Paolucci, E., D'Amico, S., Galea, P., Pace, S., Panzera, F., & Lombardo, G. (2015). Evaluation of seismic site response in the Maltese archipelago. *Geophysical Aspects*.

Friedrich, T., Zieger, T., Forbriger, T., & Ritter, J. R. (2018). Locating wind farms by seismic interferometry and migration. *Journal of Seismology, 22*, 1469–1483. doi:10.1007/s10950-018-9779-0

Gaßner, L., & Ritter, J. (2022). Ground motion emissions due to wind turbines: observations, acoustic coupling, and attenuation relationships. *EGUsphere, 2022*, 1–25. doi:10.5194/egusphere-2022-108

Gortsas, T. V., Triantafyllidis, T., Chrisopoulos, S., & Polyzos, D. (2017). Numerical modelling of micro-seismic and infrasound noise radiated by a wind turbine. *Soil Dynamics and Earthquake Engineering, 99*, 108–123. doi:10.1016/j.soildyn.2017.05.001

Hayashi, K. (2008). *Development of the Surface-wave Methods and Its Application to Site Investigations.* Ph.D. dissertation, Kyoto University.

Heuel, J., & Friederich, W. (2022). Suppression of wind turbine noise from seismological data using nonlinear thresholding and denoising autoencoder. *Journal of Seismology, 26*, pages 913–934. doi:10.1007/s10950-022-10097-6

Hu, W., Barthelmie, R. J., Letson, F., & Pryor, S. C. (2019). Seismic Noise Induced by Wind Turbine Operation and Wind Gusts. *Seismological Research Letters, 91*, 427–437. doi:10.1785/0220190095

Karatzetzou, A., Negulescu, C., Manakou, M., François, B., Seyedi, D. M., Pitilakis, D., & Pitilakis, K. (2014). Ambient vibration measurements on monuments in the Medieval City of Rhodes, Greece. *Bulletin of Earthquake Engineering, 13*, 331–345. doi:10.1007/s10518-014-9649-2

Komatitsch, D., & Tromp, J. (1999). Introduction to the spectral element method for three-dimensional seismic wave propagation. *Geophysical Journal International*, 139, 806–822. doi:10.1046/j.1365-246x.1999.00967.x

Komatitsch, D., Barnes, C., & Tromp, J. (2000). Wave propagation near a fluid-solid interface: A spectral-element approach. *GEOPHYSICS*, *65*, 623–631.

Komatitsch, D., Ritsema, J., & Tromp, J. (2002). The Spectral-Element Method, Beowulf Computing, and Global Seismology. *Science*, 298, 1737–1742. doi:10.1126/science.1076024

Kumagai, T., Yanagibashi, T., Tsutsumi, A., Konishi, C., & Ueno, K. (2020). Efficient surface wave method for investigation of the seabed. *Soils and Foundations, 60*, 648–667. doi:10.1016/j.sandf.2020.04.005

Larose, E. (2005). Lunar subsurface investigated from correlation of seismic noise. *Geophysical Research Letters, 32*. doi:10.1029/2005gl023518

Lee, S.-J., Chen, H.-W., Liu, Q., Komatitsch, D., Huang, B.-S., & Tromp, J. (2008). Three-Dimensional Simulations of Seismic-Wave Propagation in the Taipei Basin with Realistic Topography Based upon the Spectral-Element Method. *Bulletin of the Seismological Society of America*, 98, 253–264. doi:10.1785/0120070033

Lee, S.-J., Komatitsch, D., Huang, B.-S., & Tromp, J. (2009). Effects of Topography on Seismic-Wave Propagation: An Example from Northern Taiwan. *Bulletin of the Seismological Society of America*, 99, 314–325.

Leiber, C.-O. (2003). *Assessment of safety and risk with a microscopic model of detonation*. Amsterdam Boston: Elsevier.

Lerbs, N., Zieger, T., Ritter, J., & Korn, M. (2020). Wind turbine induced seismic signals: the large-scale SMARTIE1 experiment and a concept to define protection radii for recording stations. *Near Surface Geophysics, 18*, 467-482. doi:10.1002/nsg.12109

Limberger, F., Lindenfeld, M., Deckert, H., & Rümpker, G. (2021). Seismic radiation from wind turbines: observations and analytical modeling of frequency-dependent amplitude decays. *Solid Earth, 12*, 1851–1864. doi:10.5194/se-12-1851-2021

Limberger, F., Rümpker, G., Lindenfeld, M., & Deckert, H. (2022). Development of a numerical modelling method to predict the seismic signals generated by wind farms. *Scientific Reports, 12*. doi:10.21203/rs.3.rs-1621492/v1

Malin, P. E., Bohnhoff, M., Blümle, F., Dresen, G., Martínez-Garzón, P., Nurlu, M., Ceken, U., Kadirioglu, F. T., Kartal, R. F., Kilic, T., Yanik, K., and Blümle, F. (2018). Microearthquakes preceding a M4.2 Earthquake Offshore Istanbul. *Scientific Reports, 8*. doi:10.1038/s41598-018-34563-9

Nakata, N., Gualtieri, L., & Fichtner, A. (2019). *Seismic Ambient Noise.* Cambridge, UK: Cambridge University Press. Retrieved from https://www.ebook.de/de/product/34941079/seismic_ambient_noise.html

Neuffer, T., & Kremers, S. (2017). How wind turbines affect the performance of seismic monitoring stations and networks. *Geophysical Journal International, 211*, 1319–1327. doi:10.1093/gji/ggx370

Neuffer, T., Kremers, S., & Fritschen, R. (2019). Characterization of seismic signals induced by the operation of wind turbines in North Rhine-Westphalia (NRW), Germany. *Journal of Seismology, 23*, 1161–1177. doi:10.1007/s10950-019-09866-7

Neuffer, T., Kremers, S., Meckbach, P., & Mistler, M. (2021). Characterization of the seismic wave field radiated by a wind turbine. *Journal of Seismology, 25*, 825–844. doi:10.1007/s10950-021-10003-6

Olsen, K. B. (2000). Site Amplification in the Los Angeles Basin from Three-Dimensional Modeling of Ground Motion. *Bulletin of the Seismological Society of America*, 90, S77–S94. doi:10.1785/0120000506

Olsen, K. B., Archuleta, R. J., & Matarese, J. R. (1995). Three-Dimensional Simulation of a Magnitude 7.75 Earthquake on the San Andreas Fault. *Science*, 270, 1628–1632. doi:10.1126/science.270.5242.1628

Rahman, M., & Michelitsch, T. (2006). A note on the formula for the Rayleigh wave speed. *Wave Motion*, 43, 272–276. doi:10.1016/j.wavemoti.2005.10.002

Richart, F. E., Wood, R. D., & Hall, J. R. (1970). *Vibration of soils and foundations.* Prentice-Hall, New Jersey.

Roten, D., Olsen, K. B., & Takedatsu, R. (2019). Numerical Simulation of M9 Megathrust Earthquakes in the Cascadia Subduction Zone. *177*, 2125–2141. doi:10.1007/s00024-018-2085-5

Saccorotti, G., Piccinini, D., Cauchie, L., & Fiori, I. (2011). Seismic Noise by Wind Farms: A Case Study from the Virgo Gravitational Wave Observatory, Italy. *Bulletin of the Seismological Society of America, 101*, 568–578. doi:10.1785/0120100203

Shearer, P. (2009). *Introduction to Seismology, Second Edition.* Cambridge University Press, Cambridge.

Siena, L. D., Thomas, C., Waite, G. P., Moran, S. C., & Klemme, S. (2014). Attenuation and scattering tomography of the deep plumbing system of Mount St. Helens. *Journal of Geophysical Research: Solid Earth, 119*, 8223–8238. doi:10.1002/2014jb011372

Spies, T., Schlittenhardt, J., & Schmidt, B. (2017). Abschlussbericht für das Verbundprojekt MAGS2: Mikroseismische Aktivität geothermischer Systeme 2 (MAGS2) - Vom Einzelsystem zur großräumigen Nutzung. *Tech. rep., Bundesanstalt für Geowissenschaften und Rohstoffe,*. doi:https://doi.org/10.2314/GBV:1011266393

Stammler, K., & Ceranna, L. (2016). Influence of Wind Turbines on Seismic Records of the Gräfenberg Array. *Seismological Research Letters, 87*, 1075–1081. doi:10.1785/0220160049

Styles, P., Stimpson, I., Toon, S., England, R., & Wright, M. (2005). *Microseismic and Infrasound Monitoring of Low Frequency Noise and Vibrations from Windfarms.* Ph.D. dissertation, Keele University.

Welch, P. (1967). The use of fast Fourier transform for the estimation of power spectra: A method based on time averaging over short, modified periodograms. *IEEE Transactions on Audio and Electroacoustics, 15*, 70–73. doi:10.1109/tau.1967.1161901

Westwood, R. F., & Styles, P. (2017). Assessing the seismic wavefield of a wind turbine using polarization analysis. *Wind Energy, 20*, 1841–1850. doi:10.1002/we.2124

Withers, M. M., Aster, R. C., Young, C. J., & Chael, E. P. (1996). High-frequency analysis of seismic background noise as a function of wind speed and shallow depth. *Bulletin*

of the Seismological Society of America, 86, 1507–1515. doi:10.1785/bssa0860051507

Zieger, T., & Ritter, J. R. (2018). Influence of wind turbines on seismic stations in the upper rhine graben, SW Germany. *Journal of Seismology, 22*, 105–122. doi:10.1007/s10950-017-9694-9

Zieger, T., Nagel, S., Lutzmann, P., Kaufmann, I., Ritter, J., Ummenhofer, T., Knödel, P, and Fischer, P. (2020). Simultaneous identification of wind turbine vibrations by using seismic data, elastic modeling and laser Doppler vibrometry. *Wind Energy, 23*, 1145–1153. doi:10.1002/we.2479

List of Figures

Appendix

APPENDIX 1

Supporting Information for

Seismic radiation from wind turbines: observations and analytical modeling of frequency-dependent amplitude decays

Fabian Limberger[1,2], Michael Lindenfeld[1], Hagen Deckert[2], and Georg Rümpker[1]

[1]Institute of Geosciences, Goethe-University Frankfurt, 60438 Frankfurt am Main, Germany
[2]Institute for Geothermal Resource Management (igem), 55411 Bingen, Germany

Supplement of Solid Earth, 12, 1851–1864, 2021
https://doi.org/10.5194/se-12-1851-2021-supplement

Solid Earth Open Access EGU

Supplement of

Seismic radiation from wind turbines: observations and analytical modeling of frequency-dependent amplitude decays

Fabian Limberger et al.

Correspondence to: Fabian Limberger (limberger@igem-energie.de)

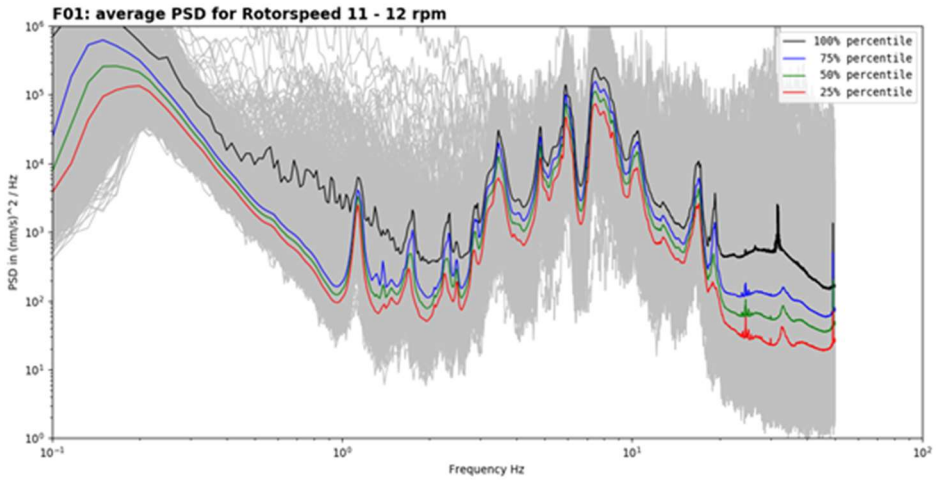

Figure S1: Effect of different percentiles (25 %, 50%, 75 % and 100 %) on the calculated average PSD spectra (coloured lines) for station F01. The grey lines in the background represent single PSD spectra derived from 10 min time windows recorded at "full power" status from Sep 2019 to Mar 2020 (9855 single PSD spectra in total). To estimate the PSD amplitude decay with distance we used the 25% percentile average (red line) calculated from 2463 single PSD spectra at each of the profile stations.

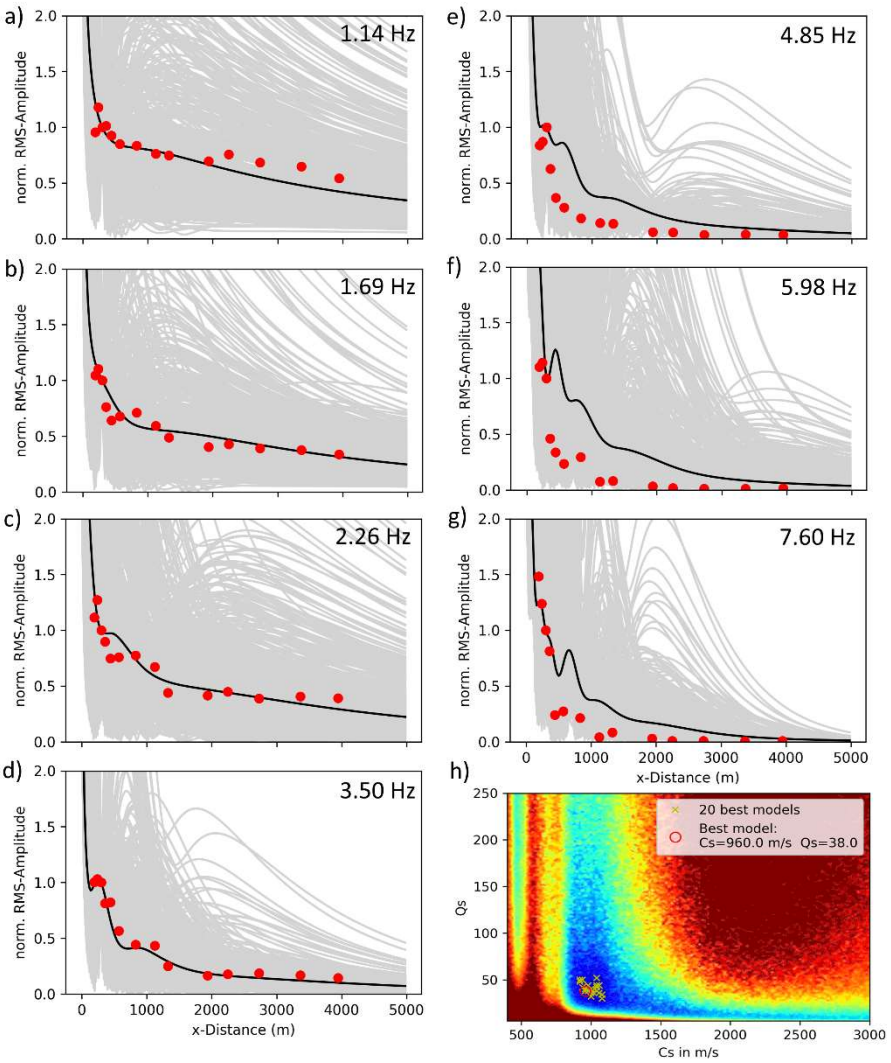

Figure S2: (a)-(g) Comparison of calculated and observed data (red dots) for seven signal frequencies assuming a simplified homogeneous model of the subsurface. (h) Best model parameters are $c_S = 960$ m/s and $Q = 38$ to fit all data simultaneously.

APPENDIX 2

Supporting Information for

Development of a numerical modelling method to predict the seismic signals generated by wind farms

Fabian Limberger[1,2], Georg Rümpker[1,3], Michael Lindenfeld[1], and Hagen Deckert[2]

[1]Institute of Geosciences, Goethe-University Frankfurt, 60438 Frankfurt am Main, Germany
[2]Institute for Geothermal Resource Management (igem), 55411 Bingen, Germany
[3]Frankfurt Institute for Advanced Studies (FIAS), 60438 Frankfurt am Main, Germany

Supplementary figures

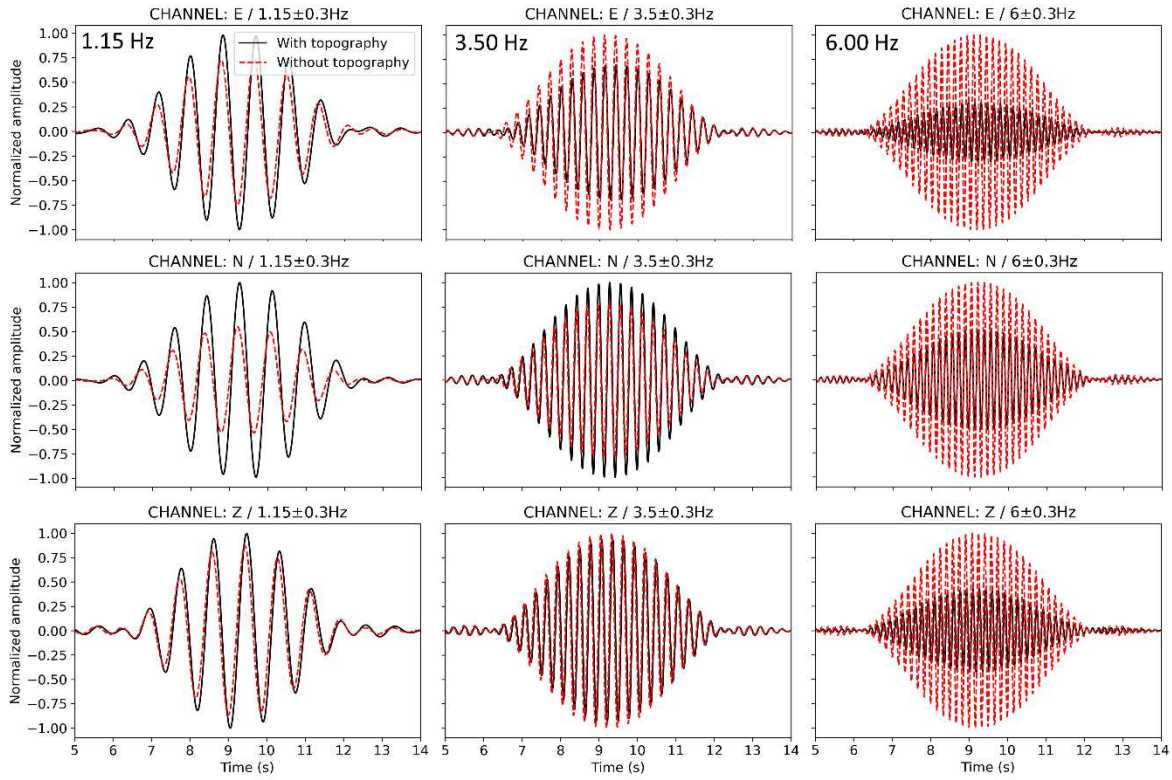

Figure S1: Synthetic waveforms of the E (top), N (middle) and Z (bottom) components simulated at the permanent seismic station (TNS) and filtered within frequency bands of 0.85–1.45 Hz (left), 3.2–3.8 Hz (middle) and 5.7–6.3 Hz (right). The low-frequency signal components are clearly amplified due to topography in comparison with the high-frequency signals.

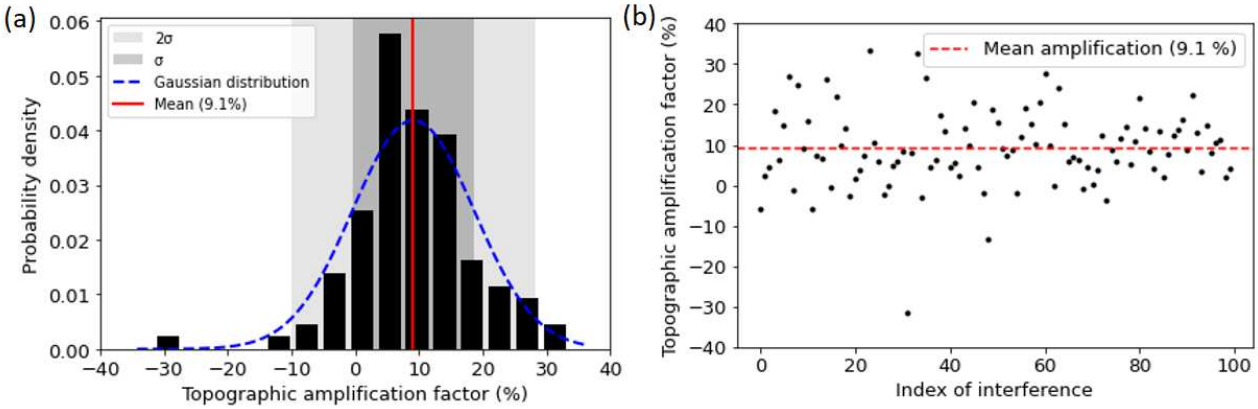

Figure S2: (a) The distribution of 1.15 Hz signal amplification at TNS due to topography for the 100 scenarios of interferences. The mean amplification is 9.1 %. The range is from -31 % to 34 %. However, -31 % is an outlier and an amplification is likelier than a reduction of amplitude (b).

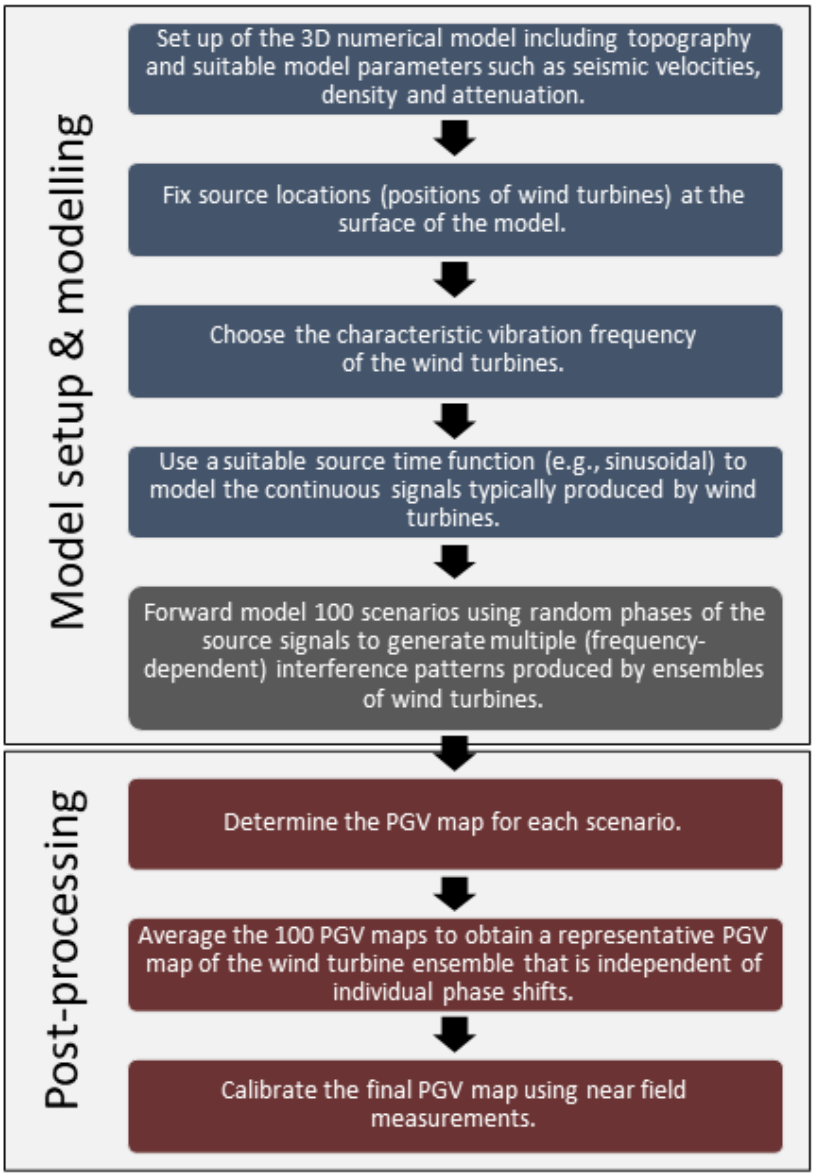

Figure S3: The flow chart represents the procedure of modelling the radiation pattern of wind turbines used in the study.

Table S1: I95 values for ground acceleration, velocity and displacement at station GSW and TNS during conditions with strong wind and no wind.

	Acceleration		Velocity		Displacement	
	Strong wind	No wind	Strong wind	No wind	Strong wind	No wind
GSW	1734 nm/s²	375 nm/ s²	240 nm/s	52 nm/s	33 nm	7 nm
TNS	108 nm/s²	50 nm/s²	15 nm/s	7 nm/s	2 nm	1nm

APPENDIX 3

Supporting Information for

The impact of seismic noise produced by wind turbines on seismic borehole measurements

Fabian Limberger[1,2], Georg Rümpker[1,3], Michael Lindenfeld[1], and Hagen Deckert[2]

[1]Institute of Geosciences, Goethe-University Frankfurt, 60438 Frankfurt am Main, Germany
[2]Institute for Geothermal Resource Management (igem), 55411 Bingen, Germany
[3]Frankfurt Institute for Advanced Studies (FIAS), 60438 Frankfurt am Main, Germany

Supporting Information for

The impact of seismic noise produced by wind turbines on seismic borehole measurements

F. Limberger[1,2], G. Rümpker[1,3], M. Lindenfeld[1], and H. Deckert[2]

[1]Institute of Geosciences, Goethe-University Frankfurt, 60438 Frankfurt am Main, Germany

[2]Institute for Geothermal Resource Management (igem), 55411 Bingen, Germany

[3]Frankfurt Institute for Advanced Studies (FIAS), 60438 Frankfurt am Main, Germany

Correspondence to: Fabian Limberger (limberger@igem-energie.de)

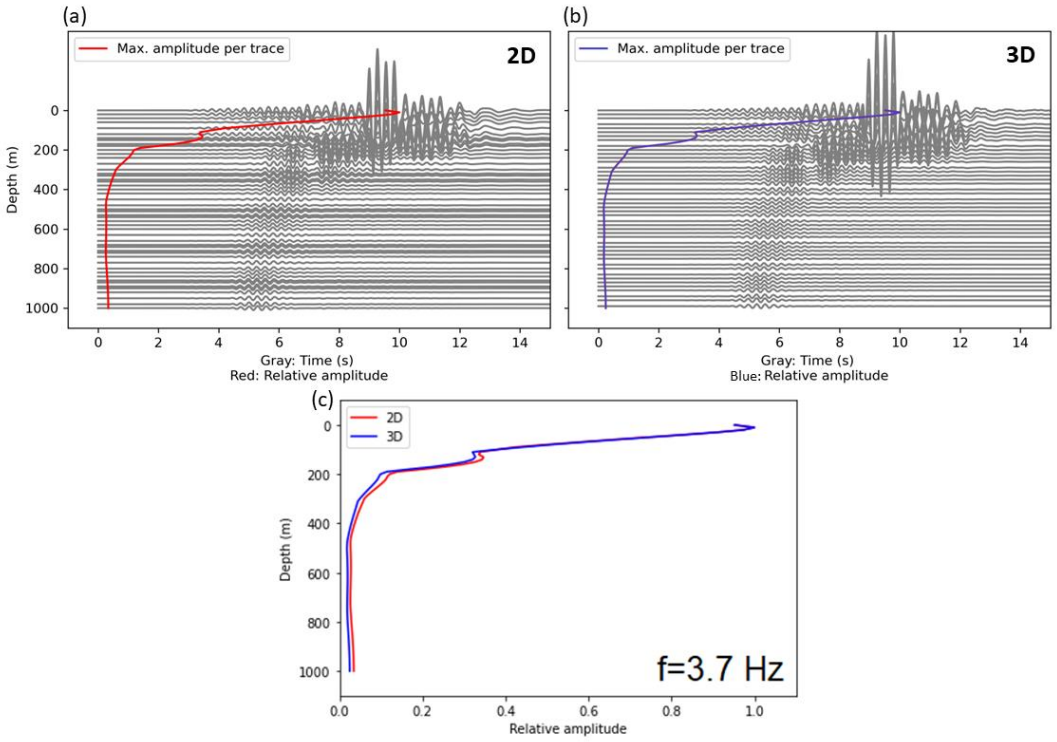

Figure S1: Comparison between the simulation of 3.7 Hz signals in two and three dimensions. The difference is not significant, hence, simulations in two dimensions are suitable to estimate the amplitudes in dependency on the depth.

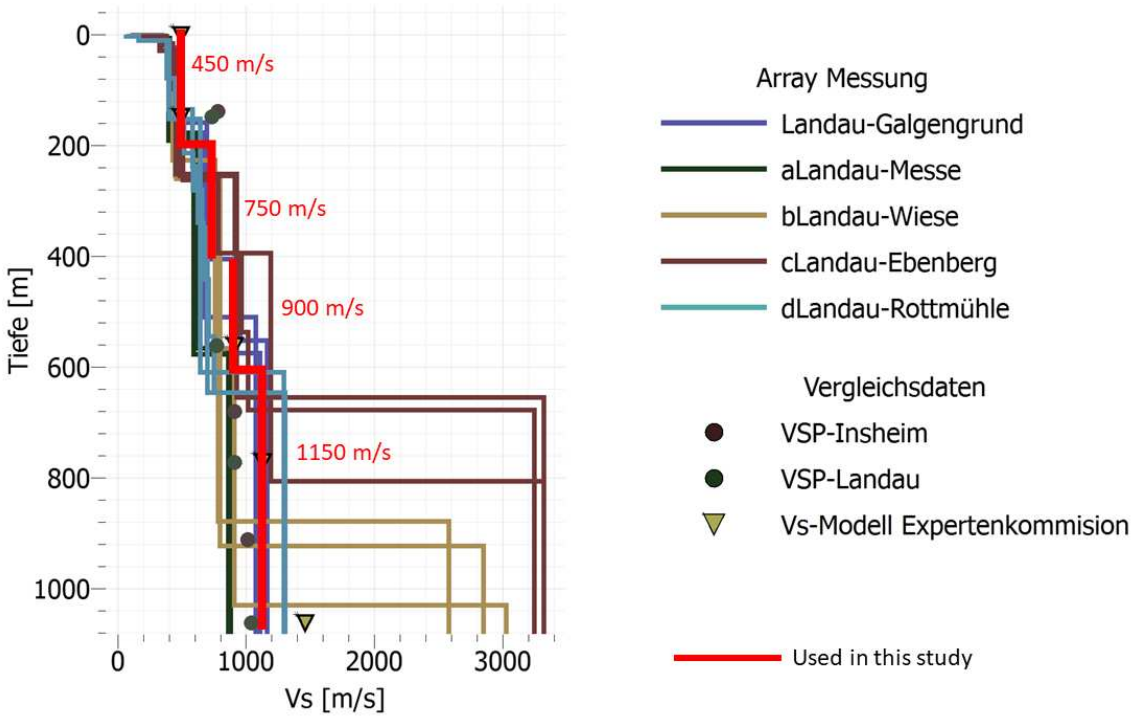

Figure S2: Model of the subsurface in the Landau Region (Rhineland-Palatinate, Germany) provided by Spies et al. (2017). The red line shows the velocity model used for the real data validation in this study. The seismic velocities are provided by the MAGS2 project. The figure is taken from Spies et al. (2017). The red lines are added and indicate the velocity model used in our study.

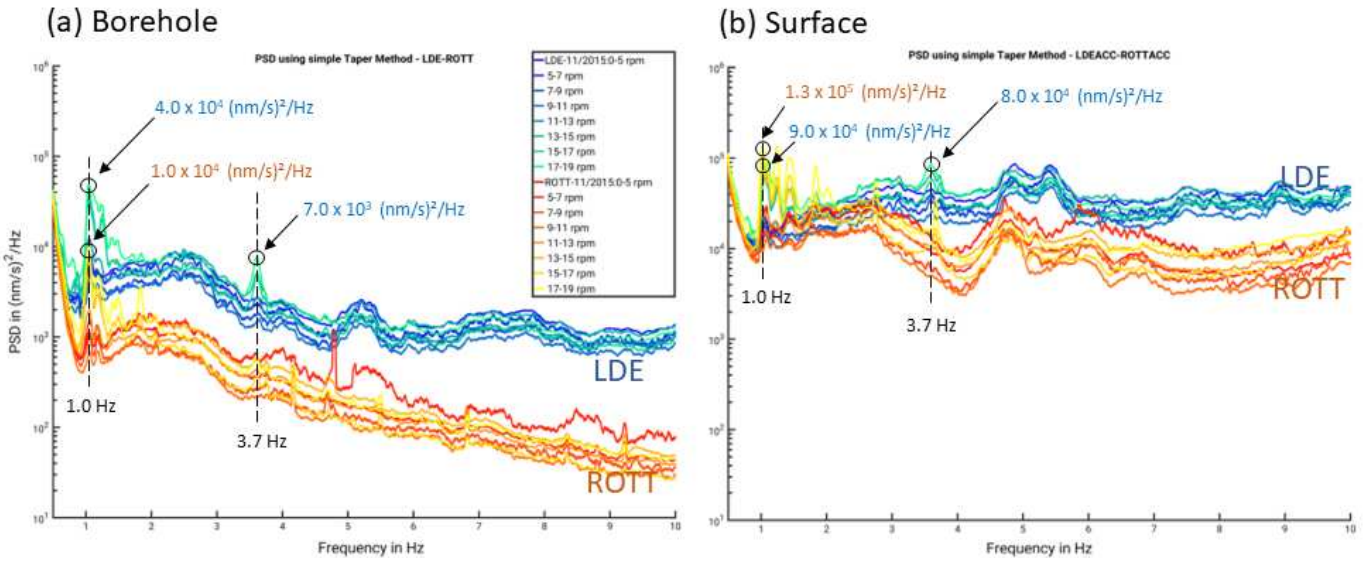

Figure S3: The figure by Zieger and Ritter (pers. comm., 2018) is modified by adding markers, arrows and numbers. PSD values by Zieger and Ritter (2018) show a reduction of amplitudes for 1 Hz (at ROTT and LDE) and 3.7 Hz (at LDE) signals due to boreholes. We transformed the PSD values in relative amplitudes by applying the root square. The comparison between the amplitude at the surface station and borehole station yields the reduction factors and percentages of 73% (ROTT, 1 Hz), 71 % (LDE, 1 Hz) and 34 % (LDE, 3.7 Hz).

The PSD amplitudes provided by Zieger and Ritter (2018) in Fig. S3 are transformed into amplitudes at the surface (AMP_{SF}) and in the borehole (AMP_{BH}) by calculating the square root. A scaling with frequency is not necessary in this case, since we compare PSD amplitudes at an identical frequency. The amplitude in the borehole is then divided by the amplitude at the surface to derive the factor *F* of noise amplitude reduction.

$$F_{ROTT,\ 1\,Hz} = \frac{AMP_{BH}}{AMP_{SF}} = \sqrt{\frac{PSD_{BH}}{PSD_{SF}}} = \sqrt{\frac{1.0\ \times 10^4}{1.3\ \times 10^5}} = 0.27\ (\cong 73\%\ reduction)$$

$$F_{LDE,\ 1\,Hz} = \sqrt{\frac{4.0\ \times 10^4}{9.0\ \times 10^4}} = 0.66\ (\cong 34\%\ reduction)$$

$$F_{LDE,\ 3.7\,Hz} = \sqrt{\frac{7.0\ \times 10^3}{8.0\ \times 10^4}} = 0.29\ (\cong 71\%\ reduction)$$

Erklärung

Ich erkläre hiermit, dass ich mich bisher keiner Doktorprüfung im Mathematisch-Naturwissenschaftlichen Bereich unterzogen habe.

Frankfurt am Main, den 22.03.2023

(Unterschrift)

Versicherung

Ich erkläre hiermit, dass ich die vorgelegte Dissertation über

Experimental and numerical analysis of seismic waves produced by wind farms

selbständig angefertigt und mich anderer Hilfsmittel als der in ihr angegebenen nicht bedient habe, insbesondere, dass alle Entlehnungen aus anderen Schriften mit Angabe der betreffenden Schrift gekennzeichnet sind.

Ich versichere, die Grundsätze der guten wissenschaftlichen Praxis beachtet, und nicht die Hilfe einer kommerziellen Promotionsvermittlung in Anspruch genommen zu haben.

Frankfurt am Main, den 22.03.2023

(Unterschrift)

Acknowledgements

Writing now the following lines at the very end of my PhD time is probably one of the most important things to do: Thank the people without it would not have been possible to come that far.

First and foremost, I would like to thank Georg Rümpker for supervising this PhD project. Your confidence and patience, the explanations based on huge experience and your open ear whenever I needed something from you were a great support. I enjoyed our scientific discussions. You gave me the opportunity and necessary space to develop my own ideas, for which I am very grateful.

I express my thankfulness to Hagen Deckert. Thanks for all the conversations and support to discover new perspectives and ideas. I thank you for trusting me to manage this project in our group and advising me, scientifically as well as personally.

Special thanks to Christine Thomas for kindly agreeing to examine this thesis.

I am thankful that I could work together with Michael Lindenfeld during my whole PhD time. After decades of installing seismometers across the globe, Michael has an enormous experience I learned from. Our discussions brought me always a step further. I enjoyed a lot our field trips to Uettingen, to drag thousands of heavy batteries across fields and forests. Michael, your relaxing attitude was very pleasant for me. Furthermore, I always felt welcomed at the seismology working group in Frankfurt and enjoyed the talks and discussions we had. Thank you all for your input.

I would like to thank my igem colleagues Ana, Steffen and Ludger, who helped me with struggles, discussed my scientific questions and made my daily work a bit easier and funnier. In those endless days of covid isolations, I was always happy to see your faces weekly in skype on my screen.

During all the ups and downs, I've got huge support by my fabulous friends around me, you know how much I like you. Thank you for having such a great time together. Probably I would get lost in research without you. Thanks for all the necessary distractions.

To my parents, thank you for giving me the chance and support to follow my childish dream of becoming a geoscientist. To my older brother and sister, Marco and Sonja, thanks for inspiring me in your own different ways and smoothing the way for me. To the littlest ones in the list, my nieces and nephew: Juna, Flora and Nahum. In busy times, there is nothing more refreshing than your young and imaginative spirits. Let me know, if you read this in 20 years.

More than a decade ago, Hanna and I started an adventure bigger than any PhD, Postdoc or Professorship. Being with you is like a soothing vacation somewhere warm and happy. Hanna, thank you for your endless support. Thanks for being who you are!